Characterization of the Dynamic Strength of Aluminium at Extreme Strain Rates and Pressures

by

Ashish Gopalakrishnan

A Thesis Presented in Partial Fulfillment
of the Requirements for the Degree
Master of Science

Approved April 2017 by the
Graduate Supervisory Committee:

Pedro Peralta, Chair
Jagannathan Rajagopalan
Kiran Solanki

ARIZONA STATE UNIVERSITY

May 2017

ABSTRACT

The study of response of various materials to intense dynamic loading events, such as shock loading due to high-velocity impacts, is extremely important in a wide variety of military and industrial applications. Shock loading triggers extreme states, leading to high pressures and strain rates, and neglecting strength is a typical approximation under such conditions. However, recent results have shown that strength effects are larger than expected, so they must be taken into account. Recently, hydrodynamic instabilities, the most common being the Rayleigh-Taylor (RTI) and Richtmyer-Meshkov (RMI) instabilities, have been used to infer the dynamic strength of materials at high pressure conditions. In our experiments and simulations, a novel RMI approach is used, in which periodic surface perturbations are made on high purity aluminium target, which was laser ablated to create a rippled shock front. Due to the slow linear growth rate of RMI, the evolution of the perturbations on the back surface of the sample as a result of the rippled shock can be measured via Transient Imaging Displacement Interferometry (TIDI). The velocity history at the free surface was recorded by spatially resolved laser velocimetry. These measurements were compared with the results from the simulations, which were implemented using rate independent and rate dependent material models, to characterize the dynamic strength of the material. Simulations using the elastic-perfectly plastic model, which is rate independent, failed to provide a value of dynamic yield strength that would match experimental measurements of perturbation amplitudes. The Preston-Tonks-Wallace (PTW) model, which is rate dependent model, worked well for aluminium. This model was, in turn, used as a reference for calibrating the rate dependent Steinberg-Lund model and the results from simulations using the calibration models were also compared to experimental measurements.

ACKNOWLEDGMENTS

It all started when my advisor Dr. Pedro Peralta took me in his research team. I still remember it afresh when he said “Try and Fail, and You will Learn”, which indeed has been a very motivating statement. From then till now, it has been an amazing journey, and I would like to take this opportunity to express my sincere gratitude to Dr. Pedro Peralta for providing me with a knowledgeable research experience and I am also grateful to him for all the countless efforts he has taken in educating me throughout, and providing everything that was necessary.

I would also like to thank Eric Loomis at Los Alamos National Laboratory (LANL), for his contribution in providing the experimental data for this project.

I had a great time working alongside my colleagues Jay, Nirmal, Sneha, Liz, Ben, Dexin and Zach. Many thanks to all of them for all the good times and for always being there to help. Special thanks to Saul, for providing a lot of assistance during the course of my research, as well as for meeting up with me often and clearing all my doubts.

Life is incomplete without friends. Cheers to all those friends who were very supportive and encouraging throughout this period.

I am indebted to my parents for their tremendous support, without which I wouldn’t be where I am today. I would like to sincerely thank my parents for being a pillar to support me in my life.

This work was funded by Los Alamos National Laboratory under the Laboratory Directed Research and Development – Directed Research (LDRD-DR) program; project #20060021DR, by the United States Department of Energy under National Nuclear Security Administration grants # DE-FG52-06NA26169, DE-FG52-10NA29653, and DE-NA0002005, and Office of Fusion Energy Science grant # DE-SC0008683.

TABLE OF CONTENTS

Page

CHAPTER Page

LIST OF TABLES

LIST OF FIGURES

CHAPTER 1

INTRODUCTION

The United States of America (USA) has not developed and tested nuclear weapons since 1992. International treaties such as the Comprehensive Nuclear Test Ban Treaty (CTBT), which was adopted in 1996 bans all nuclear explosions for both civilian and military purposes, in all environments [1]. This international ban on testing is a significant national issue, since ageing of the entire stockpile of the remaining nuclear weapons needs to be taken into serious consideration as it can cause the weapon to fail or act unpredictably and the reliability of the stockpile cannot be verified through testing. The Stockpile Stewardship Program (SSP) was established by the Department of Energy (DOE) and the National Nuclear Security Administration (NNSA) to predict the performance, reliability and safety of nuclear weapons system without nuclear testing. The Accelerated Strategic Computing Initiative (ASCI) was established in 1995 to support the SSP in developing new simulation tools that can predict the behaviour of nuclear weapons with aging and also to run simulations that can be used as a base for new nuclear weapon design [2].

High pressure at the time of detonation causes a shock wave to travel through the pit material that can cause spallation and other failure modes that are affected by dynamic material strength [3], [4]. Studying shock physics is important to understand the dynamic properties of materials under conditions of high pressure, high temperature and high strain rates typical of these conditions, and can also provide important insights into equations of state, phase transitions and mechanical properties. The study of response of various materials to shock loading spans analytical, numerical and experimental approaches that can be used to understand and predict the effects of

intense dynamic loading events such as ballistic impact, blast loading, debris impacts on space vehicles and satellites, automobile crash and large scale geological events (earthquakes, volcanic eruptions) on materials and structures. The material models developed as a part of ASCI predicts the dynamic strength, damage and failure response of materials under extreme conditions of parameters such as pressure, temperature and strain rate that are unique to weapons using specialized computer codes and experimental data. The ASCI works in collaboration with National Laboratories and advanced supercomputers are used for the purpose of computation and modelling [2], [3], [5].

Inertial Confinement Fusion (ICF) is another application that requires deep understanding of shock waves, their impact on material behaviour and vice-versa, i.e., how material behaviour affects these waves and the implosion process required to achieve thermonuclear ignition. The ICF program is a part of NNSA and also supports the SSP in providing experimental capabilities in High Energy Density Physics (HEDP) required for safe maintenance of the nuclear stockpile [2]. The ICF process involves a fuel target that is heated and compressed to initiate nuclear fusion. When high energy laser, electrons or ion beams hit the outer layer of the target, shock waves are generated. They travel inward thereby heating and compressing the fuel at the center and causing fusion reactions. Researchers have been trying to study the effects of hydrodynamic instabilities that accelerate the growth of non-uniformities on the target surface that can reduce the final compression and quench the ignition process [6]. Instabilities in a system refers to infinitesimal velocity or density perturbances or any effect on the state of the system that is amplified by base or global forces and thus leads to growth of these infinitesimal perturbations to finite size as a result of impulse forces across the perturbed biomaterial interface. The system may depart from the initial state and may never return

to that state [7]. The Rayleigh-Taylor (RTI), Richtmeyer-Meshkov (RMI) and Kelvin-Helmholtz (KHI) instabilities are predominant and common in most hydrodynamic situations.

RTI occurs at the interface of fluids of different densities when the interface is accelerated towards the denser fluid [8]. When two fluids of different densities are placed on top of each other such that the heavier fluid is above, the small perturbations present on the interface rapidly grow in time as a result of gravity [8]. The RT instability causes the initial perturbations to progress from a linear growth phase into an exponential growth phase, eventually developing plumes that rise up and spikes that fall down [9].

The RM instability occurs when a shock wave crosses the interface between two different fluids, which is not perfectly flat [8]. The shock wave suddenly distorts the boundary, thereby imparting a non-uniform velocity and causing amplification of the perturbation following the refraction of the shock [8], [10]. In ICF, the non-uniform shock fronts will induce a highly perturbed flow behind them, which will trigger the RTI that occurs later during the acceleration phase of the target [11].

The KH instability occurs when two superimposed thick fluid layers are moving with opposite velocities which cause a shear motion between them [8]. Small sinusoidal perturbations grow exponentially with time and as they become comparable to the wavelength, the perturbed interface become asymmetric and characteristic rolls appear [8].

Researchers have been studying the instabilities across a solid/solid and solid/fluid interfaces in an attempt to determine the material property by observing the growth of perturbations [12]–[14]. The yield strength of the material under high pressure

conditions is an important parameter in many applications [15]. The experimental techniques involved were used to study the effect of strength on instability growth as the dynamic yield strength of solids acts to dampen the amplitude of perturbation growth [12], [16]. Both RT and RM instabilities have been used effectively to infer material strength in solids under extreme conditions [17]. In these techniques, the sensitivity of the instabilities to material strength is used as a means to evaluate dynamic yield strength [17]. In addition to this, RMI experiments have also been recently used by many researchers to calibrate and validate various material models [15], [17], [18], [19].

Dynamic spallation is another important phenomenon that takes place when a material is shock loaded. A shock wave in a material produces internal stresses that can exceed the elastic limit resulting in plasticity and can also lead to superposition of release waves that can lead to spallation. The formation of a shock wave is a process that initiates large amplitude disturbances where the stress, density and other physical properties of a material changes in a discontinuous manner. The relationship between the parameters of state reached by shock compression, called the Hugoniot of a material, is used to develop the equation of state [20].

Spall strength or dynamic fracture strength is essential to study the failure mechanism due to interaction of two release waves. It is the amount of resistance offered to the growth of crack initiated by plastic flow. Researchers have been trying to understand the spallation in metals when they undergo shock loading. The study of spallation as a function of pulse duration, strain rate, temperature and loading history show the influence of microstructure on material failure process. The occurrence of spall involves nucleation, growth and coalescence of an array of cracks initiated at the spall plane [20]. Studying the effect of material strength on the growth of instabilities and

evolution of spall due to high pressure shock loads can be used to predict the effect of extreme loading conditions on the dynamic behaviour of a material.

In the next chapter, a brief introduction to shock waves is given along with the various experimental techniques that are used in shock wave research and the use of shock waves to study the effects of strength on hydrodynamic instabilities is also discussed.

CHAPTER 2

LITERATURE REVIEW

2.1 Basics of Shock Physics

The propagation of waves is an important phenomenon that affects a medium when it is subjected to local excitation. Upon excitation, the disturbance propagates through the material as a stress wave with a velocity given by equation [21]:

$$C^2 = \frac{1}{\rho}\frac{\partial \sigma}{\partial \varepsilon} \tag{2.1}$$

The equation of state for an ideal gas for an isentropic process is given by PV^{γ}=constant. Differentiating this equation gives the following relation [21]:

$$\frac{dP}{dV} = -\gamma\frac{P}{V} \tag{2.2}$$

In the above equation, P is the pressure, V is the volume, γ is the ideal gas constant, dP and dV are the changes in pressure and volume respectively. The derivative is directly related to P/V and $|dP/dV|$ increases with a rise in the pressure. From equation (2.1), the velocity of stress waves for an ideal gas in one dimension becomes $\frac{1}{\rho}\left(\frac{dP}{dV}\right)^{0.5}$. The velocity of disturbance is proportional to $\left(\frac{dP}{dV}\right)^{0.5}$ due to which the higher amplitude regions of the disturbance travel faster than the lower amplitude regions [21]. This results in rapid changes of pressure as the disturbance travels through the material and leads to the formation of a shock wave. As the sample is a thin plate, the geometrical constraints produced by it lead to uniaxial strain condition. Under uniaxial strain conditions, extremely high amplitude waves can travel through a material without changing its macroscopic dimensions and form a state of compressive stress close to hydrostatic compression that makes the shear stresses negligible [21]. This leads to a convexity in the stress-strain curve represented by the following equation [21]:

$$\frac{\partial}{\partial \varepsilon}\left(\frac{\partial \sigma}{\partial \varepsilon}\Big|_{s}\right) > 0 \tag{2.3}$$

Due to this, the shock front steepens and causes a discontinuity in pressure, temperature, internal energy and density as it travels through the material [21]. Shock waves are assumed to have no apparent thickness [21]. The fundamental requirement for the establishment of a shock wave is that the velocity of the pulse increases with increasing pressure [21].

In elastic-plastic solids, shock waves can exist in three different pressure regimes: purely elastic (acoustic), elastic-plastic, which has a two-wave structure, and hydrodynamic, where the hydrostatic stress is so high that the shear stresses become negligible and the strength of the material can be neglected [22]. In the two-wave regime, the main shock is preceded by an elastic precursor that is equal to the Hugoniot Elastic Limit (HEL) of the material. The HEL refers to the elastic limit under the imposed stress and strain rate conditions.

The dynamic yield stress, also known as the HEL, is the maximum stress amplitude for elastic wave propagation in a material. As the stress increases above the HEL, the material yields plastically under dynamic loading [23]. The compressive yield strength of materials subjected to high pressure shock loading is important in a number of scientific applications, including equation of state studies and high velocity penetration of armour by long rod penetrators [24]. Plastic strains are negligible at the elastic wave front and the elastic precursor amplitude characterizing yield strength in uniaxial deformation under plane wave loading is related to the yield strength by equation 2.4 [25].

$$\sigma_{HEL} = \left(\frac{1-\nu}{1-2\nu}\right) Y_{dHEL} \tag{2.4}$$

where, ν is the Poisson's ratio, σ_{HEL} is the HEL, and Y_{dHEL} is the yield strength. It is very difficult to measure the yield strength from shock experiments as the data slightly differs from idealized representations of the wave profiles. The HEL is calculated from the amplitude of the elastic wave at its interface with the plastic wave. Figure 2.1 shows the velocity profile of a real shock wave in which the HEL is also indicated.

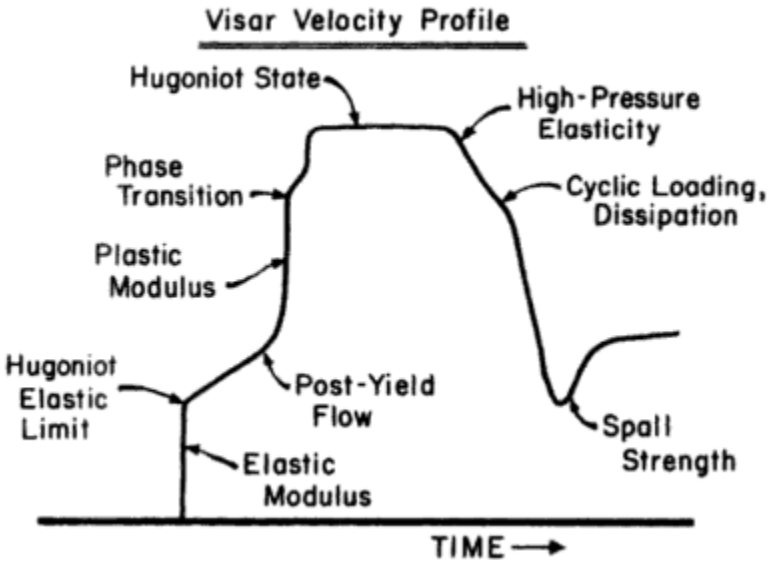

Figure 2.1: Velocity profile of a real shock wave indicating HEL [21].

Below the HEL, the wave is elastic in nature and the longitudinal wave speed at pressures below the HEL is given by equation [26]:

$$c_l = \left(\frac{K+\frac{4}{3}G}{\rho}\right)^{\frac{1}{2}} \tag{2.5}$$

The shock wave exceeds HEL at high pressures to cause plastic flow. As pressure increases above HEL, shear stresses become negligible and shear modulus G can be neglected and the longitudinal wave speed is expressed as in equation 2.6 [26]. At overdriven pressures, the plastic component travels faster and overtakes the elastic precursor, obliterating the two-wave structure and leading to a single shock front [21].

$$c_o = \left(\frac{K}{\rho}\right)^{1/2} \tag{2.6}$$

Figure 2.2 shows the schematic of a shock front profile wherein the material state changes discontinuously from one side of the front to the other. In this figure, U_s is the shock velocity, U_p is the particle velocity, P is the pressure, ρ is the density and properties of the material ahead of the shock front are represented by a subscript 'o'. The body forces and heat conduction at the shock front are considered to be negligible. As described above, the main condition required for existence of a shock is that the propagation velocity of the pulse increases with increasing pressure. Parameters such as mass, energy and momentum must be conserved across the discontinuous shock fronts. These waves can be represented mathematically by the Rankine-Hugoniot equations [21].

Conservation of mass: $\rho_o = \rho(U_S - U_P)$ (2.7)

Conservation of momentum: $P - P_o = \rho_o U_S U_P$ (2.8)

Conservation of energy: $E - E_o = 0.5(P + P_o)(V_o - V)$ (2.9)

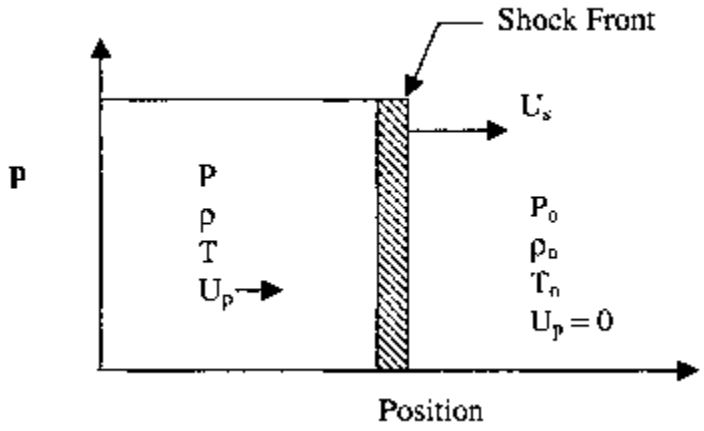

Figure 2.2: Profile of a shock front propagating through a material [27].

If the initial conditions represented by subscript 'o' are known, then the constitutive relations have 3 equations with 5 unknowns namely U_s, U_p, P, V and E. The particle velocity U_p can be measured using various diagnostic techniques. This would reduce the number of unknowns to four. To solve for all the parameters, another relationship is needed which involves the constitutive behaviour of the material that relates two or more of the variables [21]. The equation of state (EOS) defines all equilibrium states in a material and provides the pressure-volume-energy relations needed for shock calculations and using this relation, any parameter can be determined as a function of one parameter. The Linear-Hugoniot relationship is one such equation that is determined empirically and relates the shock velocity and particle velocity according to the following equation [21]:

$$U_S = C_o + SU_P \tag{2.10}$$

where C_o is the sound velocity in the material at zero pressure and S is the slope of the shock Hugoniot, and is determined empirically [21]. This equation becomes invalid for materials undergoing a phase transition [21].

The set of conservation equations for a shock discontinuity along with the equations of state defines the Hugoniot of the material [28]. The Hugoniot of a material can be graphically represented by plotting it in stress-particle velocity plane or stress-specific volume plane. The slope of the plot in stress-particle velocity plane gives the dynamic impedance of the material, i.e. the reflected and transmitted stress amplitudes required to maintain continuity at the interface of the two materials used [20]. Representation of the Hugoniot in stress-specific volume plane has higher sensitivity to phase changes and other thermodynamic mechanisms [20]. Shock waves increase the temperature as the material is compressed. The thermodynamic process at the shock front is typically

assumed to be adiabatic. The release from the shock state to the initial state is assumed to be isentropic [20].

There are various experimental techniques to study shock waves and also to record dynamic data, which will be discussed in the following section. The rest of the chapter will help understand the various properties of materials such as yield strength and spall strength analysed when a material is shock loaded, the use of hydrodynamic instabilities to determine the effect of strength on shock waves and also highlight the use of different material models that are temperature and strain rate dependent.

2.2 Experimental Methods to Study Shock Waves

Shock waves are generated in a laboratory by impact of a high velocity flyer plate on a target sample, detonation of explosive charges or by laser ablation. Impacting a flyer plate on a target using a single stage or a multi-stage gas gun is one of the traditional methods to generate shock waves. The pressure vessel in the gas gun uses compressed gas to produce the required energy and drives the projectiles to the desired velocities [20], [29]. Laser irradiation and explosives are other methods that can be used to launch flyer plates [21]. At the time of production of shock waves using these techniques, there are three considerations. The impact must be planar, normal and parallel, which implies that the two surfaces are flat and all points on the surfaces establish contact at the same time. The direction of motion of the projectile is normal to the surface [21]. The conventional technique that was used to generate plane shock waves was by impacting the sample with a flyer plate at a velocity needed to reach desired shock stress, i.e., which should be high enough to exceed the HEL in order to study the effect of strength [21], [20].

The shock wave produced by plate impact technique has initially a square shape [21]. This shape has a flat top, the length of which is determined by the time required for the wave to travel through the flyer plate. When the flyer hits the target, plane compression waves are produced both in the flyer plate and the target. The duration of the compressive pulse in the target will be equal to the round-trip travel time through the thickness of the flyer [30]. The waves in the flyer reflect from the back surface and return into the target as tensile release waves [21]. These waves interact with the release waves reflected from the free surface of the target and produce internal stresses resulting in spallation. The rate of release of a shock wave is determined by the target material, the distance travelled by the pulse through the material and the material in which the pulse is travelling [21]. The strain rates developed in plate impact techniques are limited to a maximum of 10^6 s^{-1} [31]. High energy laser pulses can be used to generate stress waves that are much higher than those achieved by gas guns and are capable of probing extreme states of matter.

The ability of a laser beam to generate shock waves was first recognized and explored in the early 1960s [32]. Many applications such as ICF use laser ablation that produces a shock wave in the material and can achieve high strain rates of the order of 10^{12} s^{-1} [33]. The laser ablation technique has been used to create ultra-high pressure compression pulses and apply prescribed perturbations to capsule surfaces for hydrodynamic growth [34]. The various steps involved in this process are: laser absorption, thermal conduction, ablation and shock wave formation [35].

When a material is illuminated with an intense laser, it absorbs energy and atoms are ablated from the surface to form a plasma plume [36]. This induces inertial and mechanical confinement on the material surface that causes stress waves to propagate

into the surrounding media [37]. The absorbed energy evolves into material motion via a variety of processes, including multiphoton and avalanche ionization, plasma formation, time-dependent plasma optical density, plasma expansion and ion heating, electron-electron relaxation and electron-phonon coupling [38].

Shock waves imparted by laser ablation create a region of high pressure that moves through the body of the material. An increase in pressure is caused by the fast laser heating of the material giving it insufficient time to expand. Figure 2.3 shows the typical setup for laser ablation. When the laser hits the sample, energy is deposited in the skin depth at the surface of the sample. Plasma is formed by the ablation of the material on the surface that results in energy deposition. The pressure is applied to the remaining material in the sample until the laser pulse ends and the plasma cloud dissipates [32]–[37]. The condition for uniaxial strain is similar to those achieved in flyer plate impact method and the geometric constraint is usually satisfied only for the center region [39].

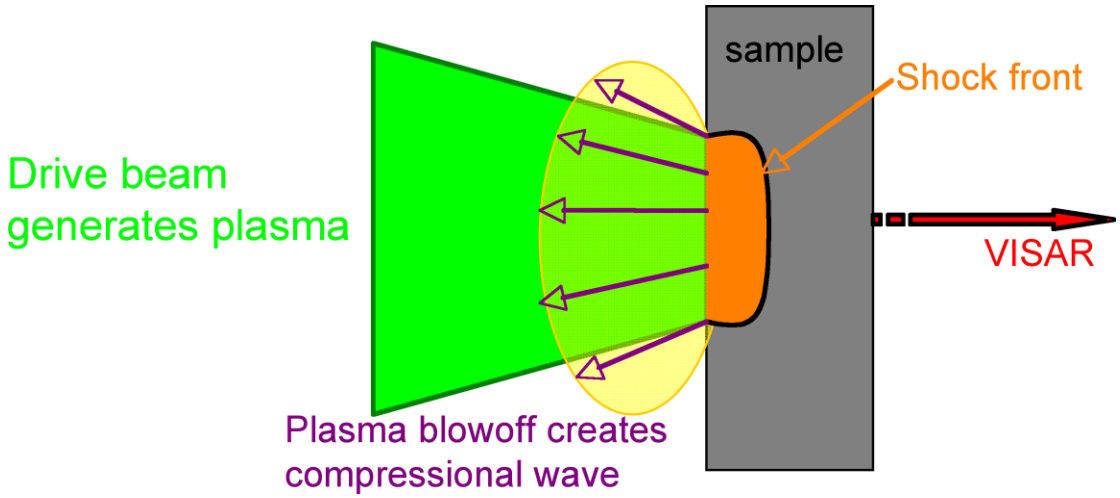

Figure 2.3: Setup showing formation of plasma generating shock waves [40].

The drive pulse and the target material decide the spatial and temporal characteristics of laser induced stress waves. In laser induced shock experiments, it is

more difficult to ensure the maintenance of a constant shock pressure. However, unlike other shock loading techniques, synchronization is more straightforward and it is easier to recover shock samples after the experiment is carried out since the momentum transfer is less. This technique can be used to investigate the mechanical and physical properties of condensed matter. Laser ablation technique has also provided detailed insights into plasticity and phase changes of materials on different time scales and pressures [32]–[37].

2.3 Dynamic Data Measurements

When a sample is shock loaded, it is essential to record the dynamic data on the surface opposite to that where impact happens. This shows the history of the transmitted shock wave and can be used to study material behaviour under high pressure conditions. The velocity at the free surface is nowadays often measure using interferometry techniques, two of which are the most popular: Velocity Interferometry System for Any Reflector (VISAR) and Photon Doppler Velocimetry (PDV). An advantage of VISAR is that it can be deployed such that it allows measurements of particle velocity on both time and space, the latter typically over a line [41], although 2-D versions that can measure velocity over an area have also been developed [42]. Given its use in this work, the VISAR will be briefly discussed. Figure 2.4 shows the schematic representation of velocity measurement from VISAR.

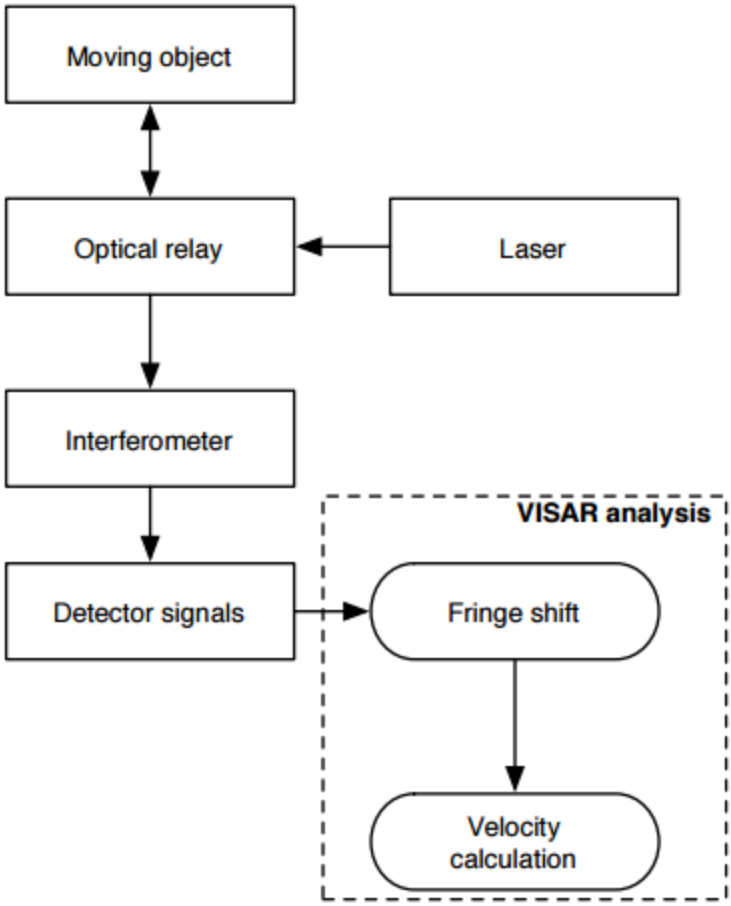

Figure 2.4: Overview of VISAR measurement [43].

When the object of interest is illuminated by a coherent laser light and reflected from the moving surface, the Doppler-shift in wavelength of the light is proportional to the velocity of the point that reflects it. The reflected light is captured by an optical relay and sent to an interferometer, which produces an output containing the input signal and a time delayed version of the input signal [43]. Fast optical detectors sense the output and the object's motion can be analysed. The VISAR employs optical interference to generate bright and dark bands of light called interference fringes [44]. The fringe shift is a

normalized measure of how the optical phase difference compares to the reference value. The velocity is in direct proportion with the fringe shift [43].

Photomultipliers and electronic streak cameras are used to record the point VISAR and line VISAR signals. Line VISAR can be used to measure the planarity of flyer plates and shock waves and also allow the shock wave velocity to be determined at shock break-out even if stepped or wedged samples are used [45]. The velocity histories of all points can also be recorded along a straight line on the specimen surface, where the signal can have temporal resolutions of the order of 100 *ps* [45]. This requires a recording time window that is very short, which is acceptable in plasma driven shock experiments [46]. Figure 2.5 shows an example of line VISAR record along with the velocity history obtained from line VISAR. The velocity history (figure 2.5 b) can be used to determine various material parameters such as the HEL, spall strength, experimental strain rate and also indicate if the material has undergone a phase transformation.

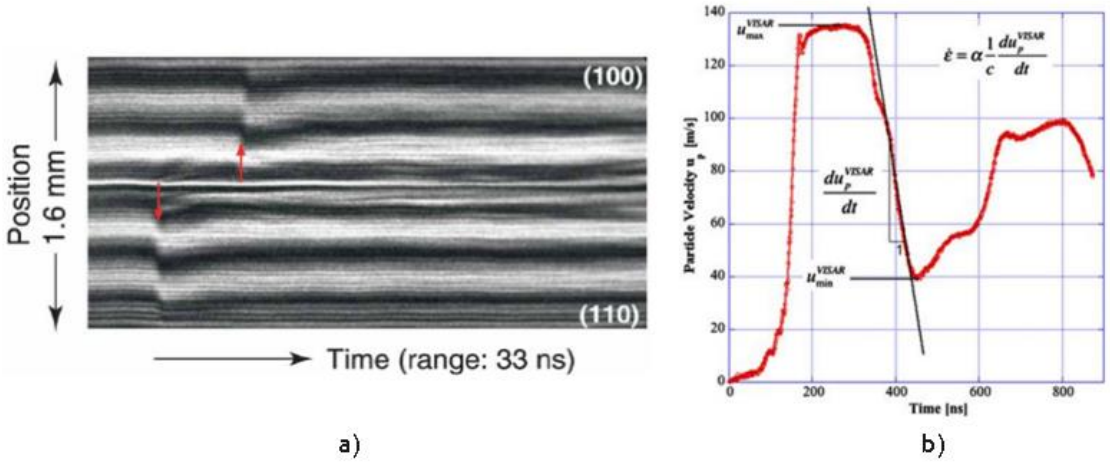

Figure 2.5: a) Line VISAR record of NiAl crystals [45]; b) Velocity profile that can be obtained from a line VISAR record after spatial averaging [47].

Another diagnostic that can provide useful dynamic data is the Transient Imaging Displacement Interferometer (TIDI), which can be used to measure the 2D out-of-plane displacement field at an optically accessible surface. The interferometer for the TIDI is a modified Mach-Zehnder design [48]. The surface displacement map is captured in a single shot with the time resolution of the illumination pulses. The surface motion can be tracked using a framing camera that captures up to eight displacement maps for a single loading event [48]. Each TIDI interferogram provides details about relative surface motion at that specific instance [49].

TIDI is used an effective tool in research studies involving the use of hydrodynamic instabilities to study material strength under extreme conditions. TIDI records the displacement at the diagnostic surface of the sample at specific instants of time after shock break out. The image can be post processed to get the displacement data that can used to analyse the effects of material strength on the evolution of hydrodynamic instabilities.

2.4 Dependence of Strength on Strain and Strain Rate

When the stress in a ductile material due to a transmitted pulse exceeds the elastic limit, the pulse will decompose into an elastic and plastic wave and the material experiences plastic deformation [21]. The plastic deformation of materials at high strain rate is often described by constitutive equations that link stress with strain, strain rate and temperature [21]. When a shock wave is formed under a state of uniaxial strain, the resulting plastic wave will have a sharp front [21]. Early shock wave equations of state studies assumed hydrodynamic material response and the effect of material strength was not taken into consideration [50]. However, the effects of strength play a major role at

very high shock wave amplitudes [50]. Figure 2.6 shows the dependence of strength on strain and strain rate.

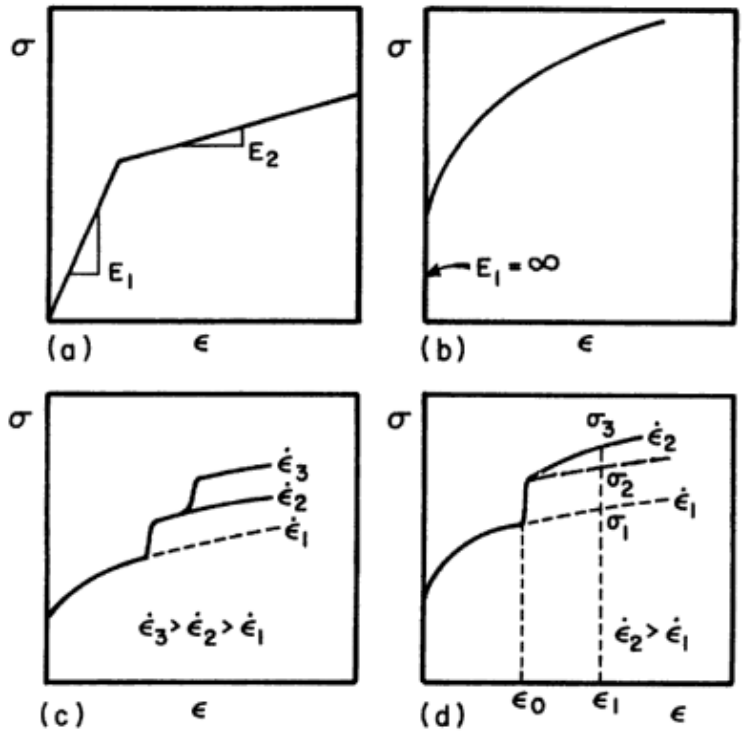

Figure 2.6: Stress-strain curves for ductile materials a) Bilinear elastoplastic; b) Work hardening using a power law; c) Strain rate dependence of flow stress; d) Strain rate history dependence of flow stress [21].

Figure 2.6 a shows the stress-strain curve represented by a bilinear elastoplastic model. In this model, the first stage is elastic and the second stage is plastic [21]. In many metals, the strain dependence of stress follows a power law as shown in figure 2.6 b and this is given by the following equation [21]:

$$\sigma = \sigma_0 + k\varepsilon^n \tag{2.11}$$

where σ_0 is the nominal stress, and n is the hardening parameter and is less than 1 [21]. Figure 2.6 c shows the dependence of strength on strain rate. The flow stress changes as the strain rate is changed during the test. The strain rate dependence of flow stress is represented by the following equation [21]:

$$\sigma = \sigma_0 + k\varepsilon^n \dot{\varepsilon}^m \tag{2.12}$$

where m is the strain rate sensitivity and usually varies between zero and unity for metals [21]. Strain rate history is another parameter that affects the mechanical response of a material [21]. The effect of strain rate history on flow stress is shown in figure 2.6 d. As the strain rate is changed from $\dot{\varepsilon}_1$ to $\dot{\varepsilon}_2$ at a strain ε_1, the flow stress changes from σ_1 to σ_2. If the strain rate change occurred earlier, at a strain of ε_0, the higher strain rate alters the work hardening rate and the material would exhibit a higher flow stress σ_3 at a strain ε_1 and strain rate $\dot{\varepsilon}_2$. The work hardening rate at the strain rate $\dot{\varepsilon}_2$ is higher than at the strain rate $\dot{\varepsilon}_1$ [21].

Shock loading of materials causes plastic deformation, which is irreversible and a path dependent process. There are a number of material models that have various equations to describe the dynamic behaviour of materials as a function of strain, strain rate and temperature. Section 2.5 briefly discusses various material models that have been prominently used to study dynamic material behaviour under shock loading. Before moving on to this section, it is essential to discuss about the different regimes in high strain rate conditions, which will be covered in the next section.

2.5 High Strain Rate Regimes

The principal agents of plastic deformations are dislocations, and the stress response of dislocation movements determines the flow stress response to strain, strain rate and temperature [21]. Thermally activated dislocation motion, dislocation drag and relativistic effects on dislocation motion are the three mechanisms governing plastic deformation at high strain rates [21].

2.5.1 Thermal Activation

Plastic deformation of crystalline solids, for example metals, is due to the formation and movement of dislocation [51]. The dislocation movement is controlled by a thermally activated process when the flow stress required to move dislocations shows temperature dependence [51]. A dislocation continuously encounters obstacles as it moves through the lattice [21]. Some of these obstacles include interstitial and solute atoms, vacancies, small-angle grain boundaries, vacancy clusters, inclusions, precipitates and so on. These obstacles make the movement of dislocations more difficult and sometimes, dislocations themselves can oppose the movement of dislocations [21]. A dislocation has to overcome an energy barrier when it moves from one equilibrium atomic position to another, i.e., a force has to be applied to it [21]. This can be seen in figure 2.7.

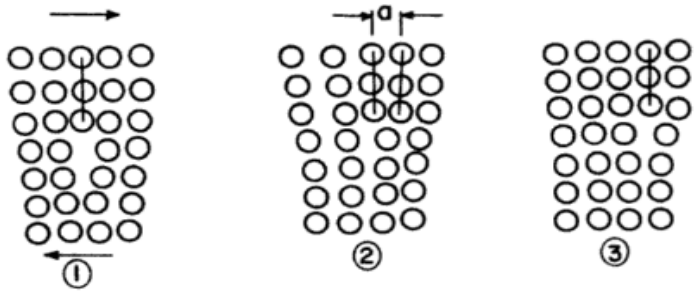

Figure 2.7: Movement of dislocation from one equilibrium position to next [21].

The stress required to move the dislocation without any additional support is the Peierls-Nabarro stress [21]. The energy barriers have a wavelength equal to the periodicity of the lattice. The dislocation motion encounters periodic barriers of different spacing and different lengths. The temperature and strain rate response of metals is influenced by the thermal energy of the lattice [21]. The amplitude of vibration of atoms increases with thermal energy, which also helps the dislocation to overcome obstacles. The thermal energy increases with increase in temperature, thereby decreasing the effective height of the barrier [21]. This can be clearly seen in a force-distance diagram in figure 2.8, in which the area under the curve represents an energy term.

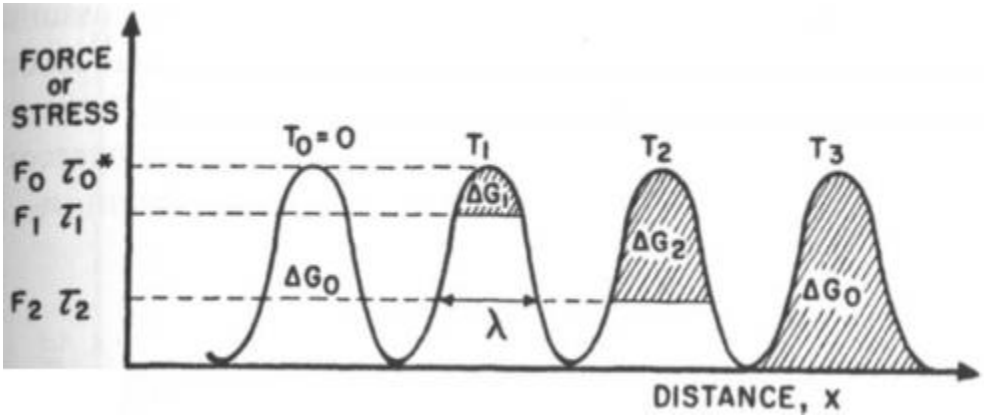

Figure 2.8: Overcoming of energy barrier by thermal energy [21].

Considering the existence of both short-range and long-range obstacles (cannot be overcome by thermal energy), the flow stress will have the athermal part, which is determined by the structure and the thermally activated part [21]. Regazzoni et al. described an equation to show the general relationship between applied stress, strain rate, and temperature at constant structure to represent the thermally activated regime [52].

$$\dot{\varepsilon} = \dot{\varepsilon}_0 \exp\left(-\frac{\Delta G}{kT}\right) \tag{2.13}$$

where, $\dot{\varepsilon}_0$ is the pre-exponential term that has negligible dependence on stress and temperature and is considered a constant, ΔG is the activation free energy, k is the Boltzmann constant, and T is the temperature [52]. The pre-exponential factor is given by equation 2.14 [52].

$$\dot{\varepsilon}_0 = \frac{\nu_0 \rho b \Delta l}{M} \tag{2.14}$$

where, ν_0 is the vibrational frequency of dislocation, ρ is the density, b is the Burger's vector, Δl is the distance between dislocation barriers, and M is the is the appropriate Taylor factor [52].

At increasing strain rates, there is less time available to overcome the barrier, i.e., the time spent by a dislocation waiting for thermal activation to add to the applied stress is reduced [21], [53]. This means that the thermal energy will be less effective and thermal activation may not be necessarily needed to assist a dislocation past a barrier [21], [52]. The dislocation motion becomes continuous and the dislocation velocity is solely limited by drag mechanisms. This is the dislocation drag regime and is briefly discussed in the next segment of this section.

2.5.2 Dislocation Drag

In a crystal, the presence of impurities offers resistance to the motion of dislocation due to which a dislocation cannot attain equilibrium [52]. The stress above which this happens is called the threshold stress. Above this region, the dislocation motion is controlled by drag produced by its interaction with phonons and electrons of the crystals [52].

A phonon is an elastic vibration propagating through the crystal and is quantized as the lattice is discrete and not continuous [21]. The interaction of the dislocation with thermal vibration, which is phonon drag, and with electrons, is the drag mechanisms that are not thermally activated and include relaxation effects in the dislocation core [21]. At ambient and higher temperatures, when the drag is due to interaction with phonons, the influence of drag acts as the damping mechanism and increases with temperature [52].

In the drag regime, the dislocation velocity is proportional to the applied stress and is determined by the equilibrium between the applied stress and the resistances occurring from the obstacles and drag [21], [52]. The energy stored in the material after deformation as defects is only a small portion of the energy spent to deform it. The residual energy is only 5-20% of the total energy. This implies that most of the energy is dissipated by forces opposing the applied stress due to the viscous behaviour of the solid [21]. The dislocation drag coefficient is defined by the relation [21], [53]:

$$F = Bv \tag{2.15}$$

where, F is the force acting on the dislocation, B is the drag coefficient, and v is the velocity of the dislocation. Equation 2.16 shows the equation for flow stress and it can be seen that the flow stress is proportional to the strain rate in the drag regime [21].

$$\sigma = \frac{2BM}{\rho b^2}\dot{\varepsilon} \tag{2.16}$$

The transition from thermally activated to dislocation drag controlled deformation has been modelled by many researchers by adding the time spent awaiting thermal activation energy to overcome a barrier and the time spent moving to the next barrier [52]. The stress ratio is the ratio of the applied stress to the threshold stress. The value of

the stress ratio at which the transition takes place depends on the strain rate sensitivity of the thermally activated process and only slightly depends on the drag process [52]. The transition stress is lower for higher strain rate sensitivity. The strain rate at which the transition occurs is influenced by the mobile dislocation density and increases with an increase in threshold stress or a decrease in drag coefficient [52]. In the following segment, theory on relativistic effects will be briefly discussed.

2.5.3 Relativistic Effects on Dislocation Motion

The third stage of dislocation motion is the one in which the velocity asymptotically approaches the shear wave velocity [21]. The velocity at which a dislocation moves is limited by the shear wave velocity due to relativistic effects [52]. When the applied stresses are sufficiently high to drive the dislocations at an appreciable fraction of the sound velocity, the relativistic effects, also known as retardation effects, start showing in this region [54]. The acceleration would steadily decrease and it becomes zero when the dislocation velocity becomes equal to the shear wave velocity [21]. The dependence of average dislocation velocity on the applied stress is found to be deviating from the linear behaviour due to relativistic effects, which limit the velocity at higher stresses [52]. Figure 2.9 shows all the three regimes. As we can see, the mean dislocation velocity is limited at high stresses.

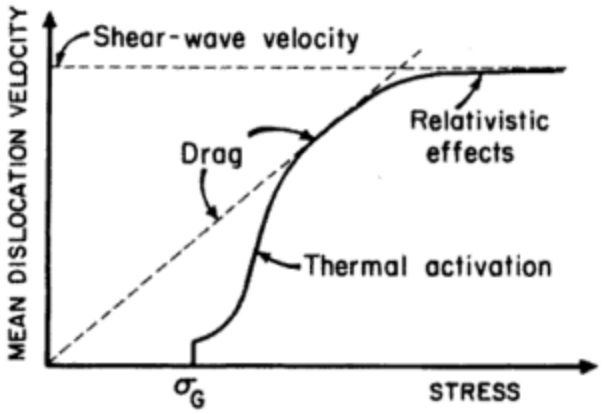

Figure 2.9: Three regimes of dislocation response [21], [52].

Extremely high strain rates are capable of producing high stresses that can lead to relativistic effects. The strain rates achieved from the experiments in this research is in the range of $10^7\ s^{-1}$. This will be discussed later while talking about the results from these experiments. In the next section, the various material models that are used to model deformation at high strain rates will be discussed. Some of them consider thermal activation alone, and in some models, both thermal activation and drag effects are taken into account.

2.6 Empirical and Constitutive Models to Study Dynamic Material Behaviour

Dynamic loading conditions and varying temperatures greatly affect the mechanical behaviour of materials. For example, under shock loading, the strength of a metal increases initially with shock pressure, but at higher stresses, they soften due to thermal effects [55]. The nature of motion of a material possessing strength and features of high rate deformation were studied assuming the material strength to be isotropic [25].

Some of the most important aspects that affect strength include pressure hardening, work hardening, strain rate sensitivity, thermal softening and phase transformation [55]. It is essential to understand the effects of these parameters on strength and other material properties during intense impulsive loading conditions. Several empirical and constitutive models have been developed that closely show the dynamic response of materials under high strain rate conditions.

An Elastic-Perfectly Plastic material model does not account for strain hardening of the material. According to this model, the stress increases linearly with strain until the yield strength is reached, and then the material offers no further resistance to deformation. The stress-strain plot for an elastic-perfectly plastic model is shown in figure 2.10. With elastic-plastic models, calculations of stress and strain distributions at low strains and stresses below S_y are based on linear elasticity [56].

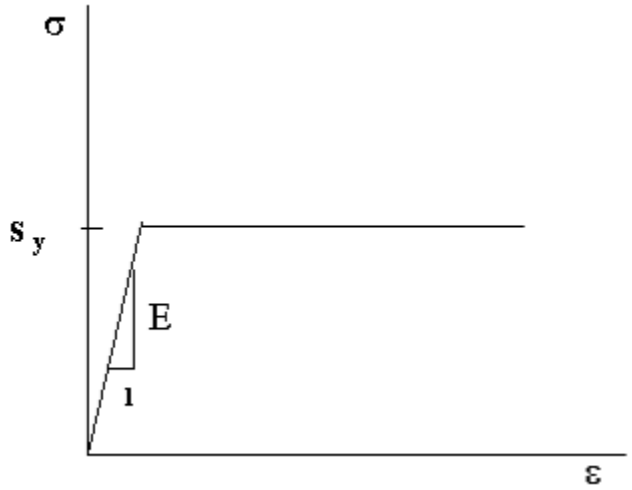

Figure 2.10: Stress-Strain plot for an elastic-perfectly plastic model [57].

The Johnson-Cook model is a constitutive model well suited for computations and available in most of the commercial finite element codes [58], [59]. This model considers

the separated effects of strain hardening (viscosity), strain rate and thermal softening [47, 48]. It is represented by the following equation [58], [59]:

$$\sigma = [A + B\varepsilon^n]\left[1 + Cln\left(\frac{\dot{\varepsilon}}{\dot{\varepsilon_n}}\right)\right][1 - \left(\frac{T-T_r}{T_m-T_r}\right)^m] \tag{2.17}$$

In the above equation, σ is the flow stress, ε is the equivalent plastic strain, $\dot{\varepsilon}$ is the equivalent plastic strain rate, $\dot{\varepsilon_n}$ is the reference plastic strain rate, T is the temperature, T_m is the melting temperature of the work material, T_r is a reference temperature, often taken as room temperature, A is the yield stress, B and n represent the effects of strain hardening, C is the strain rate constant, m is the constant for thermal softening [58]. A, B, n, C and m are material parameters determined based on the flow stress data obtained from mechanical tests [47]. This model can describe the general response of material deformation. However, it is deficient to reflect the static and dynamic recovery, and effects of load path and strain rate history in large deformation processes [47].

The Steinberg-Guinan model is a rate-independent constitutive model valid for $\dot{\varepsilon} \gtrsim 10^5\ s^{-1}$, where $\dot{\varepsilon}$ is the strain rate [60]. It is assumed that the yield strength Y is proportional to the shear modulus G and this is consistent with the neglect of strain-rate-effects [60]. The temperature dependence of Y is also assumed to be the same as G [60]. The model expresses the shear modulus and the yield strength as functions of equivalent plastic strain, pressure and internal energy and accounts for the pressure and temperature dependence of the shear modulus to calculate the relative timing between various waves in a shock-wave experiment [60]. The constitutive relations are as follows [60]:

$$G = G_o[1 + \left(\frac{G_P'}{G_o}\right)\left(\frac{P}{\eta^{\frac{1}{3}}}\right) + \left(\frac{G_T'}{G_o}\right)(T - 300)] \tag{2.18}$$

$$Y = Y_o[1 + \beta(\varepsilon + \varepsilon_i)]^n[1 + \left(\frac{Y_P'}{Y_o}\right)\left(\frac{P}{\eta^{\frac{1}{3}}}\right) + \left(\frac{G_T'}{G_o}\right)(T - 300)] \quad (2.19)$$

$$\text{subject to the limitation: } Y_o[1 + \beta(\varepsilon + \varepsilon_i)]^n \leq Y_{max} \quad (2.20)$$

Here, η is compression, defined as the ratio of initial specific volume υ_o to the specific volume υ, β and n are work-hardening parameters, and ε_i is the initial equivalent plastic strain. Parameters with a subscript 'o' represents their value at the reference state (T=300 K, P=0, ε=0). Primed parameters with subscript P and T imply their derivatives with respect to pressure and temperature at the reference state [60]. Experimental and calculated shock-induced wave profiles were reported in [60] for aluminium. Figure 2.11 from [60] shows the effect of adding P-, T- and ε-dependent terms to the constitutive model.

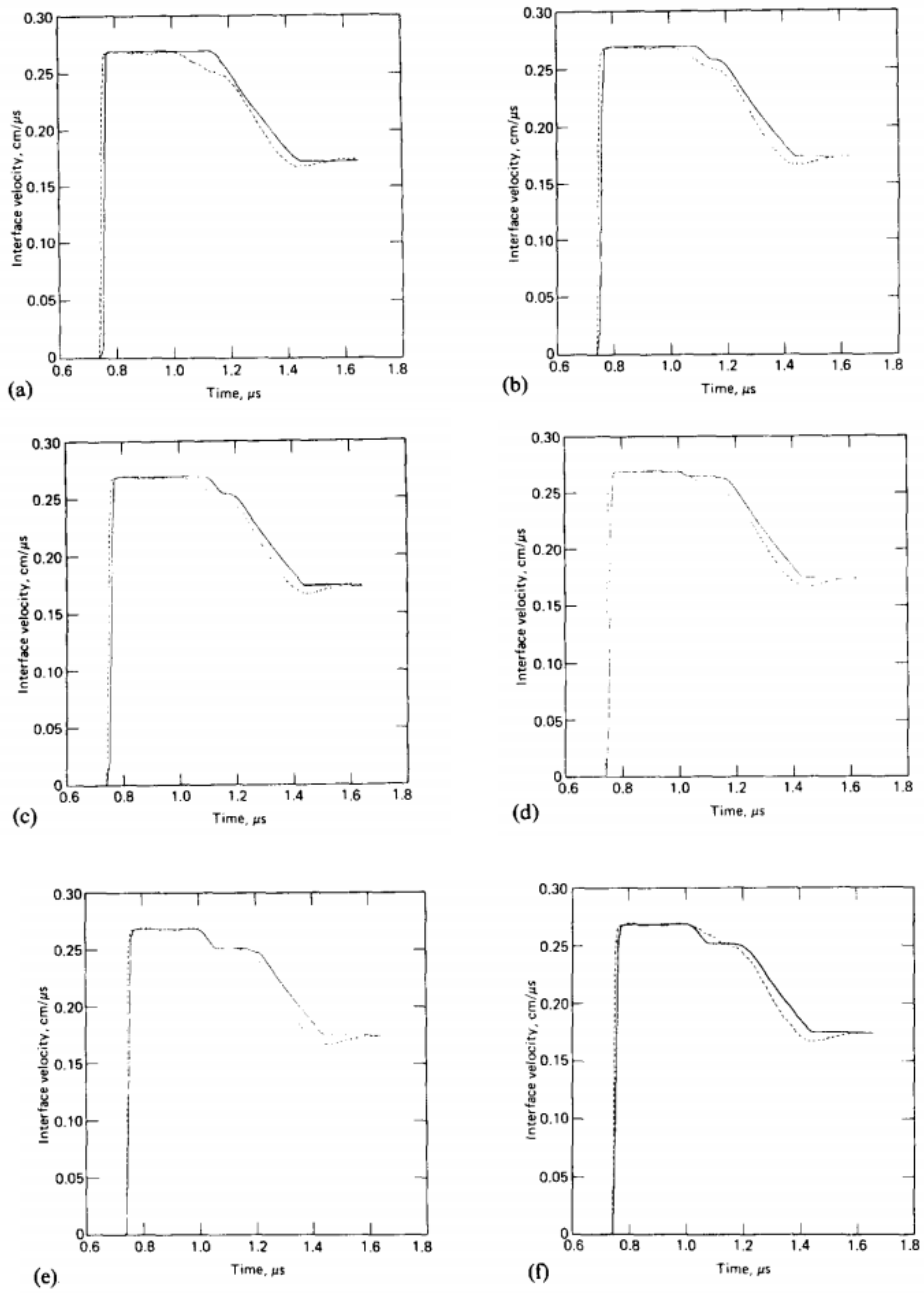

Figure 2.11: a) Pure hydrodynamic b) adding a constant *Y* and *G* c) adding work-hardening d) adding the *P* dependence of *G* e) adding the *P* dependence of *Y* f) adding *T* dependence [60].

One of the limitations of this model is that there is less information regarding the yield strength at high stresses [60]. The experimental data available at low stress was used in [60] along with extrapolation models to predict Y at high pressure and temperature.

The material strength description using simple models such as the elastic-perfectly plastic and elastic-plastic with linear work hardening include thermal softening and show rate dependence to some extent [61]. However, these models are only a numeric fit to test data and can be used only for a limited range of test data. In addition to this, these models do not take the effect of grain size into consideration although it is known that the grain size can have significant effects on the strength and ductility of materials [61].

The Zerilli-Armstrong model is a dislocation-mechanics-based model that takes into account the effects of strain hardening, strain-rate hardening and thermal softening based on thermal activation analysis [61]. The thermal activation behaviour is addressed separately for bcc and fcc metals [61]. The effect of grain size is also taken into consideration. However, the effect of deformation twinning is not included. The constitutive behaviour of each material type is dependent on the dislocation characteristics for that particular structure [61]. The flow stress for the bcc and fcc structures is given by the following equations:

$$\text{For bcc, } \sigma = \Delta\sigma'_G + C_1 \exp(-C_3 T + C_4 T \ln \dot{\varepsilon}) + C_5 \varepsilon^n + k l^{-1/2} \tag{2.21}$$

$$\text{For fcc, } \sigma = \Delta\sigma'_G + C_2 \varepsilon^{1/2} \exp(-C_3 T + C_4 T \ln \dot{\varepsilon}) + k l^{-1/2} \tag{2.22}$$

In the above equation, σ is the flow stress, C_1, C_2, C_3, C_4 and C_5 are model constants, k is the microstructural stress intensity, l is the average grain diameter, and $\Delta\sigma'_G$ is an additional component of flow stress that occurs due to the influence of solute and the

original dislocation density on the yield stress [61]. This relation was used in [61] for iron and copper cylinder impact test. Figure 2.12 shows the plot of radial strain vs distance from the impacted end for copper and iron [61]. It can be observed that the results predicted by the model are much closer to the experimental curve than the Johnson-Cook model.

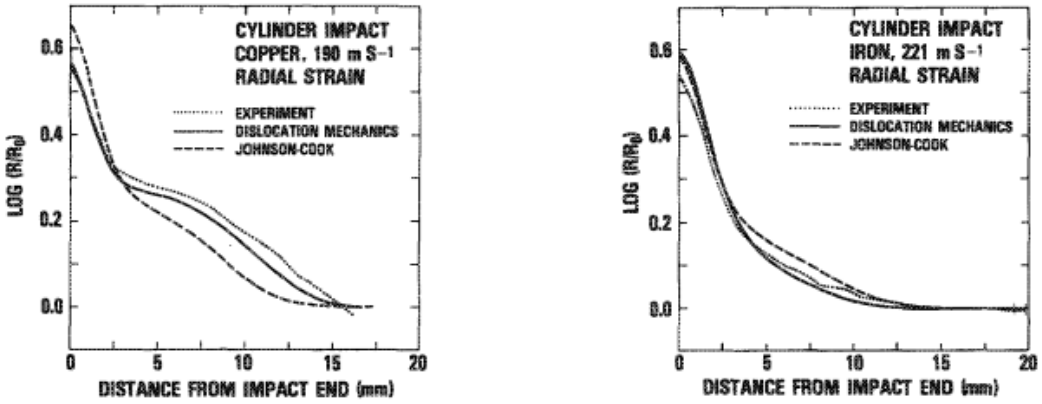

(a) (b)

Figure 2.12: Plot of radial strain vs distance from impact a) Copper b) Iron [61].

The constitutive relations can be applied to very high strain rates and relatively low temperatures, i.e., less than one-half of the absolute melting temperature [61]. However, Voyiadjis et al. pointed out that this model is not applicable to the deformation of metals under high temperature as the strain rate effect on thermal activation area has not been considered [62], [63].

Follansbee and Kocks investigated the axisymmetric deformation of copper at strain rates from $10^{-4}\ s^{-1}$ to $10^{4}\ s^{-1}$ [64]. The mechanical threshold stress, which is the flow stress at 0 K and in the absence of drag or inertia influences, was used as an internal state variable, i.e., it was used as a structure parameter [64]. The variations of flow stress and

the mechanical threshold with strain and strain rate were measured and analysed using thermal activation theory [64]. The strain and strain rate evolution of the mechanical threshold stress is treated by the sum of dislocation generation and dynamic recovery processes [64]. According to [64], the transition in rate controlling deformation mechanism from thermal activation at low strain rates to dislocation drag at high strain rates does not occur at strain rates below $10^{-4}\ s^{-1}$.

The contribution of thermal activation energy reduces the stress required to force a dislocation past an obstacle [64]. The flow stress is expressed as a combination of two components: 1) the rate independent stress that characterizes the interactions of dislocations with long range barriers such as grain boundaries; 2) the rate dependent stress that characterizes interactions with short range obstacles [64]. The relation between the flow stress and the mechanical threshold stress is a function of strain rate and temperature and is given by following equation [64]:

$$\sigma = \hat{\sigma}_a + (\hat{\sigma} - \hat{\sigma}_a)\left(1 - \left[\frac{kT\ln\left(\frac{\dot{\varepsilon}_0}{\dot{\varepsilon}}\right)}{g_0\mu b^3}\right]^{\frac{1}{q}}\right)^{\frac{1}{p}} \tag{2.23}$$

In equation 2.14, $\hat{\sigma}_a$ characterizes the rate independent interactions of dislocations, k is the Boltzmann constant, g_0 is the normalized activation energy, μ is the shear modulus, b is the magnitude of the Burger's vector, and p and q are constants that characterize the shape of the obstacle profile with $0 \leq p \leq 1;\ 1 \leq q \leq 2$ [64]. The dislocation accumulation rate was found to increase with the strain rate as it exceeded $10^3\ s^{-1}$. This was attributed to increased strain rate sensitivity of the flow stress at constant strain in fcc metals at high strain rates [64]. As the strain rate exceeds $10^5\ s^{-1}$,

the strain hardening saturates and the stress-strain behaviour will approach perfect plasticity [64].

In the strong-shock-wave limit, the nonlinear dislocation drag effects are expected to dominate [65]. The mechanical threshold stress model is mostly based on thermally activated dislocation motion and does not consider the effects of dislocation drag. The Preston-Tonks-Wallace (PTW) and the Steinberg-Lund models consider the flow properties of materials in both thermal activation and dislocation drag regimes. In the rest of this section, these two models will be discussed in detail.

The PTW model is applicable at strain rates ranging between $10^{-3}\ s^{-1} - 10^{12}\ s^{-1}$ [66]. It consists of three regimes: 1) thermal activation, 2) dislocation drag (phonon drag), and 3) transition from thermal activation to drag. The dynamic response of a material is assumed to be dependent on the current microstructural state [66]. The material anisotropy is neglected and the shear elastic response and dislocation properties are described by shear modulus alone [66]. The plastic strain rate is of the Arrhenius form and the transition in rate controlling mechanism at very high strain rates is incorporated by combining the Arrhenius form with a power-law dependence [66]. The work hardening is based on an extended Voce law in which there is a linear decrease in the work hardening rate as the saturation stress is reached [66].

At strain rates up to $10^{4}\ s^{-1}$, the strain rate is controlled by thermally activated interaction of dislocations. At higher stresses, it is no more thermally activated and the strain rate dependency shifts to the dislocation drag mechanisms [66]. At plastic strain rates from $10^{9}\ s^{-1}$ to $10^{12}\ s^{-1}$, the work hardening is neglected, and strong shock waves are considered to be in the overdriven shock regime. An overdriven shock wave is one in which the plastic wave has overrun the elastic precursor to produce a front steeper than

that attainable by adiabatic elastic compression [66]. The velocity of the plastic wave becomes greater than the elastic precursor. Heat generated by plastic flow steepens the shock front [66]. Using Wallace's theory of overdriven shock in metals, an estimate of the average deviatoric stress is obtained through heating effect of plastic work [66].

The PTW model combines saturation and yield stresses in thermal activation and drag regimes. The use of error, max and min functions for the saturation and yield stresses allow them to transition smoothly from the low strain rate region, where strength is governed by thermal activation, to high strain rate region, where strength depends on dislocation drag mechanisms [67], [66]. The max function is used to maintain continuity of stress when there is a transition from thermal activation to phonon drag [55]. The abrupt increase in strain rate sensitivity from thermal activation to drag regime is taken care by the min function [55]. The PTW model is represented mathematically by the following set of equations [67], [66]:

The flow stress is given by:

$$\tau = 2\hat{\tau}G \tag{2.24}$$

where, G is the shear modulus and $\hat{\tau}$ is the normalized flow stress, given by the following equation:

$$\hat{\tau} = \hat{\tau}_s + \frac{1}{p}(S_0 - \hat{\tau}_y)\ln\left[1 - \left(1 - exp\left(-p\frac{\hat{\tau}_s - \hat{\tau}_y}{S_0 - \hat{\tau}_y}\right)\right)exp - \left\{\frac{p\theta_\varepsilon}{(S_0 - \hat{\tau}_y)\left[exp\left(p\frac{\hat{\tau}_s - \hat{\tau}_y}{S_0 - \hat{\tau}_y}\right) - 1\right]}\right\}\right] \tag{2.25}$$

Here, $\hat{\tau}_s$ and $\hat{\tau}_y$ are the normalized saturation and yield stresses. They are calculated using equations 2.26 and 2.27.

$$\hat{\tau}_s = max\left\{S_0 - (S_0 - S_\infty)erf\left[k\hat{T}\ln\left(\frac{\gamma\dot{\xi}}{\dot{\varepsilon}}\right)\right], S_0\left(\frac{\dot{\varepsilon}}{\gamma\dot{\xi}}\right)^{\beta}\right\} \tag{2.26}$$

$$\hat{\tau}_y = max\left\{Y_0 - (Y_0 - Y_\infty)erf\left[k\hat{T}\ln\left(\frac{\gamma\dot{\xi}}{\dot{\varepsilon}}\right)\right], min\left[Y_1\left(\frac{\dot{\varepsilon}}{\gamma\dot{\xi}}\right)^{Y_2}, S_0\left(\frac{\dot{\varepsilon}}{\gamma\dot{\xi}}\right)^{\beta}\right]\right\} \tag{2.27}$$

$\dot{\xi}$ is a strain rate variable defined by the following equation:

$$\dot{\xi} = \frac{1}{2}\left(\frac{4\pi\rho}{3M}\right)^{1/3}\left(\frac{G_0}{\rho}\right)^{1/2} \tag{2.28}$$

Here, M is the atomic mass (kg per atom) and ρ is the density. The pressure dependent shear modulus is given by:

$$G = G_0(p)(1 - \alpha_p\hat{T}) \tag{2.29}$$

$G_0(p)$ is the shear modulus at zero pressure. $\hat{T}$ is the ratio of the current temperature, T to the melting temperature, T_m, and provides a thermal softening term.

$$\hat{T} = \frac{T}{T_m} \tag{2.30}$$

In the above equations, S_0, S_∞, Y_0, Y_∞, Y_1, Y_2, p, θ_ε, k, γ, $\dot{\xi}$, β, α_p, are material parameters. $S_0, S_\infty, Y_0, Y_\infty, Y_1, Y_2, p, \theta_\varepsilon, k, \gamma$ are derived from experimental data.

The PTW model is applicable to very high strain rates and can be used to study various aspects of shock loading in materials at such extremities. The Steinberg-Lund is another model that also considers the effect of temperature and drag and will be discussed in the next segment of this section.

The Steinberg-Lund model is applicable to strain rates from $10^{-4}\ s^{-1}$ to $10^{6}\ s^{-1}$ [68]. The yield strength is given by the following equation [68]:

$$Y = \left[Y_t\left(\dot{\varepsilon}_p, T\right) + Y_a f(\varepsilon_p)\right]\left[\frac{G(P,T)}{G_0}\right] \tag{2.31}$$

where, $Y_t\left(\dot{\varepsilon}_p, T\right)$ is the thermally activated part of the yield strength and is a function of plastic strain rate $\dot{\varepsilon}_p$ and temperature T, $Y_a f(\varepsilon_p)$ is the athermal part of the yield strength and is calculated using equation 2.10 from the Steinberg-Guinan model [60], with $f\left(\varepsilon_p\right)$ as the work-hardening term, which is a function of equivalent plastic strain, $G(P,T)$ is the pressure and temperature dependent shear modulus and G_0 is the shear modulus at standard temperature and pressure (STP) conditions [68].

At moderate strain rates, the Peierls mechanism, in which dislocation kinks are created by thermal activation, is rate controlling; at higher rates, it is dominated by dislocation drag [69]. The equation for the plastic strain rate combines these effects and adds the time spent in thermally activated part and dislocation drag. It is represented by the following equation [69], [68]:

$$\dot{\varepsilon}_p = \left\{\frac{1}{C_1} exp\left[\frac{2U_k}{kT}\left(1 - \frac{Y_t}{Y_p}\right)^2\right] + \frac{C_2}{Y_t}\right\}^{-1} \tag{2.32}$$

where, Y_p is the Peierls stress, $2U_k$ is the energy to form a pair of kinks is a dislocation segment of length L, k is the Boltzmann constant. The constants C_1 and C_2 are given by the following equations:

$$C_1 = \frac{\rho L a b^2 \nu}{2w^2} \tag{2.33}$$

$$C_2 = \frac{D}{\rho b^2} \tag{2.34}$$

$$\text{Condition: } Y_t \leq Y_p \tag{2.35}$$

Here, ρ is the dislocation density, a is the distance between Peierls valleys, w is the width of a kink loop, ν is the Debye frequency, D is the drag coefficient, and b is the Burgers' vector [68].

In this model, the plastic response is rate-dependent only below the Peierls stress, as given in equation 2.26. As the thermally activated part of the yield stress exceeds this threshold, the equation predicts a drop in flow stress, making it unphysical once $Y_t > Y_p$. Hence, the model assumes rate independence in order to keep $Y_t = Y_p$. To make the model physically meaningful for stresses above Y_p, Wang et al. proposed to replace equation 2.32 with the following [69]:

$$\dot{\varepsilon}_p = \left\{ \frac{1}{C_1} exp\left[\frac{2U_k}{kT} sign(Y_p - Y_t)\left(1 - \frac{Y_t}{Y_p}\right)^2 \right] + \frac{C_2}{Y_t} \right\}^{-1} \tag{2.36}$$

Using equation 2.36, $\left|\dot{\varepsilon}_p\right|^{-1}$ can be defined even in the region where $Y_t \geq Y_p$ [69]. Thus, the modified model is always rate dependent and the rate controlling mechanism transitions from thermal activation at low strain rates to dislocation drag at high strain rates as the thermal component approaches the Peierls stress [69]. The dislocation drag constant C_2 controls the rate dependence of the flow stress at high strain rates [69]. Figure 2.13 from [69] shows a plot of plastic strain rate vs Y_t for tantalum, comparing Steinberg-Lund with the modified model.

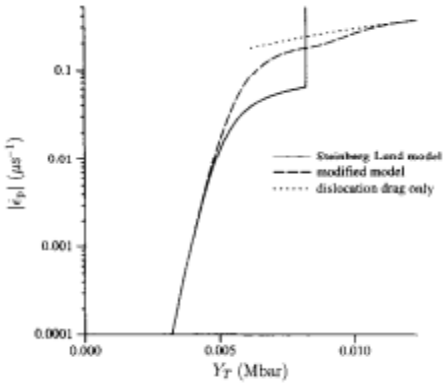

Figure 2.13: Plot of plastic strain rate vs Y_t comparing Steinberg-Lund and the modified model [69].

The Steinberg-Lund model becomes vertical at $Y_t = Y_p$, due to the assumptions made by the model, leading to rate independence. The rate dependence can be clearly seen in the modified model. The dislocation drag curve shows the dominance of the drag constant in the high strain rate region [69].

The strength models described above are used to study the materials strength and their dynamic behaviour under high pressure and strain rate conditions. Researchers are using hydrodynamic instabilities in their experiments to study dynamic material strength [18], [15], [12]–[14], [16], [17]. In this research, perturbations are created on the geometry to apply the hydrodynamic instability approach and this is used to determine the effects of strength through the nature of it evolution. In the following section, the most commonly used instabilities in these experiments, i.e., Rayleigh-Taylor (RT) and Richtmeyer-Meshkov (RM) will be briefly discussed.

2.7 Determination of Material Strength using Hydrodynamic Instabilities

In inertial confinement fusion applications, implosions tend to be inherently unstable due to the growth of amplified disturbances known as instabilities [8]. The geometry of an ICF capsule makes them susceptible to various types of hydrodynamic instabilities at different stages of an ICF implosion [70]. These instabilities initially destroy the imploding shell, which greatly affects the formation of the central hot spot. Controlling the growth of the instability is critical as it affects the central hot spot ignition. Successfully igniting an ICF capsule has always been a big challenge. A bi-material interface with a difference in density between the two materials can trigger the instability [8]. The various stages of ICF and the growth of an instability in each stage can be seen in figure 2.14.

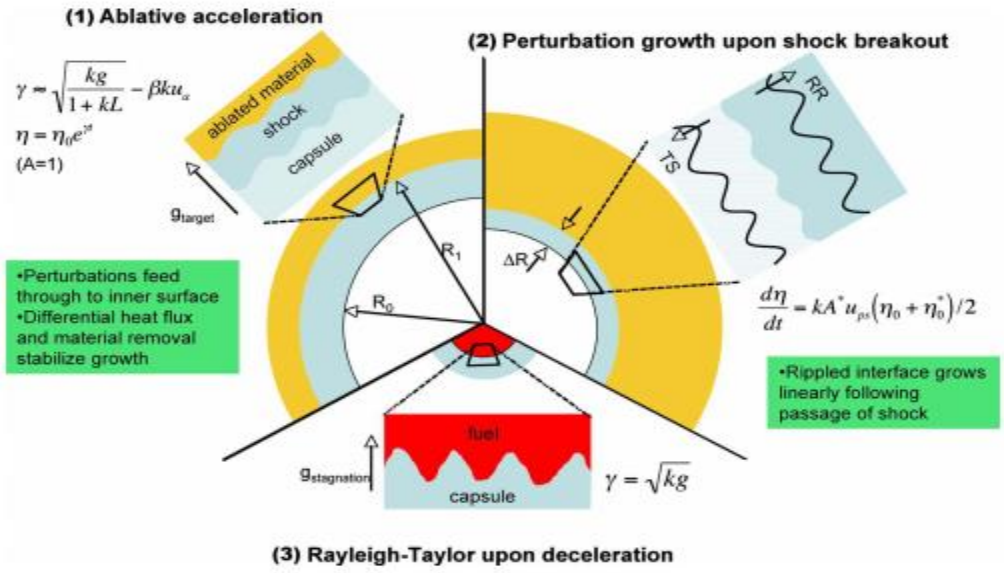

Figure 2.14: Three stages on ICF implosion and the hydrodynamic instabilities developing at each stage [70].

Perturbations on any interface in an ICF capsule have the ability to communicate their structure to any other interface, making them coupled in space and time [70]. The ablated surface will undergo RM oscillations initially, which when accelerated leads to RTI growth. RT at the ablation surface can possibly break up the capsule if the perturbations grow to larger amplitude [70]. The growth of instabilities at the perturbed interface is characterized by growth rate γ, wave number k, acceleration in the frame of the interface g, ablation velocity u_a, pre- and post-shock perturbation amplitude η and density scale length L. The mechanisms involved are explained in detail in [70].

Researchers have been studying all aspects of various types of instabilities for the last two decades and significant progress has been made based on theory, simulations and experiments [8]. The RT and RM instabilities, which are common in ICF, have been used to study material strength due to the high influence of strength on their behaviour and the existence of experimental capabilities that record dynamic and transient data at the time of their evolution [18], [15], [12]–[14], [16], [17]. This section will briefly discuss RT and RM instabilities and their application to study material strength.

2.7.1 Rayleigh-Taylor Instability

The Rayleigh-Taylor instability (RTI), also known as the gravitational instability, arises at an interface of different density materials, when an acceleration perpendicular to the interface is directed from the lower density material to the higher density material [71]. The concept of RTI can be easily understood by associating it with fluids. The instability occurs at the interface of two fluids with different densities when the heavy fluid is pushing the light fluid. This causes a jump in the tangential component of velocity across the interface. The interface remains stable if the reverse process occurs [72]. An example of RTI formation is shown in figure 2.15.

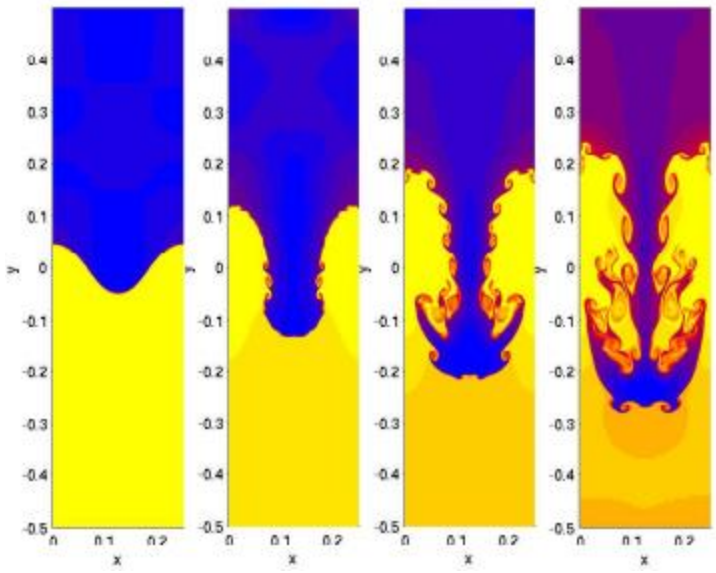

Figure 2.15: An example of Rayleigh-Taylor Instability formation [73].

The same concept can be applied to an ICF shell driven by hot ablating plasma. When the acceleration is directed inward towards the interface, which is the inner surface of the ICF shell, it becomes unstable due to inertial force acting in the opposite direction [8]. Figure 2.16 shows the distinction between the two configurations discussed above. In 2.16 a, the heavier fluid is above the lighter fluid and instability occurs due to gravity. In 2.16 b, the lighter fluid accelerates the denser fluid [8].

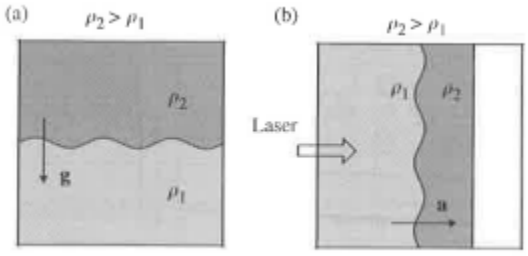

Figure 2.16: a) System of two fluids where, the lighter fluid supports the denser one b) A lighter fluid accelerates a layer of denser fluid [8].

According to the linear stability theory, the classical RTI growth rate is given by the following equation [8]:

$$\sigma_{RT} = \sqrt{\frac{2\pi A_t a}{\lambda}} \tag{2.37}$$

and, the perturbation amplitude, which grows exponentially in time, is given by [8]:

$$\zeta = \zeta_0 \exp(\sigma_{RT} t) \tag{2.38}$$

In equations 2.31 and 2.32, a is the acceleration, λ is the wavelength of the perturbations, ζ_0 is the initial amplitude, $k = \frac{2\pi}{\lambda}$ is the wave number, and A_t is the Atwood number of the interface defined by [8]:

$$A_t = \frac{\rho_2 - \rho_1}{\rho_2 + \rho_1} \tag{2.39}$$

Elastoplastic materials play a key role on the physics of RTI in solids and this complex phenomenon has been analyzed in materials with elastic or plastic properties [13]. The initial perturbations in the interface or velocity field are extremely small and they grow exponentially with time. As the growth becomes non-linear, the development is strongly influenced by three dimensional effects [72]. The RTI occurs in solids when accelerated by a low density fluid. The material strength plays a key role in stabilizing or reducing the perturbation growth [12], [74]. Barnes et al. studied RTI by observing the growth of perturbations on the surface of a flat plate. The accelerated plates had uniform sinusoidal perturbations on the surface contacted by high-explosives (HE) and were smoothly accelerated by expanding detonation products [12]. Using a 2D elastic-plastic numerical hydrodynamics code, it was determined that the amplitude growth was largely governed by the dynamic yield strength of the material [12].

He et al. also did a similar work on aluminium plates using high explosives [74]. At first, they assumed that the aluminium material was a fluid and used only the equation of state. Then it was considered as an elastic-plastic solid, i.e., both the equation of state and the Steinberg-Guinan constitutive model were used [74]. The driven surface of the aluminium plates had a sinusoidal perturbation and the opposite side was made flat. The perturbation growth factor, which is the perturbation amplitude growth divided by initial perturbation amplitude, comes from multiples of initial perturbation amplitudes. There was an existence of a cut-off wavelength for the RTI in the case where the material was assumed to be elastic-plastic. The growth of perturbation was stable for shorter wavelengths, i.e., when perturbation wavelength was smaller than the critical wavelength. The growth was found to increase rapidly with an increase in wavelength [74].

Piriz et al. presented an analytical one-degree-of-freedom model for the RTI based on second law of Newton, to deal with the instability of accelerated elastic solids [13]. The model describes the transient phase between initial conditions and the asymptotic instability growth rate and shows how the perturbation growth in the asymptotic regime depends on the initial conditions [13]. The model was applied to solid/solid and solid/fluid interfaces. For each of these considerations, expressions have been derived for the total force, the equation of motion, the growth rate, the cut-off perturbation wave number, and the perturbation amplitude as a function of time for both stable and unstable cases [13]. The theory and equations of this model applied to perfectly elastic solids, that considers interfaces of solid/solid, solid/vacuum, and solid/viscous fluid, and to rigid plastic solids, are completely elaborated in [13]. The authors have stressed the importance of initial conditions as the perturbation amplitude will be affected by the initial velocity and acceleration and the RT phase may start from a surface at rest in a

stress-free material, or it could be triggered by RMI, and/or, by a transient phase in which the driving pressure increases after reaching a constant value [13]. Later, the model from [13] was used by Piriz et al. to study RTI in elastic-plastic solids [14]. The linear analysis was carried out for thick solid plates with elastic-plastic constitutive properties that were accelerated uniformly by a constant pressure [14]. It was found that the transition from elastic to plastic regime is a necessary condition, but not a sufficient one for instability [14].

Park et al. presented experimental results showing reduction in RTI growth in polycrystalline vanadium when it was subjected to high pressure and strain rate [75]. Samples were compressed and accelerated quasi-isentropically at ~1 Mbar pressures, while maintaining the samples in the solid-state [75]. The microscopic change in the lattice structure under compression can have a significant effect on the macroscopic properties of the material. Loading materials to high pressure using shocks causes heating, potentially melting the material [75]. Hence, to reach high pressures under nearly isentropic conditions, a laser is used to drive a strong shock through a low-Z reservoir, which unloads as a rarified plasma across a vacuum gap, that then stagnates on the sample [75]. The vanadium sample was pre-imposed with sinusoidal ripples and the back was polished flat. The sample was thermally insulated with CH-based epoxy to overcome the heat created by the stagnating plasma [75]. The experimental setup is shown in figure 2.17.

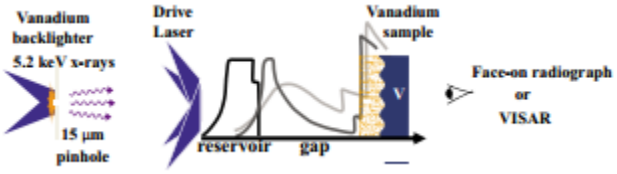

Figure 2.17: Schematic of the experimental configuration [75].

As seen in figure 2.17, the drive laser shocked the plastic reservoir, which releases across a vacuum gap as flowing plasma. This generates a ramped pressure drive on the vanadium sample [75]. Face-on radiography was used to measure the growth of RTI using a synchronised, laser-driven x-ray backlighter. A VISAR was used to measure the pressure profile by replacing the vanadium with aluminium backed by a LiF window [75].

The growth factor is defined as the amplitude of the perturbations at time *t* divided by the initial amplitude of the perturbations [75]. Calculations of the RT growth factor were compared with 2D hydrodynamic simulations using Steinberg-Guinan and PTW models [75]. Figure 2.18 a depicts density plots obtained from the simulations using PTW strength model and no-strength model. The growth rate of RTI can be reduced to a great extent when the material has strength [75]. The comparison of growth factors between experimental and simulation is shown in figure 2.18b. The models predict a higher value than the experiment [75]. The model parameters were varied to match the experimental data. The authors theoretically attribute this increase in strength to strain rate effects [75]. The experimental strain rate was calculated and both Steinberg and PTW models show that the high rate deformation occurs in the phonon drag regime [75].

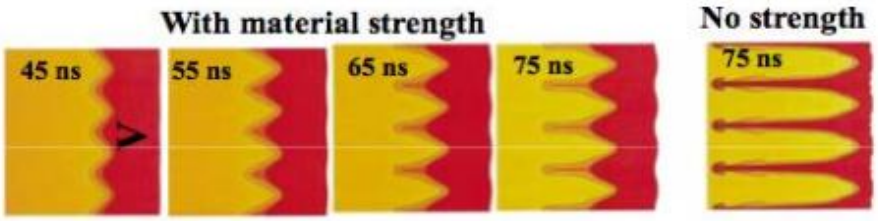

(a)

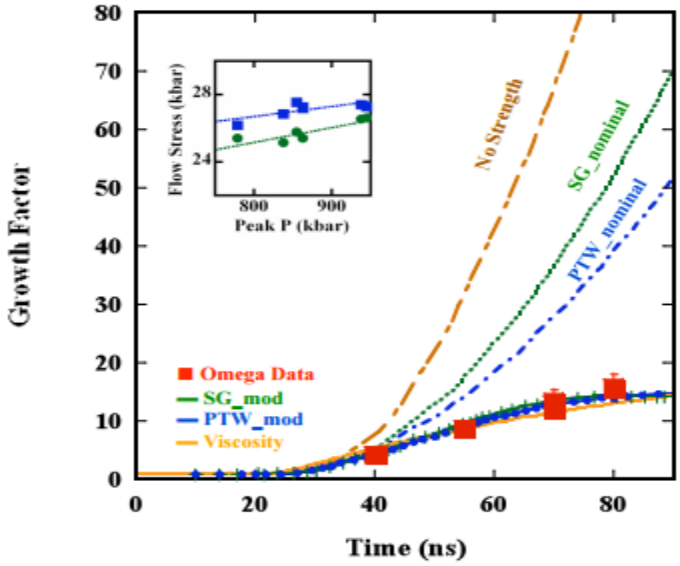

(b)

Figure 2.18: a) Density plots with PTW model at different times and No-strength model at 75 ns; b) Plot of growth factor vs time comparing experiments and simulations [75].

Olson et al. assessed the effect of microstructure and material processing of copper on the RTI growth utilizing the experimental technique from Barnes et al [12], [76]. Different polycrystal grain-sizes, single crystal and strain hardened samples were dynamically tested by keeping the dynamic loading conditions and sample geometry constant [76]. It was observed that the crystallographic orientation of single-crystals affected the perturbation growth [76]. The strain hardening was found to increase the dynamic strength at strain rates above $10^5\ s^{-1}$ [76]. The grain boundary strengthening did not have considerable effects in the loading conditions used in [76]. Aglitskiy et al. studied the evolution of perturbations on the free rippled surface of a plastic target that was triggered by a laser-drive shock wave breakout [77]. At sub-megabar pressure, the RM instability follows the shock break out in the non-accelerated target [77]. An

oscillatory rippled expansion wave was observed with increase in pressure and this triggered the RT instability as the target was accelerated due to the interaction of rear-surface perturbations with the ablation front [77].

From the above discussions on various research done on RTI, we can see that the growth of RTI is influenced by a range of factors such as microstructure, material strength, initial conditions like the initial velocity and acceleration and controlling the load and applied pressure. In some of the research papers discussed here, it has also been clearly indicated that even though RT is a dominant phenomenon in ICF applications, it is more likely that it can be triggered by the RM iinstability [13], [77]. Therefore, it is essential to study the evolution of the RM instability and the effects of material strength on its growth. One of the advantages of RMI is that it has a slow linear growth rate, due to which, the behaviour of RMI in a material can be recorded using experimental techniques like Transient Imaging Displacement Interferometry (TIDI), thereby making it easier to model [18], [15]. The RM instability will be briefly discussed in the next segment of this section.

2.7.2 Richtmeyer-Meshkov Instability

The Richtmeyer-Meshkov instability (RMI) is caused by a shock wave passing through the interface of two different density materials, which is not perfectly flat, and in a direction perpendicular to the interface [8], [71]. The interface is accelerated impulsively and then moves without any acceleration. The interface moves at an acceleration behind the wave front when the shock wave is time dependent [61]. The interface seems to be discontinuous and the region over which the properties change across the interface can be infinitely thin [10]. The amplification of perturbations at the interface is due tovorticity generation resulting from the misalignment of the pressure

gradient of the shock and the local density gradient across the interface. In ICF applications, the RMI causes mixing between the capsule material and the fuel within, which will limit the final compression and affects the ability to achieve energy production [10]. Figure 2.19 shows the formation of the RM instability caused by a moving shock wave. The passage of the shock suddenly distorts the boundary, and imparts a non-uniform velocity [8]. RMI can produce seeds, which are later amplified by a more violent RTI [8].

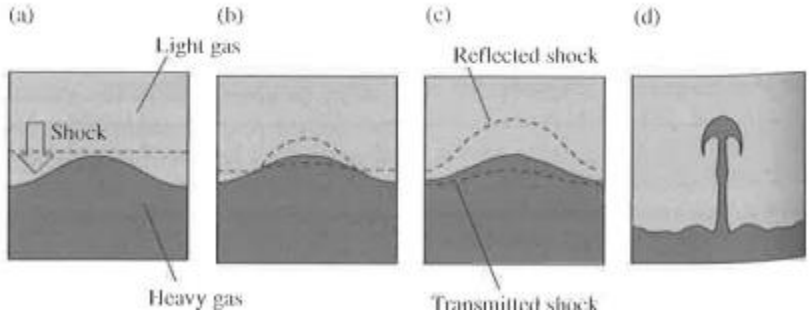

Figure 2.19: Formation of RMI caused by a moving shock wave [8].

The equation for the RMI growth rate is given by Richtmeyer (1960) using the impulsive model [8].

$$\sigma_{RM} = A_t k \Delta u \tag{2.43}$$

Here, A_t is the Atwood number, the value of which is taken just after the transit of the shock wave, k is the wave number, and Δu is the velocity increment caused by the transit of the shock at time t=0. The equation for the perturbation amplitude as a function of time is as follows [8]:

$$\zeta(t) = \zeta_0(1 + \sigma_{RM} t) \tag{2.44}$$

where, ζ is the amplitude of the unstable interface, and ζ_0 is the initial surface amplitude [8]. From the above equation, it is evident that the perturbation amplitude varies linearly in time [8]. Once the shock has crossed the interface, the mechanism driving the instability ceases and the evolution of RMI is due to inertia [8]. RMI occurs both for a shock propagating from a light material to a denser one and vice-versa[8]. When the shock propagates from a denser medium to a lighter one, the instability reverses the sign of the perturbation amplitude [8].

Piriz et al. presented an analytical model for the linear RMI in solids under conditions of high-energy density, to describe the evolution of small perturbations at the solid-vacuum interface [18]. It is assumed that the perturbations are incompressible and the shocked material behaves similar to an elastic-perfectly plastic medium described by Prandtl-Reuss flow rule with the von Mises yield criterion as it was done in [78]. The asymptotic evolution of the interface after an initial transient phase is described by considering the fact that the only force acting on the interface is the one due to shear stress, which is described by the deviatoric part of the stress tensor [18]. In order to represent the Hugoniot of the solid, the Mie-Gruneisen equation of state and the linear relationship between shock velocity and the particle velocity as in equation 2.10 is used. The following equations were derived to describe the interface evolution in terms of the effective yield strength S_y [18]:

$$\rho \frac{\alpha}{k} \ddot{\xi} = -S_y \tag{2.45}$$

$$S_y = \begin{cases} \sqrt{\frac{2}{3}} \frac{Y}{\alpha |M|}, k\dot{\xi} > 0, \xi \geq \xi_p \\ 2\frac{k}{\alpha} G\left(\xi - \bar{\xi}\right), k\dot{\xi} < 0, \xi \leq \xi_p \end{cases} \tag{2.46}$$

$$|M|^2 = \frac{2}{\alpha^2} \tag{2.47}$$

Here, Y is the yield strength, ρ is the post-shock density of the material, k is the wave number, α is a numerical factor that expresses the ignorance about the exact velocity field, ξ_i is the initial amplitude of perturbation when the material is stress-free and the subscript *'p'* represents the perturbation amplitude in the plastic regime, and G is the shear modulus [18].

For the initial elastic phase [18]:

$$\xi_p - \xi_i = \sqrt{\frac{2}{3}} \frac{1}{2|M|} \frac{Y}{kG} \tag{2.48}$$

At time $t=t_o$, the amplitude has already overcome the elastic limit [18]:

$$\xi_0 - \xi_i \geq \sqrt{\frac{2}{3}} \frac{1}{2|M|} \frac{Y}{kG} \tag{2.49}$$

The transition of the perturbation amplitude into different regimes with time can be explained with the help of figure 2.20.

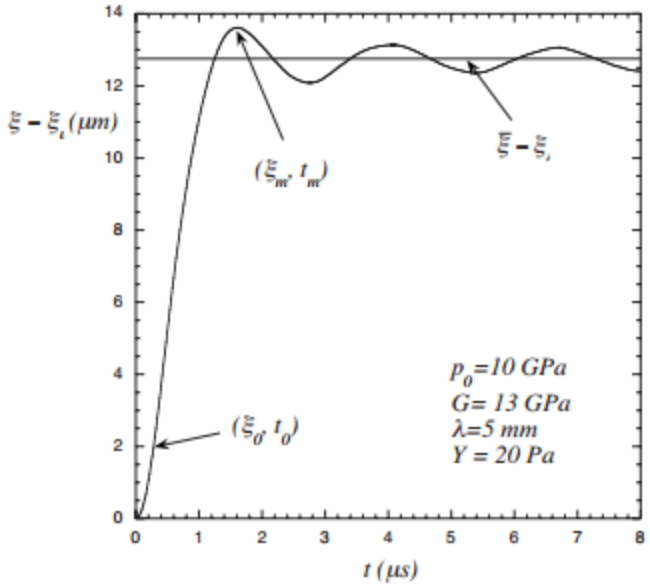

Figure 2.20: Relative perturbation amplitude as a function of time [18].

If the condition $k\dot{\xi} > 0$ is satisfied, the later evolution will take place in the plastic regime [18]. In every case, the amplitude will grow to a maximum value at a particular time, and after that, the material remains oscillating between the region above and below $\overline{\xi} - \xi$ with a constant amplitude, which is represented by the horizontal line [18].

Piriz et al. applied this model to [15], in which RM instability was used as a tool for evaluating material yield strength of solids at shock pressures below the melting pressure value. An aluminium plate was considered, with perturbations imposed on the front of the plate, and with symmetry boundary condition at the edges [15]. Numerical simulations were run for different values of yield strength, shear modulus, perturbation wavelength and pressure [15]. Figure 2.21 shows the plot of relative perturbation amplitude as a function of time for different values of yield strength.

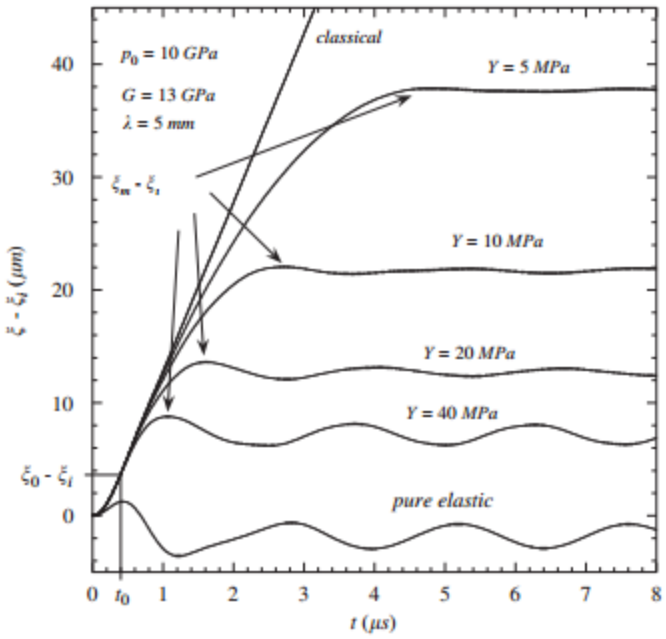

Figure 2.21: Relative perturbation amplitude as a function of time for different values of yield strength obtained from 2D numerical simulations [15].

During an initial transient phase, the material is not affected by the constitutive properties and evolves similar to a classical case for an ideal fluid [18], [15]. The perturbation growth is similar to a fluid during the interval $0 \leq t \leq t_0$. After the initial transient phase, i.e., when $t \geq t_0$, the perturbation grows to a maximum value ξ_m at time t_m depending on the yield strength of the material, and then it remains oscillating elastically around a mean value $\bar{\xi}$ for time $t \geq t_m$ [18], [15]. The amplitude of elastic oscillations taking place at $t \geq t_m$ is much less than the maximum amplitude [15]. The following expression can be obtained by applying a scaling law with $\bar{\xi} \approx \xi_m$ and $\xi_0 \sim \xi_i$ [15]:

$$\bar{\xi} - \xi_i \approx \frac{\alpha \rho \xi_0^2}{kY} \tag{2.50}$$

The above equation can be used to evaluate the yield strength Y, from a single measurement of the amplitude taken at relatively long times, i.e., for $t \geq t_m$ [15]. However, this method is based completely on simulations and has not been tested experimentally or on real materials [4].

Dimonte et al. used the RMI at a metal-gas interface to determine the yield stress of the metal under shock loading and release [4]. The authors also described an ejecta transition, wherein the formation of saturated spikes and bubbles determined the velocity of ejecta [4]. When the shock arrives at the free surface, material can be ejected in the form of fine spray and this ejection of material is called ejecta [79]. This jetting of material is due to the reflection of strong shock waves from the surface [79]. Buttler et al. presented a physics- based ejecta model using RMI to study various aspects of spikes and bubble formation [80], with a basic initial and final geometries shown in figure 2.22.

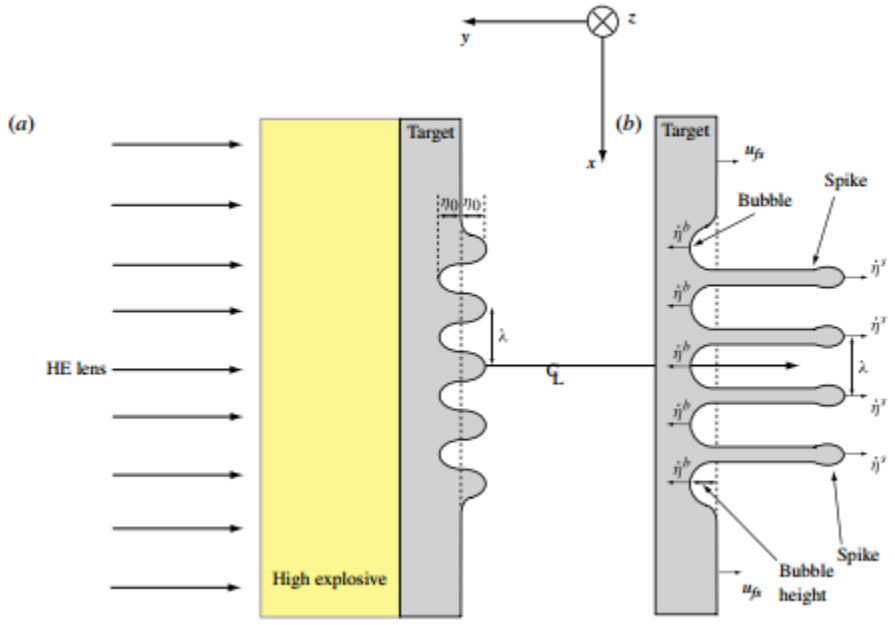

Figure 2.22: a) Pre-shocked and b) Post-shocked geometry of the sample [80].

Dimonte et al. estimated an average RMI yield in the perfectly plastic regime as a function of the amplitude of the spike [4].

$$Y_{RMI} \sim 0.24\rho_A \frac{|V_{sp}^0|^2}{k h_{sp}^{max}} \tag{2.51}$$

Here, Y_{RMI} is the RMI inferred yield stress, ρ_A is the density, V_{sp}^0 is the velocity of the spike, k is the wave number, and h_{sp}^{max} is the scaled amplitude of the spike [4]. This was compared with direct yield predictions under the same conditions using molecular dynamics simulations [4].

As we can see, in some of the research papers discussed so far, the sample was perturbed on one end and flat on the other end. The flat end of the sample was shock loaded and the perturbations grew once the shock arrived at the rippled interface. When this experimental method is used to study RMI growth and the influence of strength, it is also essential to take into account the driving condition such as the shock pressure and the effect it may have on ejecta transition.

Opie et al. used an experimental setup that was somewhat different from the conventional method, to study the effect of strength of copper and phase transformation kinetics of iron on a rippled shock [19]. In this setup, the shock originated from the perturbed surface of the sample and the flat surface was treated as the free surface [19]. The shocked surface of the sample had perturbations in the form of a square wave and these perturbations were imprinted on the sample by photolithography [19]. The sample was shock loaded to about 10 to 30 GPa pressures by laser ablation, wherein the laser pulses lasted for ~5 ns. The material strength/phase regimes were determined by the pressure, which was controlled by varying the laser intensity [19]. The velocity at the diagnostic surface was recorded using a line VISAR [46] and the out of plane

displacement measurements, i.e., the evolution of the RM instability, were recorded using TIDI [48]. Figure 2.23 shows the schematic of the experimental setup that was used in [19].

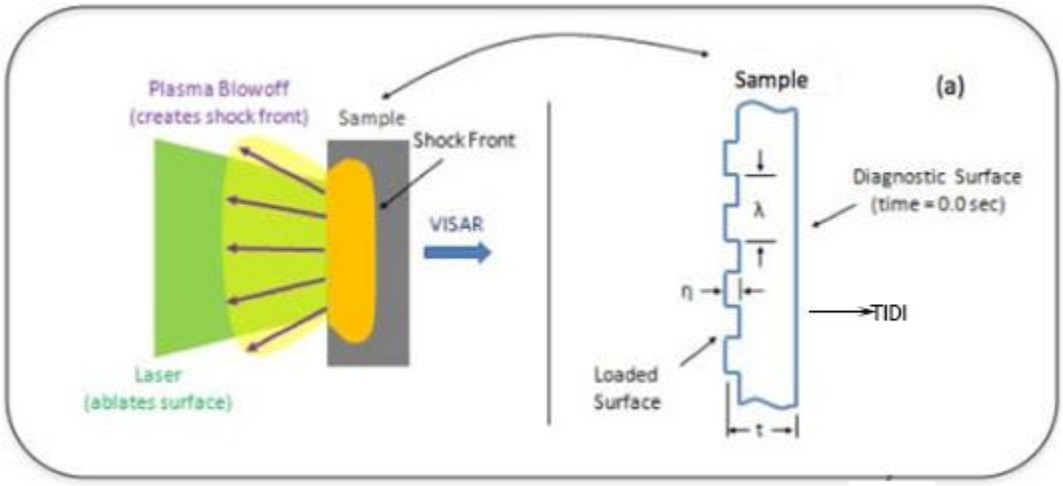

Figure 2.23: Schematic of the experimental setup used in [19].

The test was done on two sample geometries: samples with both ends flat and samples with one end perturbed [19]. The velocity history from the shocked flat samples was used to calibrate the pressure boundary condition as a function of laser energy, which was used to obtain the driving pressures for rippled samples [19]. Laser ablation of the rippled samples produced a rippled shock front that travelled through the sample and imprinted the initially flat free surface with perturbations, which then grew as a result of the RM instability [19]. Two framing cameras were used to obtain two dynamic images per sample in which the extent of growth of perturbations on the flat surface can be seen [19]. Figure 2.24 shows VISAR images for flat and rippled samples along with the velocity history and the out-of-plane displacement at the free surface [19].

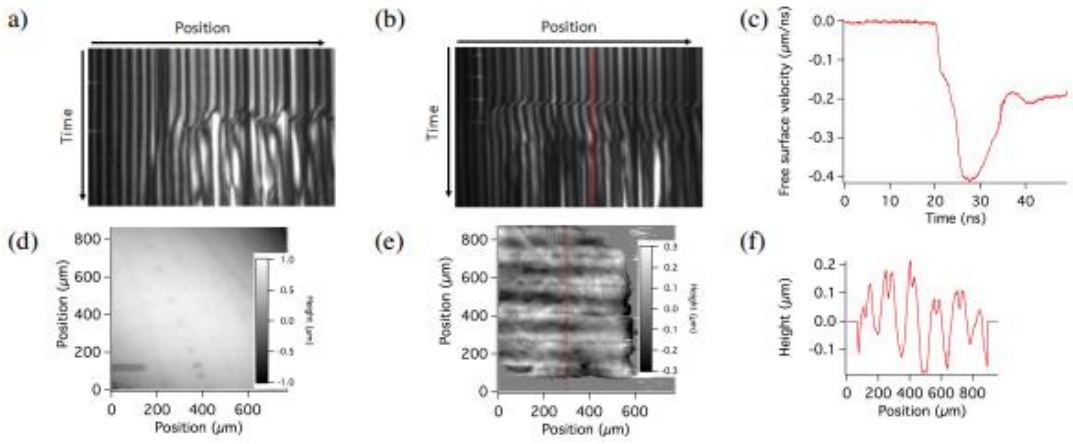

Figure 2.24: a) Line VISAR image of a rippled sample; b) Line VISAR image of a flat sample; c) Velocity history of a flat sample; d) Pre-shock TIDI image; e) Post-shock TIDI image; f) Displacement data after post processing [19].

As seen in figure 2.24 c, the velocity history of the flat sample was typical of the one obtained from laser ablation or plate impact experiments. This indicated that the surface accelerated and decelerated as a whole with the shock front and release wave [19]. On the other hand, the free surface of the rippled samples had perturbations with a wavelength equal to the wavelength of the ripples, and evolved higher harmonics with time due to the interaction with the release wave [19].

Simulation were run using the PTW model [66] and the unitless model parameters of iron and copper were adjusted to match the velocity profiles of flat samples [19]. These parameters play a major role in controlling the strain rate sensitivity and the characteristics of material in the thermal activation and phonon drag regimes. The displacement data from TIDI, i.e., the amplitude of perturbations evolved on the free surface was also compared with the simulations. The strength parameters were found to have a significant effect on the sensitivity of perturbation growth [19].

It was observed that the perturbed shock front profile travelling through the sample was less perturbed in samples with increased strength [19]. The transformation rate and the energy barrier constant were varied for iron to match the experimental data. Faster kinetics in iron led to more uniform pressure contours and also increased the strength of the material. The simulations predicted smaller permanent deformations relative to transient deformations as the shock reached the free surface, and indicated a quasi-linear growth rate of the transient perturbations for a pressure pulse that was sustained for a longer time. The effects of strength on the perturbation growth can be seen in figure 2.25.

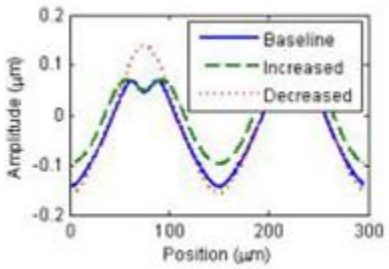

Figure 2.25: Displacement at the free surface from simulations, showing the effect of strength in copper [19].

In this section, two different approaches have been discussed in regards to the RM instability and its sensitivity to material parameters. As already discussed, the conventional method, in which the shock travels from the flat surface, is more prone to ejecta transition. On the other hand, in the experimental setup proposed by Opie et al., the shock front is already rippled and significant results from [19] show that the amplitude of this shock front is affected by the material properties as it travels through the sample. The novel experimental setup from [19] is used in this research to get

experimental dynamic data, which is in turn used to study the effect of strength and validate various material models.

There is another important phenomenon in shock physics, called dynamic spallation that takes place in shock experiments due to the superposition of tensile release waves in the sample [20]. The next section briefly describes about spallation during shock loading.

2.8 Dynamic Spallation

Dynamic spallation refers to the dynamic tensile behaviour of a material under uniaxial strain conditions that result in nucleation, growth and coalescence of voids or crack formation [81]. The compressive waves generated from high velocity impact events propagate away from the impact site and tend to encounter the free surfaces. At this point, release waves are generated that communicate free surface zero stress boundary condition to the shock compressed material [82]. In a flyer plate impact test, when the flyer plate hits the target, shock waves are generated, travelling in opposite directions from the plane of impact. These compressive waves reach the free surfaces of the flyer plate and the target and reflect back as tensile release waves. The release waves interact with each other at a plane, referred to as the spall plane, generating a high magnitude tensile pulse. If the magnitude of the tensile pulse is greater than the spall strength of the material, plastic deformation occurs, thereby resulting in separation of material and spallation [83]. Spall strength is a characteristic of the tensile strength of the material and refers to the threshold required for damage or fracture initiation. The distance-time plot in figure 2.26 shows the propagation and reflection of the elastic and plastic waves as a result of flyer plate impact and the spall plane at which the release waves interact.

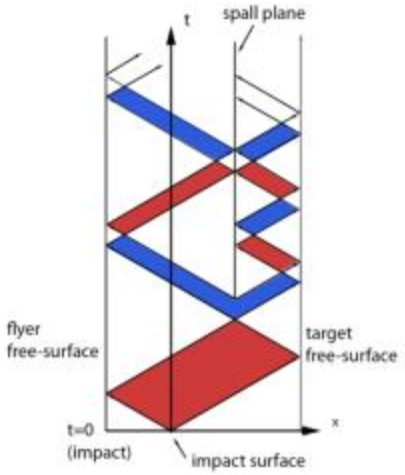

Figure 2.26: Distance-time plot from plate impact experiments showing propagation of waves and formation of spall plane [84].

The incipient spall threshold is defined as that combination of stress and time (pulse duration) below which no damage to the specimen would be visible [85]. The stresses in excess of the tensile strength of the material result in the process of internal failure or rupture of condensed media through the mechanism of cavitation [86]. Spall damage occurs within the material when the magnitude of the tensile pulse approaches or exceeds the spall strength, which is dependent on loading conditions, sample geometry and material microstructure [81]. The resistance to spall also depends on the compressive yield strength of the material. Materials with high yield strength have better resistance to nucleation of voids. Grain boundaries, grain boundary precipitates, precipitation free zones, and coarse intermetallic particles are other microstructural aspects that must be taken into account to predict the spall behaviour of metals [83], [87].

Spall damage can be studied by examining the samples recovered after a series of impact loading experiments at varied peak stress and determining the stress threshold

corresponding to the first appearance of damage [88]. The other method is based on measurements of the free surface velocity history. Tensile stress decreases rapidly to zero due to fracture of material and as a result, a release compression wave appears in stretched material adjacent to spall plane. The period of velocity oscillation of the spall pulse is a measure of the spall plane and the velocity pullback is a measure of the incipient fracture strength [88]. Various characterization techniques such as optical microscopy and scanning electron microscopy have been used to obtain images to study the fractured surface visually.

Spall can be classified into three categories based on the extent of damage [87]. Figure 2.27 shows an example of the three classifications.

- Incipient spall: nucleation of the spall.
- Intermediate spall: spall grows due to tensile stresses and depends on temperature and strain rate.
- Spall fracture: spall coalesce after sufficient growth to form fracture surfaces and the material completely fails.

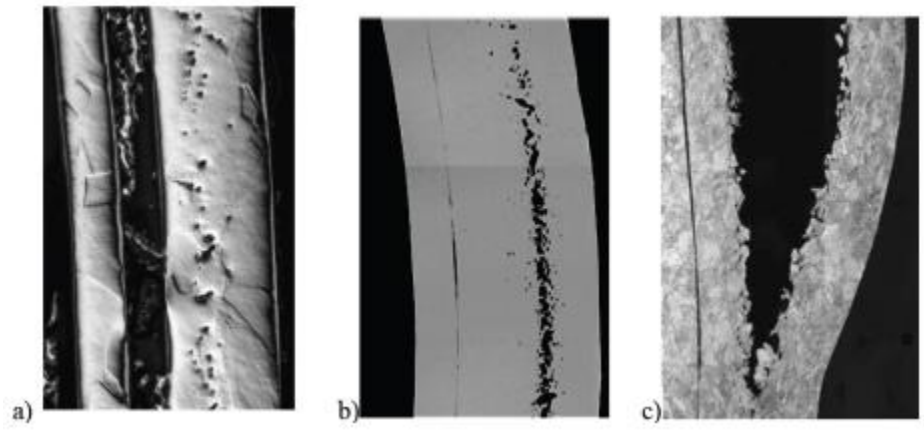

Figure 2.27: Examples of: a) Incipient spall b) Intermediate spall c) Spall fracture [89], [90], [22].

Spall damage occurs during shock loading as a result of excess tensile stresses produced by the interaction of release waves [91]. The favourable conditions for spall can be produced 1) by impacts, 2) by lasers or other thermal radiation sources, and 3) by explosions [91]. The peak free-surface velocity, u_0, and the free-surface velocity just before the arrival of the spall pulse, u_m, are determined directly from the free-surface velocity profile [91]. Within the acoustic approach, the linear approximation in equation is used:

$$\sigma^* = \frac{1}{2}\rho_0 c_0 \Delta u_{fs} \tag{2.52}$$

where, ρ_0 is the density, c_0 is the wave speed, σ^* is the value of the tensile stress or the spall strength, and $\Delta u_{fs} = u_0 - u_m$ is called the velocity pullback [91]. Equation 2.43 gives a reasonable estimate of the spall strength as long as the density and wave speed in the material are close to their original values. This condition becomes less accurate with increasing tensile stress as it is necessary to know the compressibility of the material under tension [91].

Stepanov and Romanchenko studied the effect of elastic-plastic response and spall plate thickness on the velocity pullback and obtained an expression for spall strength as in equation 2.47 [91].

$$\sigma^* = \rho_0 c_l \Delta u_{fs} \frac{1}{1+\frac{c_l}{c_b}} + \Delta\sigma \tag{2.53}$$

where, c_l and c_b are longitudinal and bulk sound velocities, and $\Delta\sigma$ is a function of the stress gradient of the refracted wave and spall plate thickness [91].

There are many factors that influence spall strength such as microstructure, yield strength, temperature, etc. and a lot of research has been done to understand the effects

of such parameters on the tensile behaviour of the material. These factors are beyond the scope of this work, so the interested reader is referred to the work of Chen et al. [81], Kanel et al. [92], [93], Peralta et al [90] for more details.

In this chapter, a brief introduction to shock, experimental methods to achieve high strain rate conditions, hydrodynamic instabilities and their application to study strength, and the phenomena of spall has been provided. In addition to this, the different regimes at high strain rates and various constitutive material models to study the behaviour of materials under dynamic conditions are also discussed. It can be seen that the use of hydrodynamic instabilities in high strain rate experiments works well for studying various aspects of the dynamic strength of a material. In this research, we will primarily focus on using the experimental configuration of Piriz et al. and Opie et al. to drive a shock wave from the rippled surface of the sample and use the experimental data to evaluate strength. In the next chapter, the key objectives of this research will be provided.

CHAPTER 3

OBJECTIVES

The dynamic strength of a material plays a major role in controlling the growth of hydrodynamic instabilities. During extreme conditions, this strength is bound to be dependent on several factors such as applied pressure, strain, strain rate, temperature, etc. There is a need for choosing and calibrating a constitutive model to describe accurately the nature of the dynamic strength and its effect on instabilities by taking the appropriate factors into consideration. In this regard, the objectives of this research work are as follows:

1. Study plasticity during shock loading by analysing dynamic data from hydrodynamic instability experiments.
    - Both rate independent and rate dependent material models along with a Mie-Grüneisen equation of state will be used to study plasticity during shock loading.
    - Rate independent models:
        i. Elastic-perfectly plastic
        ii. Steinberg-Guinan
    - Rate dependent models:
        i. Preston Tonks Wallace (PTW)
        ii. Steinberg-Lund
        iii. Implementation of these models is done using the 1D Hydrocode LAGC1D, Combined Hydro and Radiation Transport Diffusion Hydrocode (CTH), and ABAQUS™/EXPLICIT.

2. Perform a calibrtion of boundary conditions (driving pressure) for each model and then analyse the predicted response.
    - The calibration technique is done by using the best-fit technique. A laser pulse was used to shock load samples and the Velocity Interferometer System for Any Reflector (VISAR) is used to obtain the velocity data. The velocity history can be obtained from this data. In the best-fit technique, the velocity history of flat samples and selected rippled samples will be closely matched with the experimental result. A pressure boundary condition (or equivalent) will be used in this simulation. The value of the pressure for which the simulated velocity profile closely matches with the experimental velocity is the calibrated pressure for the corresponding laser energy.
    - The response of each of the models mentioned in point 1 will be analysed. The model that more closely matches the shape of the velocity profile will be calibrated and validated. While calibrating using the experimental velocity profile, the spall pullback is not taken into consideration. Calibration is done only for the region before spall pullback.
3. Calibrate and validate the developed constitutive model.
    - Calibration of the material constants and the relationship between the laser energy and applied pressure is done simultaneously using the method mentioned in point 2.
    - Validation of the model is done by comparing the experimental data from Transient Imaging Displacement Interferometry (TIDI) with the amplitude of the perturbation at the free surface obtained from

simulations. TIDI is used to measure the out-of-plane displacements at the free surface.

4. Use the calibrated model to study the effects of strength on the growth of hydrodynamic instabilities.
    - Evaluation of the free surface amplitude is monitored by varying the parameters in the model that would alter the range of the material strength, i.e., the parameters that will increase and decrease the strength.

CHAPTER 4

EXPERIMENTAL AND MODELLING PROCEDURES

4.1 Experimental Setup to Achieve High Strain Rate

The shock loading experiments for this research were performed by Loomis and P.Peralta at the Trident Laser Facility at Los Alamos National Laboratory (LANL). The experiments at Trident were carried out on samples of pure aluminium (Al) with surface perturbations that were loaded using direct laser drive. This, in turn, led to perturbations on the shock front that travelled through the sample and made an imprint on the free surface. This imprint then grew as a result of what is essentially a Richtmyer-Meshkov instability (RMI).

The strength of material can lead to significant resistance to shear deformation at large strain rates and this strength is known to decrease the growth rates of RTI and RMI [19]. Experiments using hydrodynamic instabilities can also be used to study material anisotropy in polycrystalline materials that can affect plasticity under dynamic conditions and lead to damage nucleation and growth [17].

The experiments at LANL were performed on two sets of Al samples: flat and rippled. The thickness of the flat samples ranged from 50 μm to 80 μm. The rippled samples had a perturbed surface with either a square wave or a sine wave. For the experiments in this research, the samples were imprinted with a sine wave. The process used to imprint sine wave ripples in Al samples is described in section 4.3. This process resulted in surface perturbations in the form of sine wave with wavelength of 100 μm and 150 μm on one side of the sample. The perturbations with a wavelength of 100 μm had an amplitude 2 μm and those with a wavelength of 150 μm had amplitude of 4 μm. The thickness of the rippled samples ranged from 50 μm to 100 μm.

The shock wave was produced on the sample using laser ablation process. A high intensity laser beam was used to ablate the surface of the sample, which resulted in the formation of plasma and gas. The evaporation of this layer produced an equal reaction directed in the form of shock wave into the sample [36]. The applied pressure was controlled by varying the laser intensity and the laser pulse lasted for about 5 to 7 ns.

The experimental set up from Opie et al. [19] was used wherein, a rippled shock front, created by ablating the perturbed surface of the sample was 'fed-thru' to the sample at the free surface. This is shown in figure 4.1.

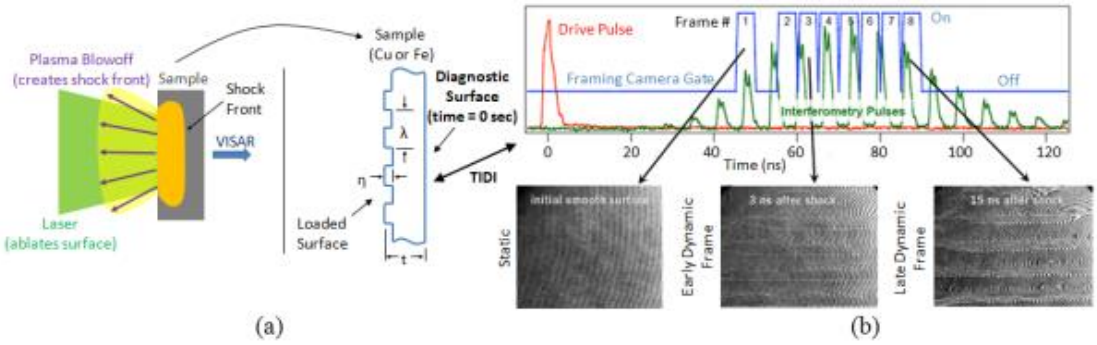

Figure 4.1: Experimental setup for shock loading of perturbed samples. a) Laser ablation and sample configuration highlighting the loaded surface and the free surface b) Laser pulse train to capture TIDI data and example images [19].

As the rippled shock front propagated through the thickness of the sample, it underwent Richtmyer-Meshkov oscillations coupled in time and space, and eventually arrived at the free surface [70]. The curvature of the shock front created velocity perturbations in the loaded sample. These velocity perturbations were modified by the strength of the sample and are coupled with the wavefront [94]. As already stated, upon arrival at the free surface, the rippled shock imprinted perturbations that grew via RM instability. The physics of rippled shock perturbation evolution and the influence that

material strength has on it can be analysed by studying the evolution of perturbations imprinted on the free surface due to the ripple shock. Figure 4.2 shows the ripple shock front originating from the ablated surface along with the imprinted perturbations on the free surface.

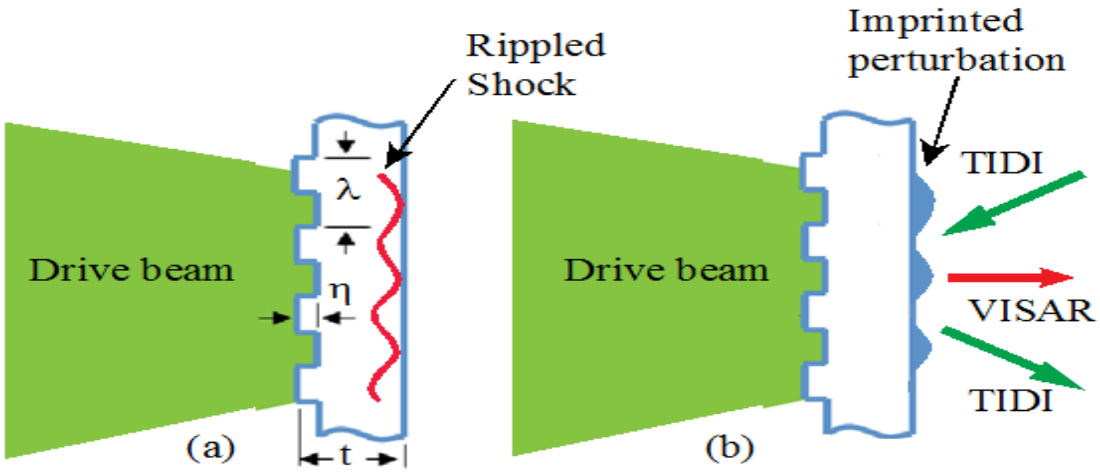

Figure 4.2: a) A rippled shock front originating from the laser ablated surface b) Perturbations imprinted by the rippled shock on the free surface that has VISAR and TIDI diagnostics.

The velocity profile at the free surface was monitored using the Line VISAR [43]. The TIDI [48] was used to record the out-of-plane displacement at the free surface with <100 nm sensitivity and <5 μm spatial resolution. Due to its high sensitivity, small amplitude changes at the free surface can be measured, which are otherwise difficult using other diagnostic techniques such as X-ray or proton radiography [17]. There were framing cameras that were used to obtain the static images of the free surface before shock break-out and two dynamic images of the free surface of each sample at two different times after the shock break-out. These images were captured using a pulse train of laser illumination.

4.2 Experimental Dynamic Data

The line VISAR output from a flat sample and a rippled sample is shown in figure 4.3. The horizontal axis is space and represents positions (x in μm) along a line on the free surface of the sample. The vertical axis is time (t in ns) and increases downwards. The VISAR output was recorded during a time window of 50 ns and the line was about 1 mm long. The time fiducials in these interferograms were obtained from pulses used for TIDI illumination and are 6.5 ns apart.

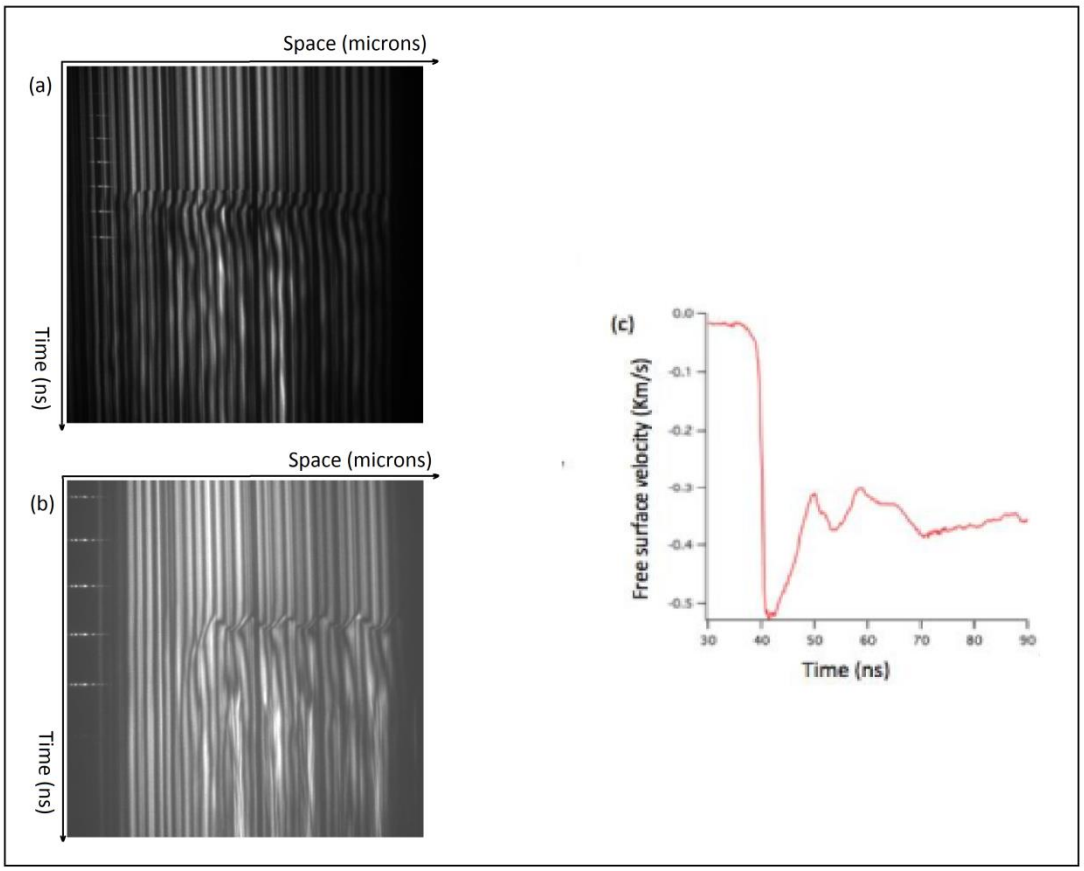

Figure 4.3: a) Line VISAR image from a flat sample b) Line VISAR image from a rippled sample c) Velocity history at the free surface after post-processing [95].

The shock break out is indicated by the start of a fringe shift, but the velocity is proportional to the amount of fringe shift as a fraction of the period of the carrier fringes. In flat samples, the fringe shift is uniform in space. In rippled samples, the line VISAR was much more heterogeneous. In particular, the locations were fringe shifts started varied both in space and time, indicating that the shock fronts did not arrive at the same time to the free surface everywhere. This can be attributed to the formation of a rippled shock front following the ablation of the perturbed surface. The time difference shown in the VISAR output of the rippled sample corresponds to the difference in time of arrival between the peak and valley of the perturbed shock front.

It was harder to obtain the velocity history of rippled samples after post-processing as the flat free surface developed peaks and valleys as the rippled shock arrived. The amplitude of the perturbations imprinted on the aluminium samples was small. Hence, the difference in arrival time between the peak and valley was not clearly seen in the VISAR output for most of the rippled samples. Image processing software, i.e., ImageJ and Data thief, were used to trace a fringe along a vertical line and estimate the velocity history based on the number of fringes shifted at a point on the line. This method was applied to flat samples and a few rippled samples with a traceable VISAR output.

On the other hand, for flat samples, the displacement of the free surface is uniform. A fast-Fourier-transform method of topography and interferometry proposed by Takeda et al. was used to process the line VISAR images to get the velocity history [96]. Using this method, an automatic discrimination is achieved between elevation and depression of the wave-front form [96]. The VISAR image is put into a computer by an image sensing device. Each row was Fourier transformed using fast-Fourier-transform algorithm for filtering out the unwanted background variation [96]. Following this, using the

algorithms of inverse Fourier transform and complex logarithm, the phase was separated from the unwanted amplitude vibration [96]. In order to correct the discontinuities due to 2π phase jumps, a criterion for the absolute phase difference was set to specify all the points with 2π phase jump [96]. The offset phase distribution of these points was added to the actual phase difference to get a continuous distribution [96]. This algorithm from [96] was used to post-process the VISAR image and obtain the experimental velocity history at the free surface.

The evolution of ripples on the free surface was studied from images recorded from TIDI at two different times and this is shown in figure 4.4. Figures 4.4 (a) and (b) shows pre and post-shot images from TIDI. Figure 4.4 (c) represents the post-processed line profiles of the TIDI output showing the out of plane displacements at two different times t1 and t2, where t2 > t1. At time t = t1, the perturbations on the free surface showed only one harmonic, whereas at time t = t2, due to the interaction between the shock front and the perturbed release waves, a second harmonic is observed as seen in figure 4.4 (c).

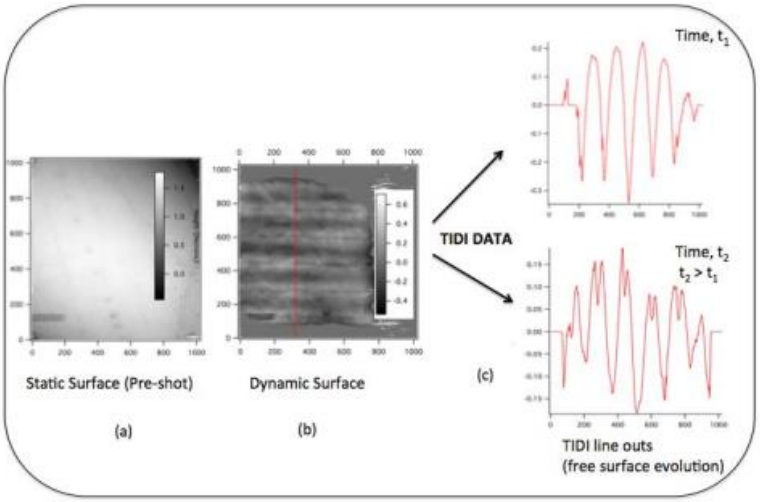

Figure 4.4: (a) Pre-shot (static) TIDI image (b) Post-shot (dynamic) TIDI image at time t (c) Out of plane displacements at the free surface after post-processing [95].

4.3 Sample Preparation

The flat samples were shaped in the form of discs and the rippled samples were square shaped. Discs with a 10 mm diameter and a thickness of about 200 μm were cut from a 99.99% pure aluminium rod. The Tech-Prep polisher available at the Multiscale Material Characterization and Multiphysics Modelling Lab (MMCMM) at Arizona State University (ASU) was used for high precision polishing of flat samples to their desired thickness. The polishing procedure is explained in section 4.4.

Diamond turning was carried out at LANL to machine sinusoidal perturbations across the face of the rippled targets. A round puck of 99.99% pure Al, was diamond turned to create a flat platform for the shock experiment with a tolerance of 2 μm. The diamond turning profiler was controlled using a custom software programming function to cut the sine wave geometry [97]. After turning, square specimens were cur from the rippled puck samples using CNC Electrical Discharge Machining at ASU Tech shop. The rippled samples were then polished down with ±10% of the desired thickness using the Tech-Prep Polisher by removing material from the side opposite to the rippled surface.

4.4 Polishing Procedure

Sample polishing was performed not only to planarize specimens to high tolerances for shock loading, but also to characterize properties of materials such as microstructure and yield strength. The samples to be polished were cut from an aluminium rod or from leftover pieces of diamond turned samples using the TechCut Precision Low-Speed Saw at the Mechanical Testing Laboratory (MTL) at ASU, shown in figure 4.5. A low concentration diamond metal bonded wafering blade, 4 inches in diameter was used for

the sectioning process. The speed of the blade at the time of cutting was set between 150 rpm and 200 rpm. Since aluminium was a light metal, extra weights were not necessary while cutting. The coolant (mostly distilled water) stored in the reservoir lubricated the contact between the blade and the sample and also reduced damage due to thermal effects. Before the cutting process, the blade was cleaned with a dressing stick attachment to remove debris or gummed materials that would hinder contact between the blade and the sample.

Figure 4.5: Precision low-speed saw [98].

Once the sample was cut, the surface to be analysed was polished using the Tech Prep Polisher at MMCMM at ASU, to give a shining surface so that it can be used in Electron Backscatter Diffraction (EBSD). The Tech Prep enables precise semiautomatic grinding and polishing of a wide variety of materials and can be used for parallel polishing, precise angle polishing, site-specific polishing or any combination of the above. Figure 4.6 shows the high precision polisher used at ASU.

Figure 4.6: Tech Prep High Precision Polisher.

The greatest advantage of Tech Prep is that it eliminates the tedious function of holding polishing jigs by hand. The sample can be swept across the polishing platen using its entire 4-inch radius as well as continuously rotated 360 degrees or within a limited range at variable speeds. A digital dial indicator is attached and can be used to measure the amount of material being removed from the sample in 1-micron increments. To flatten the surface of the sample, the platen and the vertical spindle were calibrated to ensure that they were parallel. The sample was mounted on a puck using a crystal bond. Table 4.1 lists the polishing procedure involving grinding and final polishing.

Table 4.1: General sample polishing procedure for Aluminium

Step	Abrasive	Polishing Pad	Load (g)	RPM	Time (min)
Grinding	600 grit SiC	Wet SiC paper	75-100	45	3
Grinding	800 grit SiC	Wet SiC paper	75-100	45	5-10
Grinding	1200 grit SiC	Wet SiC paper	75-100	45	12-20
Polishing	3 μm diamond suspension	Imperial Adhesive Back Polishing cloth	100	45-50	30-45
Polishing	1 μm diamond suspension	Imperial Adhesive Back Polishing cloth	100	45-50	30-45
Polishing	SIMAT 2 colloidal silica suspension	Final A Adhesive Back Polishing Pad	100	45-50	45-60

The polishing using diamond suspension removed the scratches from the surface produced from grinding. During this step, the surface of the sample was frequently observed under the microscope to check if scratches from the previous step were removed. No coolant was used in this step. SIMAT 2 colloidal silica was used as the final step to perform chemo-mechanical polishing and obtain the surface finish required to perform EBSD. Each time the sample was checked and mounted again, the surface of the pad was cleaned thoroughly with water and a new solution of colloidal silica was used on it. This was done to prevent the used solution from scratching the surface.

Once the final polishing was complete, the sample was carefully removed from the crystal bond using a solution of acetone. Once separated from the crystal bond, to remove dirt and remains of colloidal silica from the surface, the sample was dipped in a new solution of acetone followed by dipping it in a solution of ethanol or methanol. As a final step, it was cleaned in a solution of isopropanol. It was essential to avoid any

contact with the surface during cleaning. The whole process was done by dipping the sample in the respective solution.

4.5 Yield Strength and Microstructure Characterization

The yield strength and grain size were the two important characteristics that were obtained after polishing. Regarding yield strength, Giannakopolous et al. used a method to determine it from Vickers indentation [99]. In this method, the radius of the pile-up zone around a Vickers indent was measured and used to calculate yield strength [99].

The Vickers indentation testing was performed using a Leco M-400-H2 micro-indentation hardness tester at MMCMM at ASU, which is equipped with a diamond indentor in the form of a pyramid with four sides. The indentor was pushed into the material under a load of 100 g for 10 seconds. This left an indent on the surface of the material that is surrounded by a region in which the originally flat surface moves vertically. When the surface rises, this is called “pile-up”, and when the surface goes down, this is called “sink-in” [99]. This represents the total area of plastic deformation due to indentation or “plastic-zone”. The radius of the plastic zone was measured using optical profilometry at the LeRoy Eyring Center for Solid State Science, ASU. The yield strength was calculated according to equation 4.1, established by Giannakopolous [99].

$$C^2 = \frac{0.3P}{\sigma_y} \tag{4.1}$$

In the above equation, P represents the indentation load, C is the radius of the plastic zone and σ_y is the yield strength [99].

Regarding microstructure, Scanning Electron Microscopy (SEM) was used to study the microstructure of the material. The Electron Backscatter Diffraction (EBSD) technique was used to map the microstructure and determine the grain size. It was essential to polish the sample to get a damage free surface in order to scan it with SEM. The Orientation Imaging Microscopy (OIM) technique utilizes EBSD patterns produced during SEM and create a grain orientation map of a sample surface [100], [101]. The sample was mounted on a holder that was then fixed onto SEM stage. The stage was rotated 70° from the horizontal, so that it was highly tilted towards the EBSD detector as shown in figure 4.7. The EBSD detector is comprised of a CCD camera behind a phosphorous screen, oriented at 90° from the electron beam pole piece [101], [102].

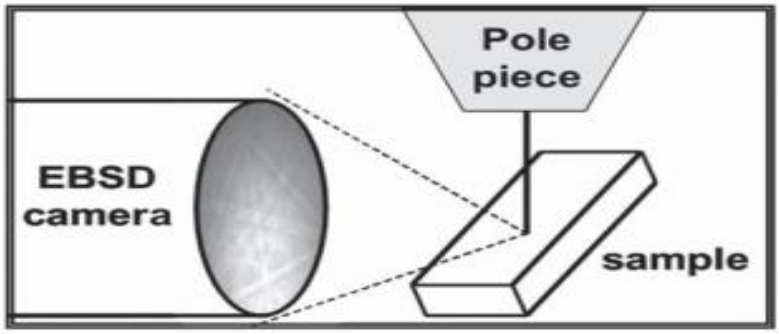

Figure 4.7: Position of the sample inside the SEM chamber relative to the EBSD detector and pole piece [103].

Raster of the electron beam combined with automated indexing of the EBSD patterns allowed to map the microstructure of the sample based on the crystallography of individual points. The results were post-processed using EDAX-TSL OIM™ analysis software to obtain maps of the microstructure and grain size.

4.6 Numerical Simulations

Numerical simulations of the experiments to relate material strength to rippled shock propagation and evolution of instabilities at the free surface produced by the rippled shocks were performed using Lagrangian and Eulerian approaches. Lagrangian simulations were carried out using the finite element and finite difference methods and involved 1D and 2D simulations of polycrystalline aluminium samples using various strength models and a pressure boundary condition was used to simulate the laser pulse used in the experiment to ablate the surface of the sample.

One dimensional finite difference simulations were performed using a 1D Lagrangian Hydrocode (LAGC1D). The simulations were carried out using elastic-perfectly plastic model for material strength. The LAGC1D is a suite of programs to calculate the dynamic response of materials to impact or dynamic loading in 1D [104]. The programs define the initial position, velocity and state of each region, integrate the continuum equations in time and re-zone the mesh [104]. The ARIADNE material model library from [104] specifies the parameters required for various models that are used along with the equation of state. The material and geometrical data are kept in separate files from the control data and are copied into the appropriate place as a program is run.

Lagrangian simulations were also performed with the finite element code ABAQUS™ using time integration [105], [106]. Simulations were done by using the elastic-perfectly plastic model coupled with Mie-Grüneisen equation of state (MG-EOS) already available in ABAQUS™ as well as the PTW strength model coupled with MG-EOS implemented using a fortran subroutine within the ABAQUS™ built-in co-rotational framework [105], [106]. Figure 4.8 shows the geometry of the rippled sample to be modelled and figure 4.9 shows the geometry used in ABAQUS™ along with the boundary conditions applied.

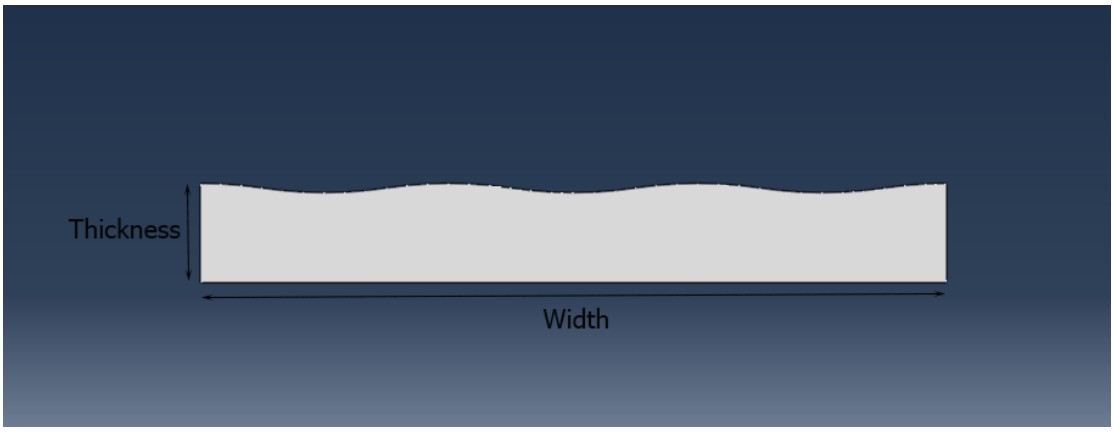

Figure 4.8: Rippled sample geometry.

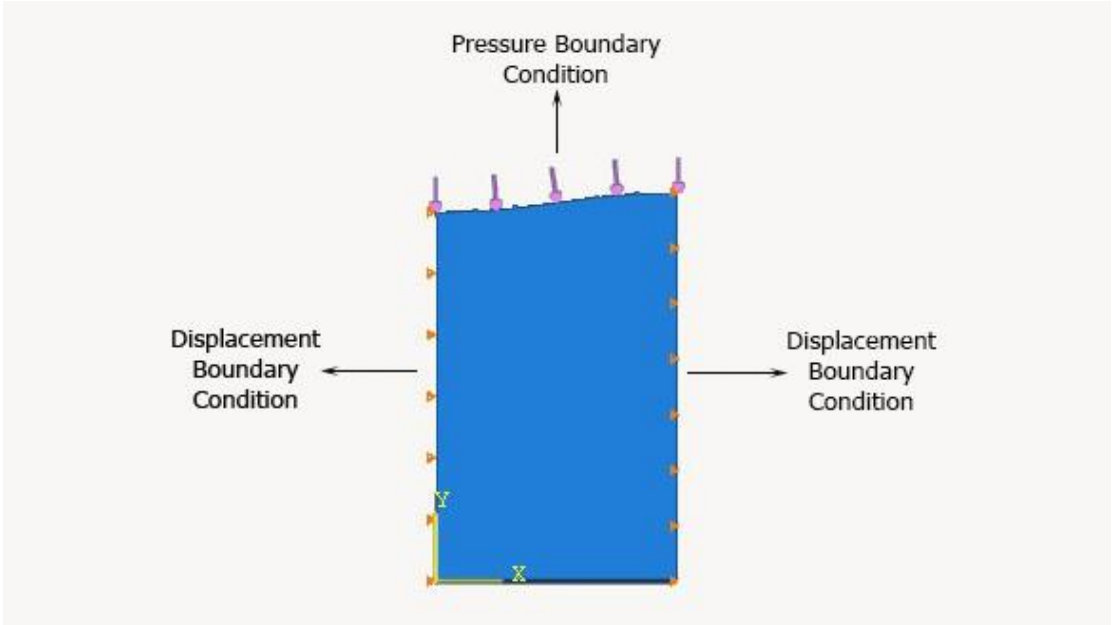

Figure 4.9: Sample geometry in ABQAUS™ with the applied boundary conditions.

The optimal element size for the finite element analysis was obtained by performing a mesh-convergence study. The geometry considered was similar to the one shown in figure 4.9. The simulation was run for a total of 40 ns. In this research, the displacement at the free surface before tensile wave breakout from was used as a parameter to quantify strength. Hence, the displacement at approximately 20 to 22 ns, which is almost 8 to 9

ns after shock break out, was used to study the convergence of the solution with different mesh sizes. The element sizes ranged from 2.0 to 0.4 μm. The mesh convergence of the displacement at the free surface is shown in figure 4.10.

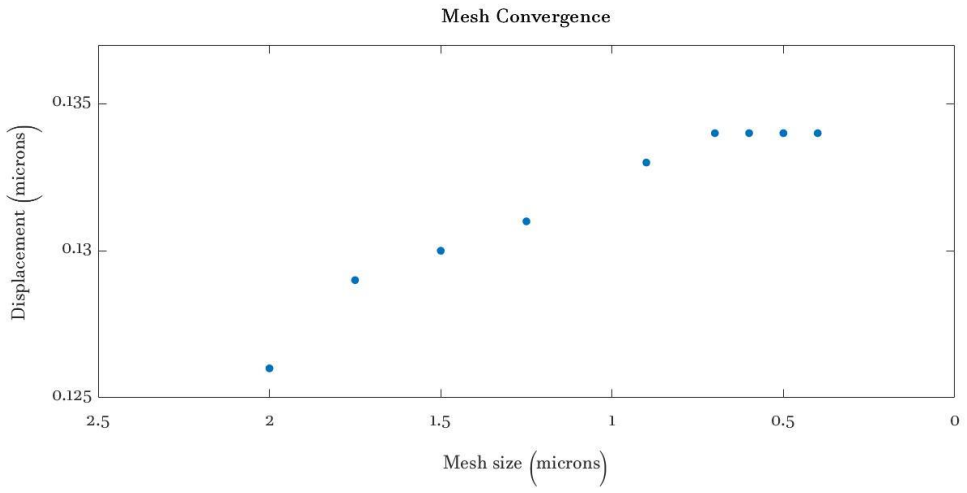

Figure 4.10: Convergence of displacement for different element sizes.

As seen in figure 4.10, the displacement starts converging for a base element size of 0.7 μm and is almost constant after that. An element size of 0.7 μm was chosen to be the optimal mesh size.

Simulations in ABAQUS™ were used to test the boundary conditions obtained from the 1D hydrocode. This was done by comparing the velocity histories from the experiments with the simulation. Following this, the displacement at the free surface was estimated at the desired times to be compared with the experimental data in order to study the dynamic yield strength of the material.

The stable time increment size, which is defined as the smallest transit time of a dilatational wave across any of the elements in the mesh, was automatically calculated for each solution by ABAQUS™ explicit solver using equation 4.2 [105], [106].

$$\Delta t \approx \frac{L_{min}}{c_d} \tag{4.2}$$

In the above equation, L_{min} is the smallest element size in the mesh, and c_d is the dilatational wave speed, which is determined by ABAQUS™ explicit by calculating the effective hypoelastic moduli from the constitutive response of the material [105], [106]. This value of time step will be less than equation 4.2 by a factor between $1/\sqrt{2}$ and 1 in a two-dimensional model [105], [106].

Regarding Eulerian simulations, the Combined Hydro and Radiation Transport Diffusion (CTH) hydrocode [107] was used for simulating the process of shock loading in both flat and rippled samples and obtain histories of velocities, displacements and stresses at desired locations. CTH is a multi-material, Eulerian, large deformation, strong shock wave, solid mechanics code developed at Sandia National Laboratories [107]. A two-step, second-order accurate Eulerian solution algorithm is used to solve the mass, momentum and energy conservation equations [108]. CTH includes rate dependent models of material strength and these models rely on the use of internal state variables (equivalent plastic strain) to account for the history dependence of material response [108]. It has adaptive mesh refinement and uses second-order accurate numerical methods to reduce dispersion and dissipation and produce accurate, efficient results [107]. The CTH simulations were run by Dr. Pedro Peralta at ASU using the elastic-perfectly plastic and Steinberg-Lund models.

Figure 4.10 shows the geometry of the rippled samples used in the CTH simulations along with the applied boundary conditions. To analyse the velocity and displacement history at the free surface, a rippled flyer plate with the same amplitude and wavelength as the ripples on the samples was used to replicate the shock produced by the laser. This is also indicated in figure 4.11 to control the nature of the release waves from the flyer, a

density gradient is applied on the flyer close to its free surface. This is done to mimic the gentler release observed from the velocimetry of the lase shots resulting from expansion of gases. The thickness of the flyer was meant to mimic the duration of the pulse measured with velocimetry diagnostics. The dots in the figure represents tracers (Lagrangian particles) at which time history of various parameters were recorded.

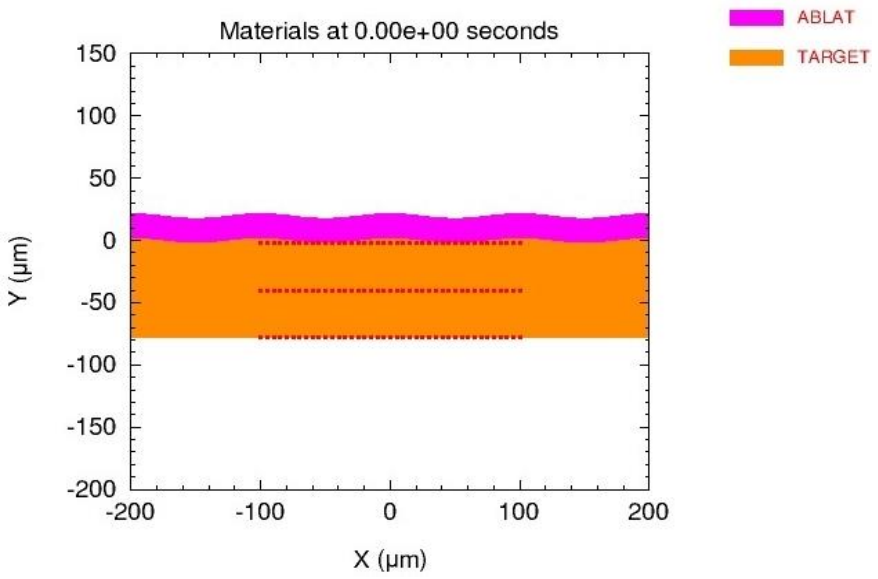

Figure 4.11: Geometry of the sample showing the shock loaded surface and the flyer plate of definite thickness.

The plot in figure 4.11 was created from a simulation that only modelled the region $x \geq 0$. However, a symmetry plane was assumed at $x = 0$.

Flyer is made of Al and its thickness is about 24 μm, which results in an approximate pulse duration of 7 ns under the shock conditions observed during the experiments. Flyer velocities are chosen to obtain good agreement with peak velocities measured by line-VISAR on the free surface. The mesh along the y-direction was uniform with a cell size of 0.33 μm, which was found to be fine enough to resolve the shock front through a

convergence analysis. The mesh in the x-direction was finer close to the center, with a cell size of 2 μm between 0 and 1 mm, and 10 μm from 1 to 2.5 mm. The computational domain was 0 to 2.5 mm in x and -200 to 200 μm in y, which was large enough to contain the sample for the 50 ns duration of the simulation, which was also long enough to match the timing of the TIDI data acquisition.

Boundary conditions for the computational domain were essentially, free tractions for the top and the bottom and symmetry boundary conditions for the left and the right. This allowed to simulate both small and larger Al samples used in this work.

CHAPTER 5

EXPERIMENTAL RESULTS AND DISCUSSION

In the first two sections of this chapter, the determination of static yield strength from indentation test and the microstructural characterization will be covered. The rest of the chapter will discuss the dynamic data of the high-pure aluminium samples obtained from line VISAR and TIDI.

5.1 Yield Strength from Indentation

The static yield strength of aluminium is an important parameter that was measured from indentation tests. Several indents were made on the sample under a load of 100 g and the average radius of the pile-up zone was measured using a Zygo ZeScope optical profilometer. Figure 5.1 shows the images of the pile up zone of one of the indents, obtained from the optical profilometer.

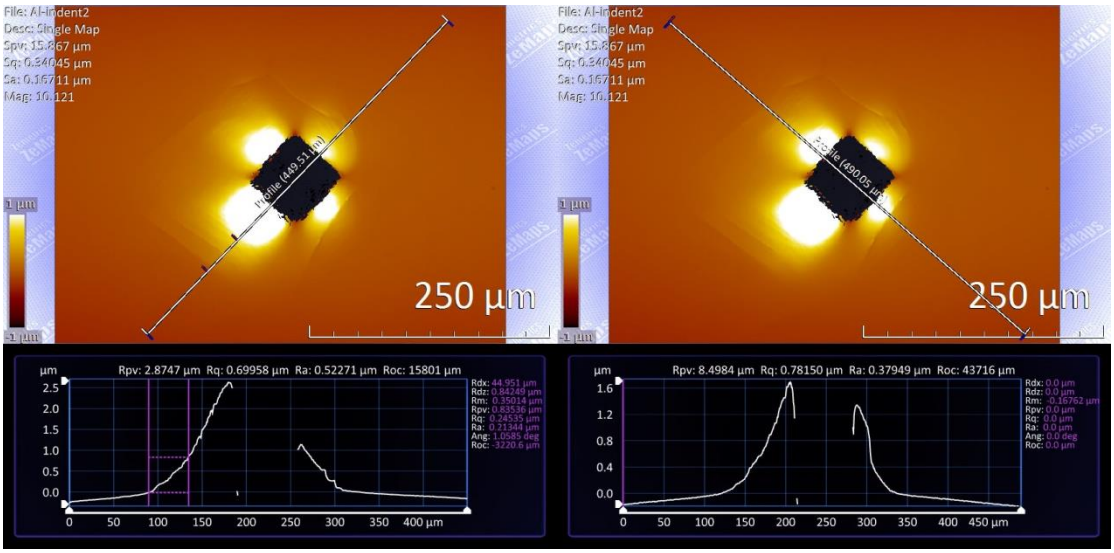

(a) (b)

Figure 5.1: Topography of the pile-up zone surrounding Vickers indents in Al from optical profilometer.

The yield strength was calculated using equation 4.1 from [99]. Table 5.1 shows the calculated values of yield strength from five different indents made on the sample.

Table 5.1: Calculated values of yield strength from indentation test

Indent No.	D1 (mm)	D2 (mm)	Average D (mm)	Average R (mm)	Yield Strength (MPa)
1	0.27	0.25	0.26	0.13	18.48
2	0.29	0.27	0.28	0.14	15.93
3	0.28	0.31	0.295	0.1475	14.35
4	0.24	0.28	0.26	0.13	18.48
5	0.3	0.29	0.295	0.1475	14.35
Average Yield Strength					16.32

The yield strength of the material is an important property in high pressure shock loading applications [24]. As already discussed in chapter 2, when a material is shock loaded, high pressure compressive waves propagate through the material, which lead to

high strain rates. This eventually causes an increase in the flow stress of the material. Hence, the average value of the yield strength measured in this experiment was used as a rough lower bound, which indicates the stresses above which the material might start yielding.

5.2 Determination of Grain Size

After polishing the sample using the procedure described in section 4.4, microstructural characterization was performed in order to determine the grain size. Scanning electron microscope was extensively used for this purpose. As stated in section 4.5, orientation image mapping was used to measure the average grain size by utilizing the EBSD patterns produced by SEM. The inverse pole figure map of aluminium was obtained for an area of 3.6 mm by 1.2 mm on the freshly polished sample and is shown in figure 5.2 a. The different colours of each grain represent the distinct grain orientations with respect to the reference direction, which is typically the out-of-plane axis [101]. This is also the direction of shock wave propagation through the sample. The inverse pole figure (IPF) legend is shown to the right of the figure. The grain size distribution for high pure aluminium as a function of area fraction is shown in figure 5.2 b. The area average for the grain size was 220.47 μm with a standard deviation of 126.33 μm.

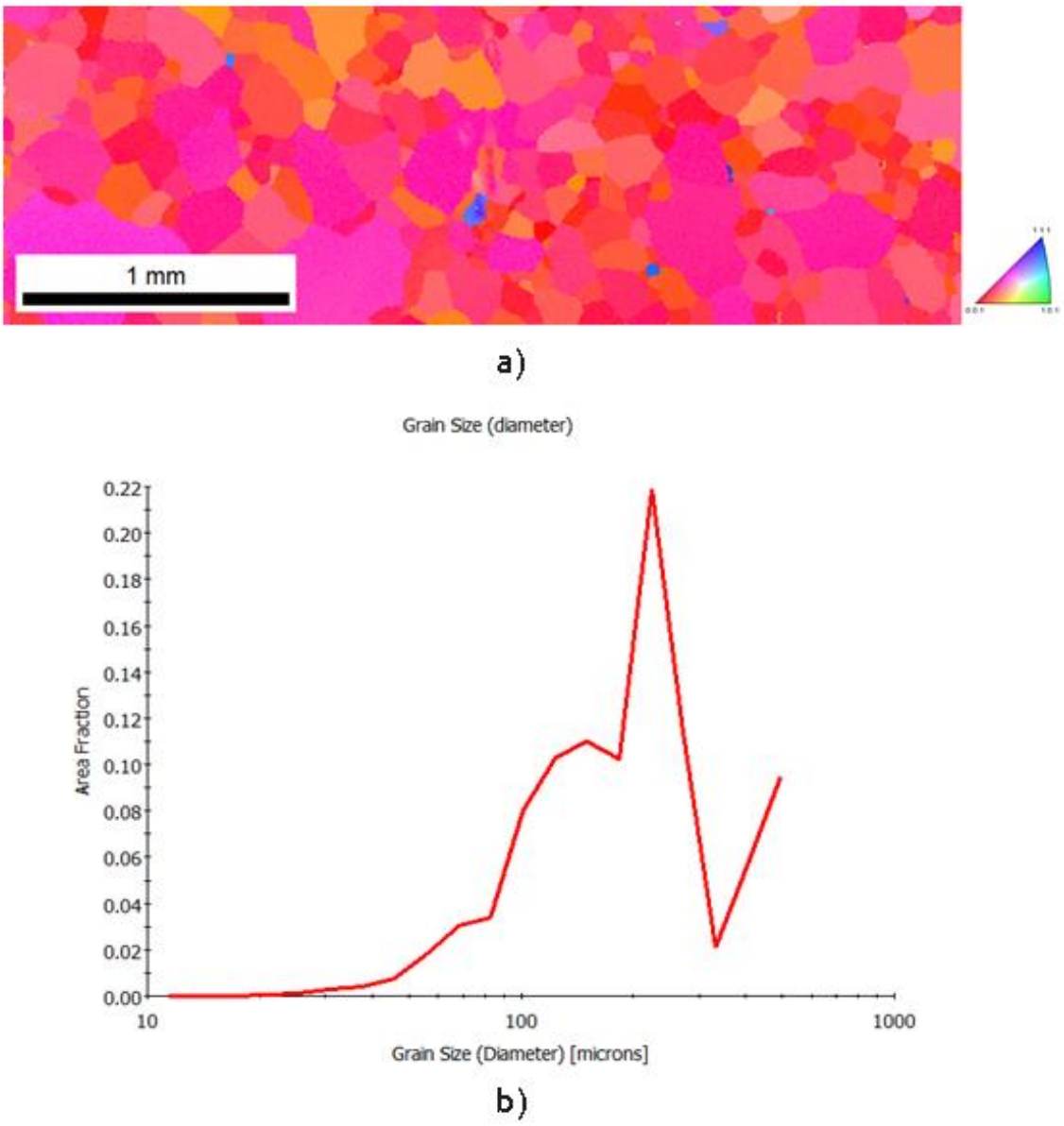

Figure 5.2: a) Inverse pole figure map; b) Grain size distribution of high purity aluminum.

As mentioned in section 4.4, a crystal bond was used to hold the sample tight while polishing. The puck is heated to about 400 K to melt the crystal bond and then the sample is placed over it, so they get bonded tight after cooling. The melting point of aluminium is close to 933 K. When it is exposed to temperature close to half its melting

point, there are more chances for the grains to increase in size. Hence, it is likely that the grain size measured is slightly higher than its actual value.

The microstructure characterization can be used to study the effect of material anisotropy and heterogeneity on local plastic response in polycrystalline materials, especially in the low pressure shock regime [17]. The grain size can also be compared with length scales used during the test.

The main concern in this study is the use of hydrodynamic instabilities to quantify the dynamic strength by the validation of rate independent and rate dependent strength models from the experimental data collected, which will be discussed in the further sections.

5.3 Velocity History of Flat Samples

The velocity history at the free surface of the flat samples was obtained by post-processing the line VISAR images of those samples. The flat samples were shocked using laser ablation and the laser pulse lasted for approximately 5-6 ns as shown in figure 5.3.

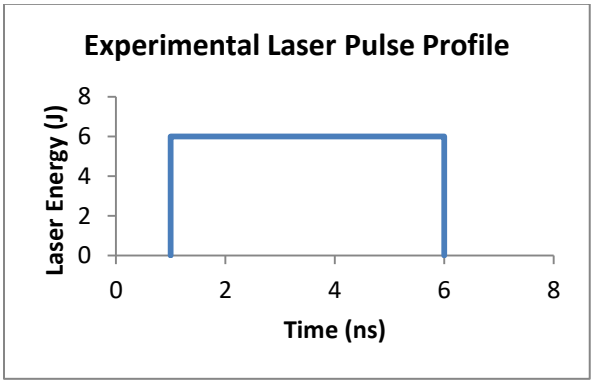

Figure 5.3: Experimental laser pulse profile to shock the samples.

Table 5.2 contains the details of the geometry and the laser pulse conditions at which the flat samples were shocked.

Table 5.2: Data for flat samples

Shot #	Thickness (μm)	Laser Energy (J)	Pulse Duration (ns)
25304	64	9.1	5
25305	73	13	5
25306	56	11.2	5

The post-processing was done by taking the average from two methods:

- Fast Fourier transform method proposed by Takeda et al. [96], and
- Tracing of individual fringes using ImageJ and Data thief.

As already discussed in section 4.2, Takeda's algorithm is based on the use of Fourier transform to filter the unwanted noise and the mean component of the data to obtain the phase as a function of time, which is directly related to the velocity history. On the other hand, using ImageJ and data thief, the path of the fringes that were traceable were followed and data points collected along that path. The position of these data points were converted to times and phase shifts, which then allowed obtaining velocity as a function of time. This, in turn was compared with the output from Takeda's algorithm. The final output was obtained by taking the average between these two methods. The raw and processed velocity data for all the three samples are shown in figures 5.4, 5.5, and 5.6. In the line VISAR image, the vertical axis is time and the horizontal axis represents position, with data collected in a line of about 1 mm long. The time fiducials are 6.5 ns apart, i.e., the fiducials show data that is recorded every 6.5 ns.

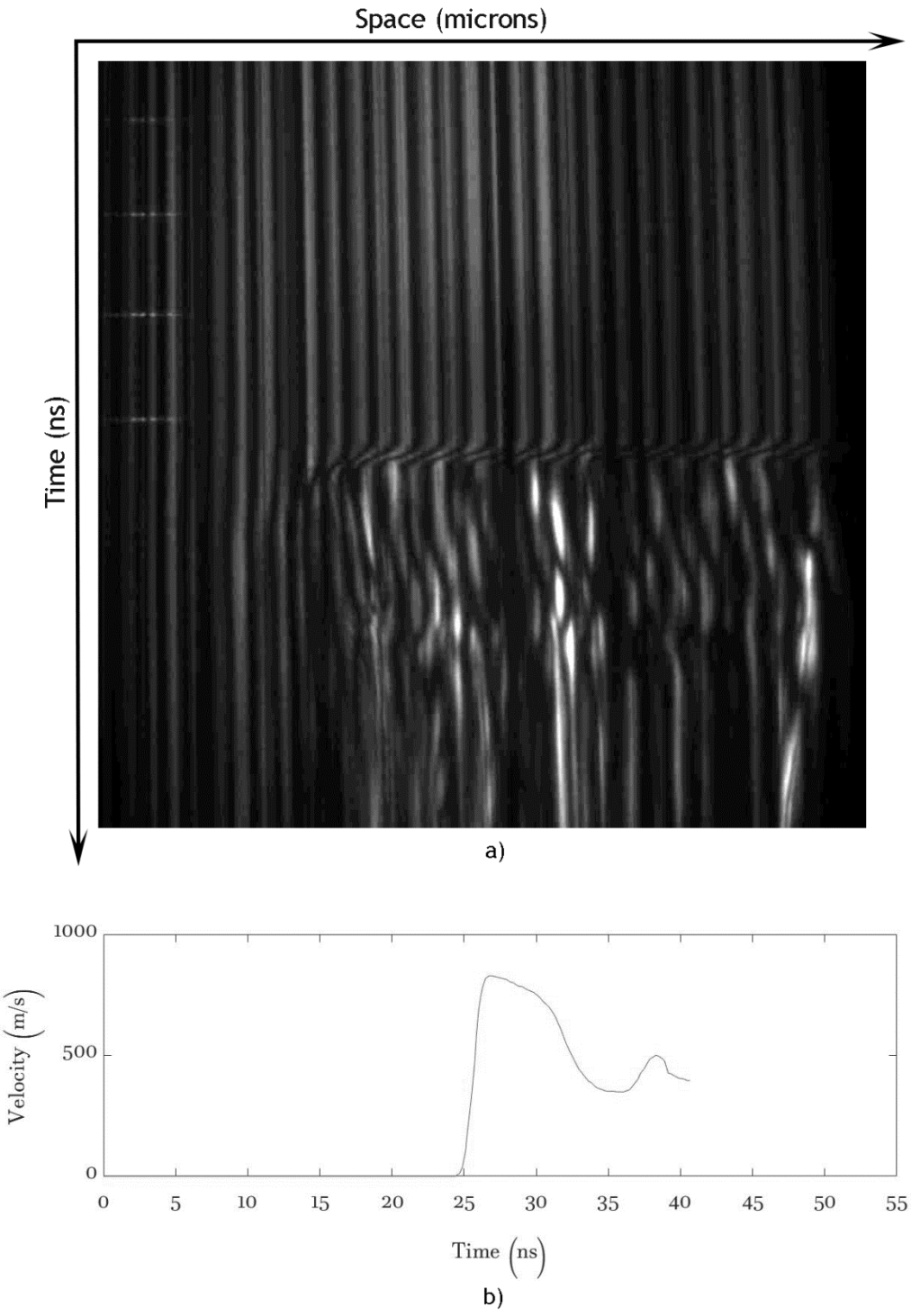

Figure 5.4: Velocity data for s25304 a) Output from the line VISAR b) Velocity history at the free surface obtained after post-processing.

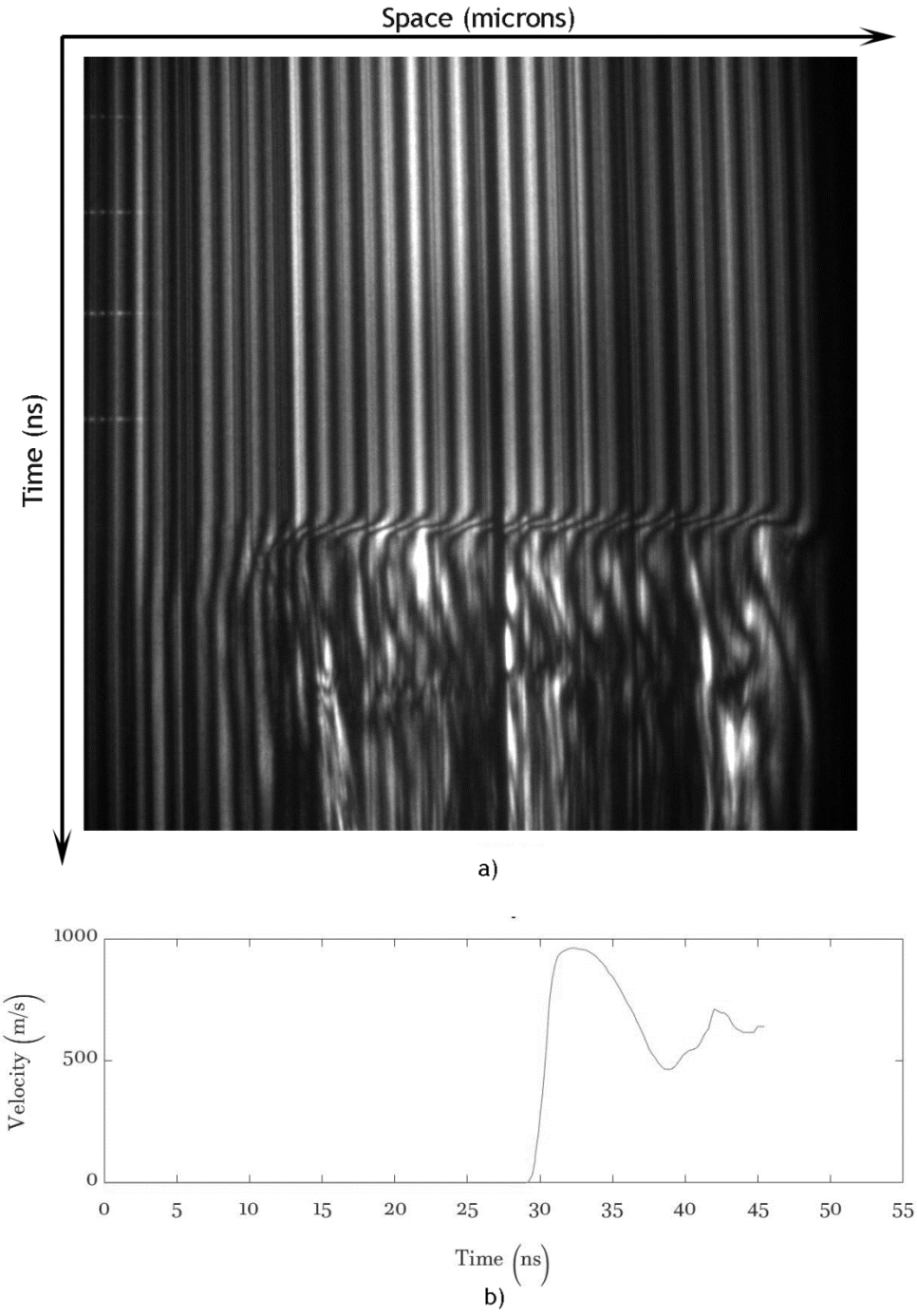

Figure 5.5: Velocity data for s25305 a) Output from the line VISAR b) Velocity history at the free surface obtained after post-processing.

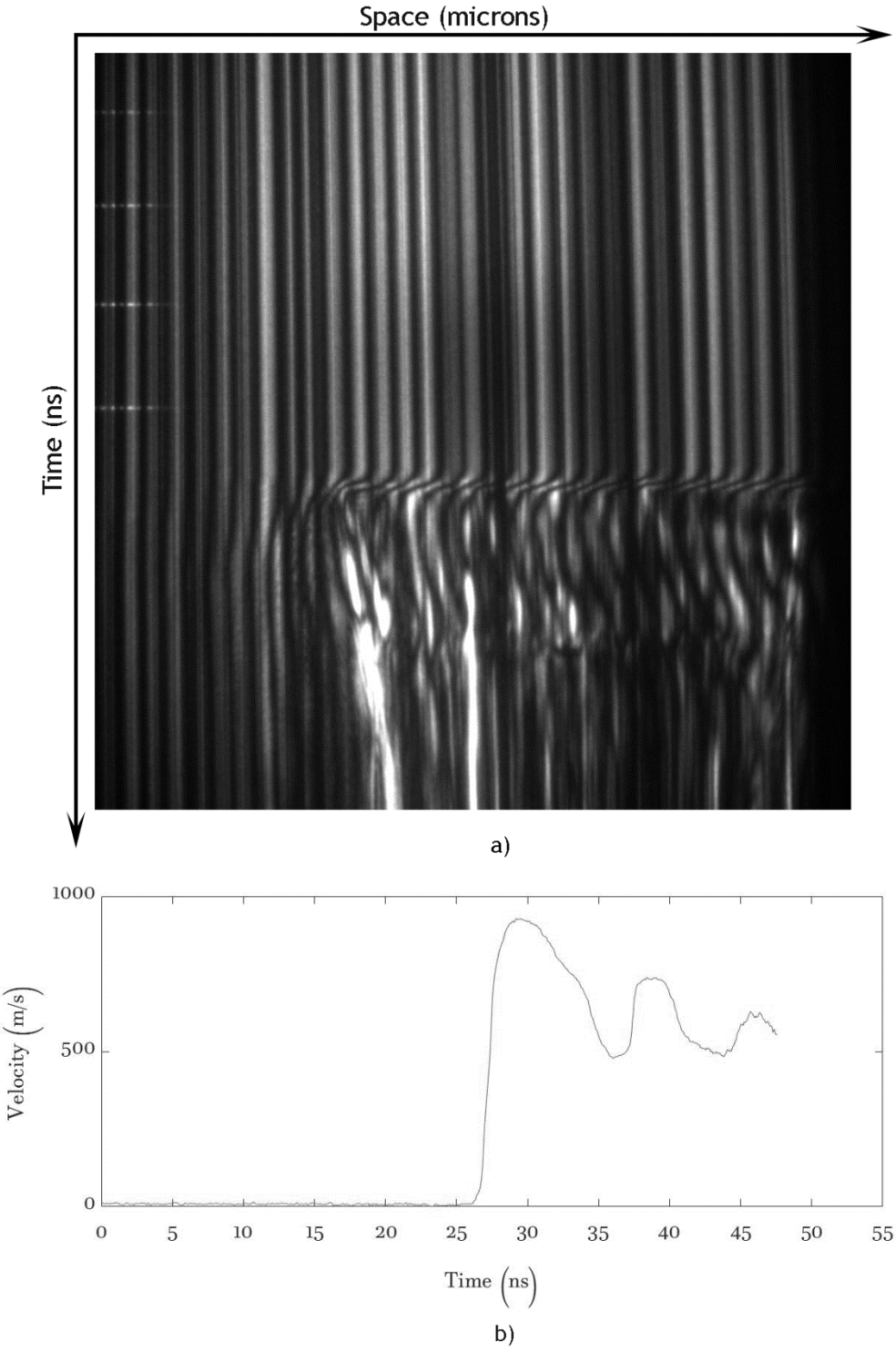

Figure 5.6: Velocity data for s25306 a) Output from the line VISAR b) Velocity history at the free surface obtained after post-processing.

In order to replicate the shock loading phenomena using laser ablation, a pressure boundary condition was used in the simulations. It was essential to estimate the applied pressure that is approximately equivalent to the laser energy. One of the main uses of the velocity history of flat samples is the calibration of the applied pressure as a function of laser energy. This is done by matching the experimental velocity with simulation predictions obtained using a 1D hydrocode or ABAQUS™ with an appropriate equation of state and an elastic-perfectly plastic model. A trapezoidal boundary condition using an applied pressure is the one that would more closely replicate the shock loading of the sample by laser ablation [95]. As indicated in table 5.2, the laser pulse lasted 5 ns, i.e., the laser hit the sample, was held for 5 ns and then removed. However, the plasma produced was still expanding after the laser is turned off, which would make the pulse last slightly more than 5 ns. Hence, in the pressure boundary condition used to replicate this, the pulse width was also varied along with the pressure, in order to match the experimental velocity history. The boundary condition in the simulations using applied pressure can replicate the velocity histories measured in the experiment. A typical pressure history is shown in figure 5.7.

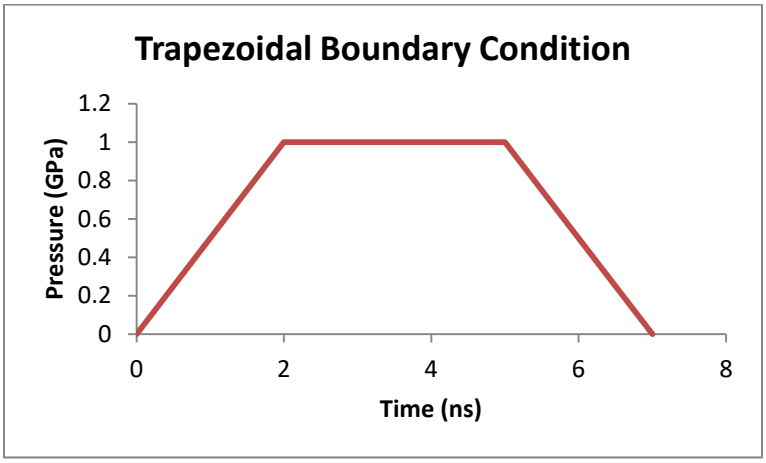

Figure 5.7: Trapezoidal boundary condition that replicates the laser ablation experiment.

This peak pressure and the total pulse duration are varied to match the experimental velocity data. However, in some cases, using this trapezoidal boundary condition in simulations implemented with rate independent models would give a square pulse that would make it difficult to match the experimental velocity. In that case, the pressure profile is given a smooth ramp while increasing it to a peak value and decreasing it to zero. The peak pressure for which the measured and predicted peak particle velocities match is considered as the applied pressure for the corresponding laser energy. Figure 5.8 shows a pressure profile provided with smooth ramps during the rise and release.

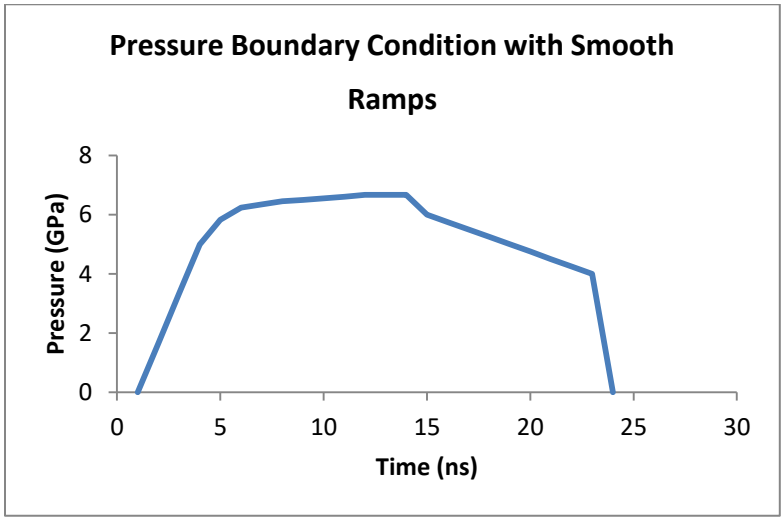

Figure 5.8: Pressure boundary condition with smooth ramps during the rise and release.

The experimental strain rates during the rise and release was calculated from equation 5.1.

$$\dot{\varepsilon}_p = \frac{1}{2C_0}\frac{\Delta U_p}{\Delta t} \tag{5.1}$$

where, the slope $\frac{\Delta U_p}{\Delta t}$ is determined from the velocity history of the sample under consideration. The free surface velocity is the sum of that due to the shock and the one

due to reflection wave and these two are approximately equal [109]. This equality is known as free-surface approximation. As a result of this, the free surface velocity is taken as twice the particle velocity. Hence, in equation 5.1, to obtain the change in particle the free surface velocity is divided by 2. The summary of the pressure, peak velocity and strain rate for each sample is given in table 5.3.

Table 5.3: Summary of measured quantities for flat samples

Shot #	Laser Energy (J)	Peak Velocity (m/s)	Applied Pressure (GPa)	Strain Rate (s^{-1})	
				Rise	Release
25304	9.1	829	6.67	5.34e7	1.17e7
25305	13	962	7.84	5.84e7	1.05e7
25306	11.2	961	7.73	5.41e7	1e7

The calibrated pressure obtained for each sample from this simulation is the pressure for the corresponding laser energy. The pressure increased with increased in laser energy. The relationship between pressure and particle velocity is given by equation 5.2 [21].

$$\sigma = \rho U_s U_p \tag{5.2}$$

where, U_s is the shock velocity and U_p is the particle velocity. From this equation, it can be seen that the particle velocity increases with increasing pressure. This can be seen in table 5.3, where the peak velocity is high for an increased pressure.

The boundary conditions show that the applied pressure increases during the rise and decreases during the release. The strain rate also follows the same trend, as it increases with increasing pressure. The strain rate during the release is much lower than the strain rate after the peak was attained.

The pressure values from table 5.3, when plotted as a function of laser energy can be used to obtain an approximate value of the applied pressure for rippled samples. However, in this work, the method of tracing has also been applied to rippled samples to post-process the line VISAR image and hence, this velocity data was used to calculate the applied pressure using the same procedure used for flat samples. In the following section, the experimental data from rippled samples will be covered.

5.4 Dynamic Data of Rippled Samples

The rippled samples were fabricated with a sine wave perturbation on the side that was shocked and the other side of the sample was made flat. The dynamic data included the velocity and displacement at the free surface of the sample, measured using the VISAR and TIDI. The experimental data of two samples was analysed and used to study the dynamic strength of aluminium. The details of the rippled samples are given in table 5.4. The experimental condition is the same as shown in figure 5.3.

Table 5.4: Experimental data for rippled samples

Shot #	Thickness (µm)	Laser Energy (J)	Pulse Duration (ns)	Amplitude of ripples (µm)	Wavelength of ripples (µm)
25274	85	8.9	5	4	150
25278	80	7.4	5	2	100

The line VISAR image of the rippled samples was post-processed using ImageJ and Data thief. Similar to the procedure followed for flat samples, the path of the fringes that were good enough to be followed were traced with data points using data thief and the average velocity history of the free surface was obtained. The output from the line VISAR

and the velocity history of the rippled samples after post-processing is shown in figures 5.9 and 5.10.

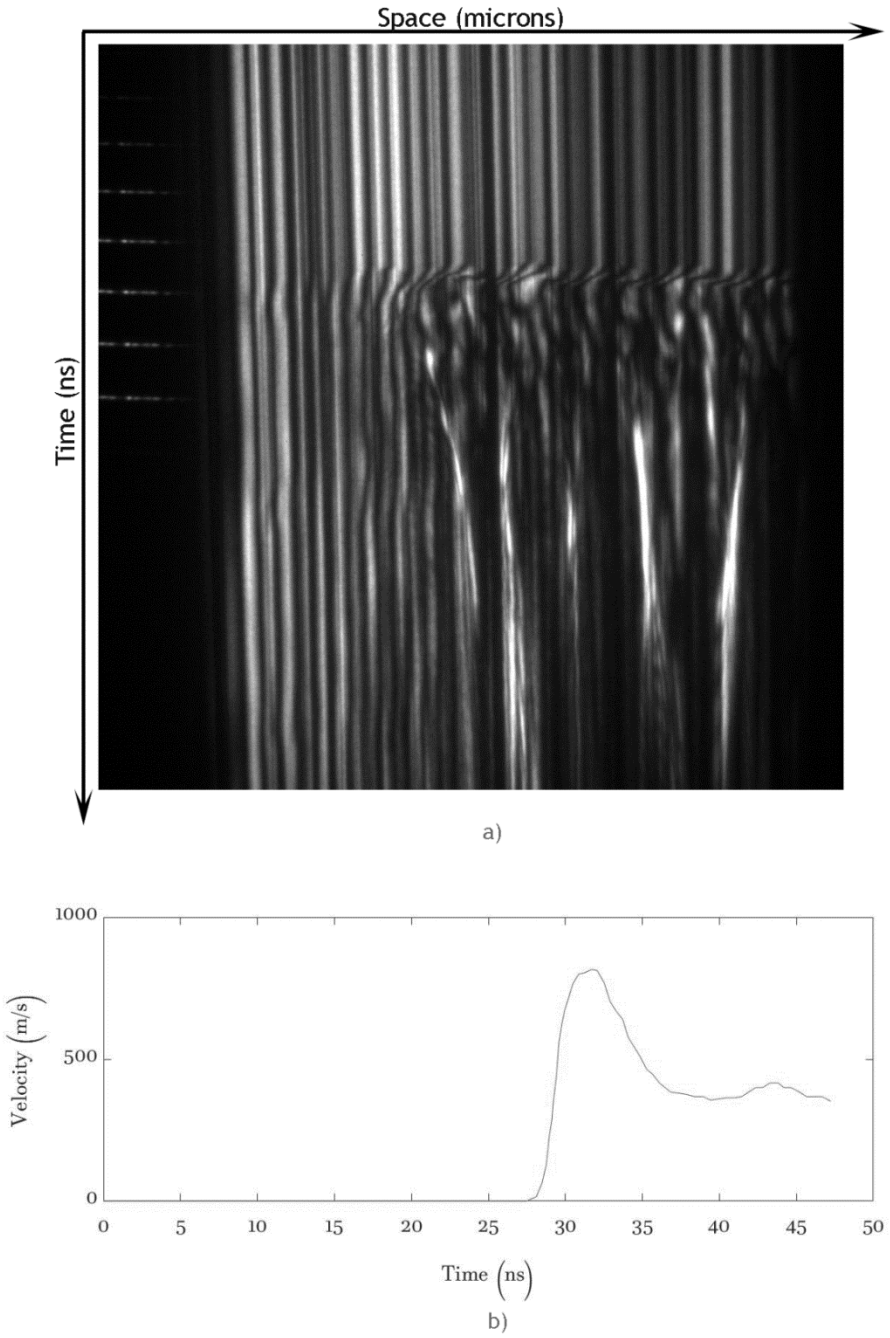

Figure 5.9: Velocity data for s25274 a) Output from the line VISAR b) Velocity history at the free surface obtained after post-processing.

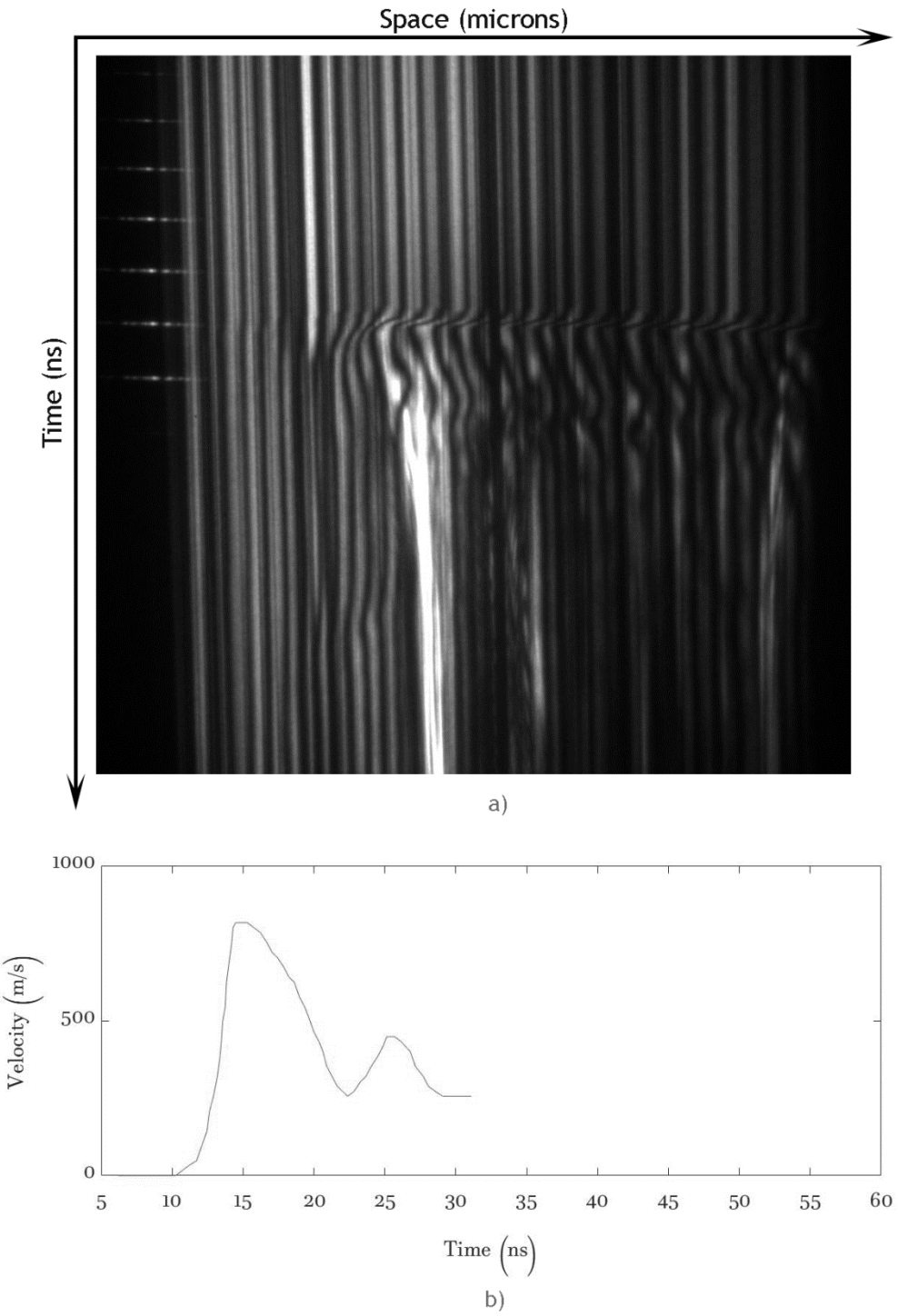

Figure 5.10: Velocity data for s25278 a) Output from the line VISAR b) Velocity history at the free surface obtained after post-processing.

Similar to the flat samples, the calibration of the applied pressure was done using a 1D hydrocode by implementing an elastic-perfectly plastic model. The experimental strain rates during the rise and release was also calculated using equation 5.1. Table 5.5 gives the summary of the measured quantities from the experimental data.

Table 5.5: Summary of measured quantities for rippled samples

Shot #	Laser Energy (J)	Peak Velocity (m/s)	Applied Pressure (GPa)	Strain Rate (s^{-1})	
				Rise	Release
25274	8.9	816	6.8	4.52e7	1.03e7
25278	7.4	808	6.66	3.37e7	0.84e7

Similar to the flat samples, a correlation can be seen between the applied pressure, peak velocity and strain rates during the rise and release.

The images from TIDI were post-processed using the fast-Fourier-transform method proposed by Takeda et al. [96]. The displacement data was recorded at two different times after shock break out for each sample. The displacement variations along a particular direction, e.g., perpendicular to the ripples imprinted on the free surface by the rippled shock produced in these experiments, can be obtained from different line profiles after post-processing. Table 5.6 shows the times for each sample, at which TIDI data was recorded.

Table 5.6: Time at which TIDI data was recorded for rippled samples

Shot #	Time after shock break (ns), at which TIDI images were recorded	
	NTIDI	ETIDI
25274	19.86	26.28
25278	10.9	17.4

The TIDI data along with the post-processed displacement at the free surface for 25274 is shown in the figures 5.11 and 5.12.

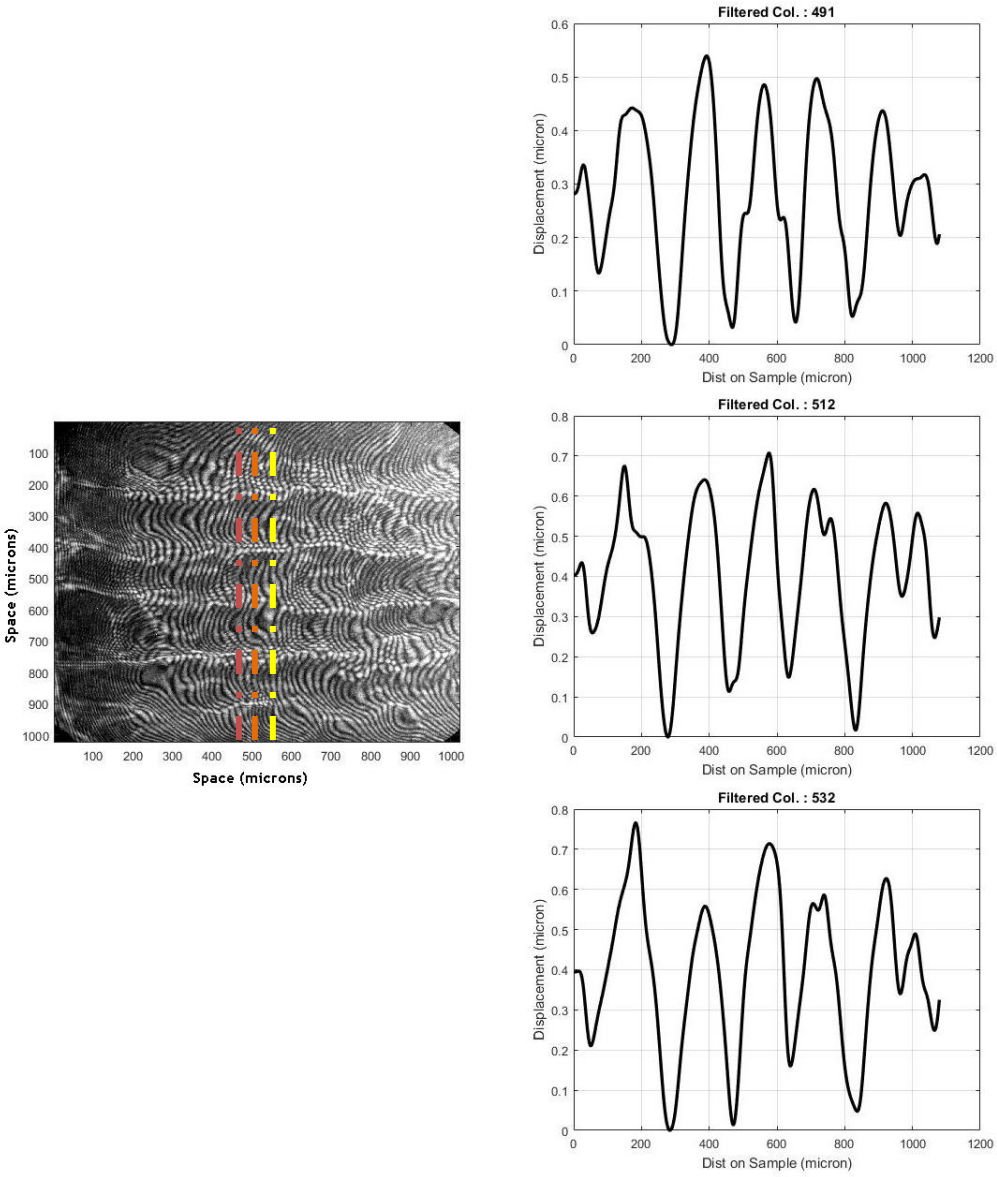

(a) (b)

Figure 5.11: a) TIDI data of s25274 at 19.86 ns after shock breakout; b) Displacement profiles on the sample, obtained after post processing along the red, orange and yellow lines indicated in 5.11 a.

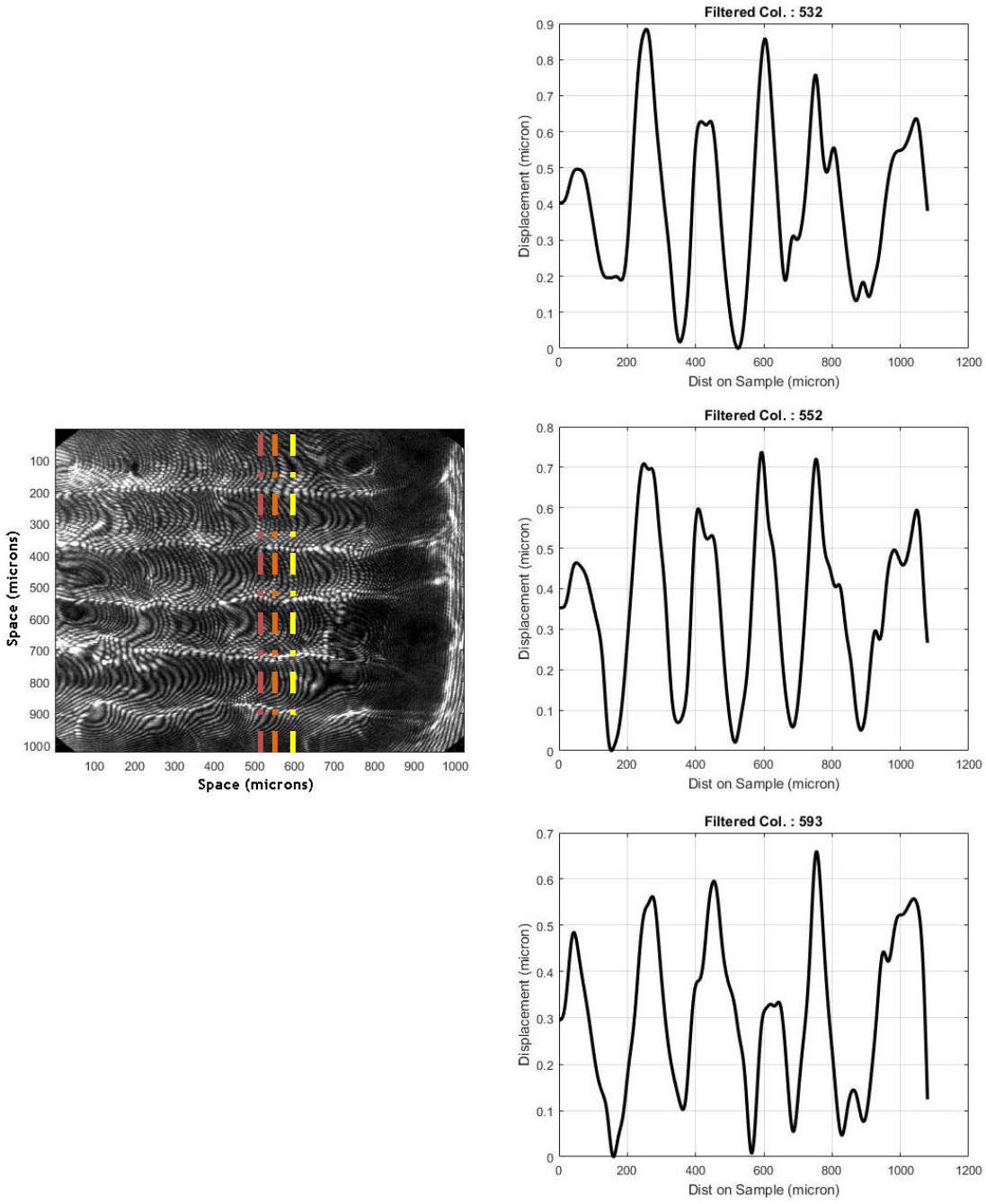

(a) (b)

Figure 5.12: a) TIDI data of s25274 at 26.28 ns after shock breakout; b) Displacement profiles on the sample, obtained after post processing, along the red, orange and yellow lines indicated in 5.12 a.

The mean peak to valley amplitude was measured from each plot and average of these values is the displacement at the free surface of the sample 25274. This was estimated to be 0.55±0.06 at the first TIDI timing and 0.64±0.08 at the second TIDI timing. The TIDI data for 25278 is shown in figures 5.13 and 5.14.

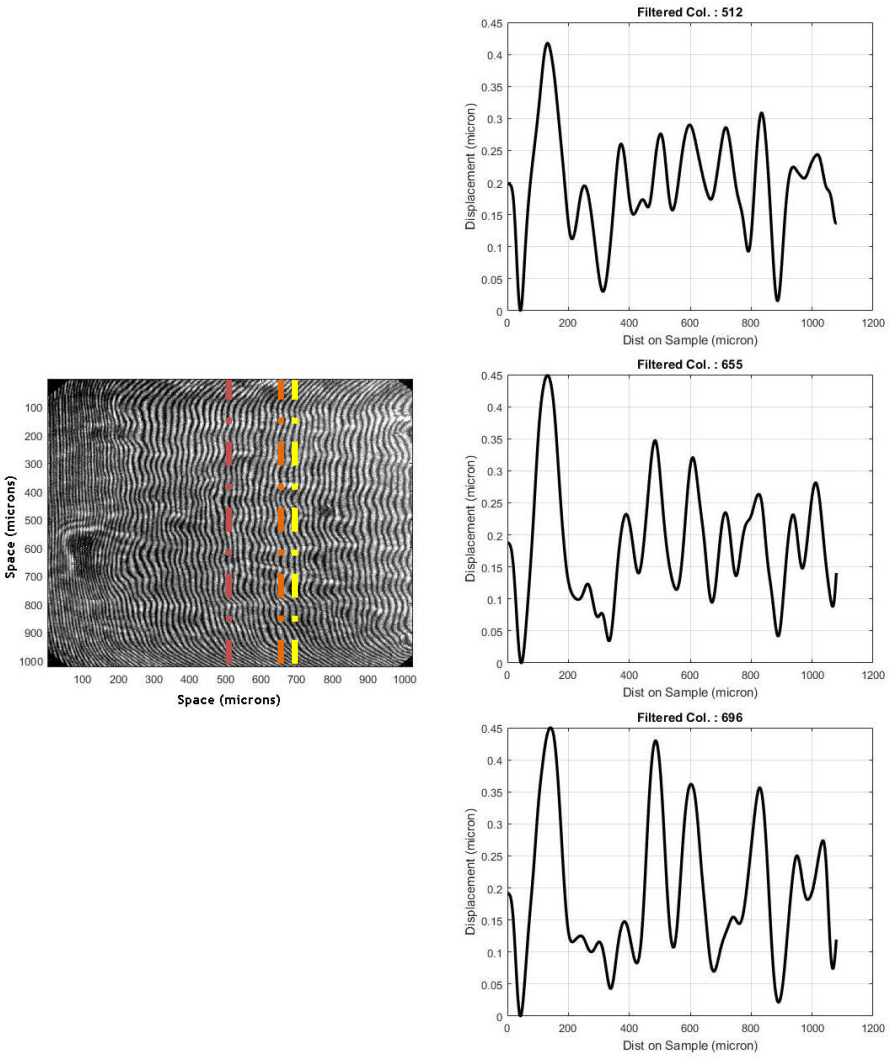

(a) (b)

Figure 5.13: a) TIDI data of s25278 at 10.9 ns after shock breakout; b) Displacement profiles on the sample, obtained after post processing, along the red, orange and yellow lines indicated in 5.13 a.

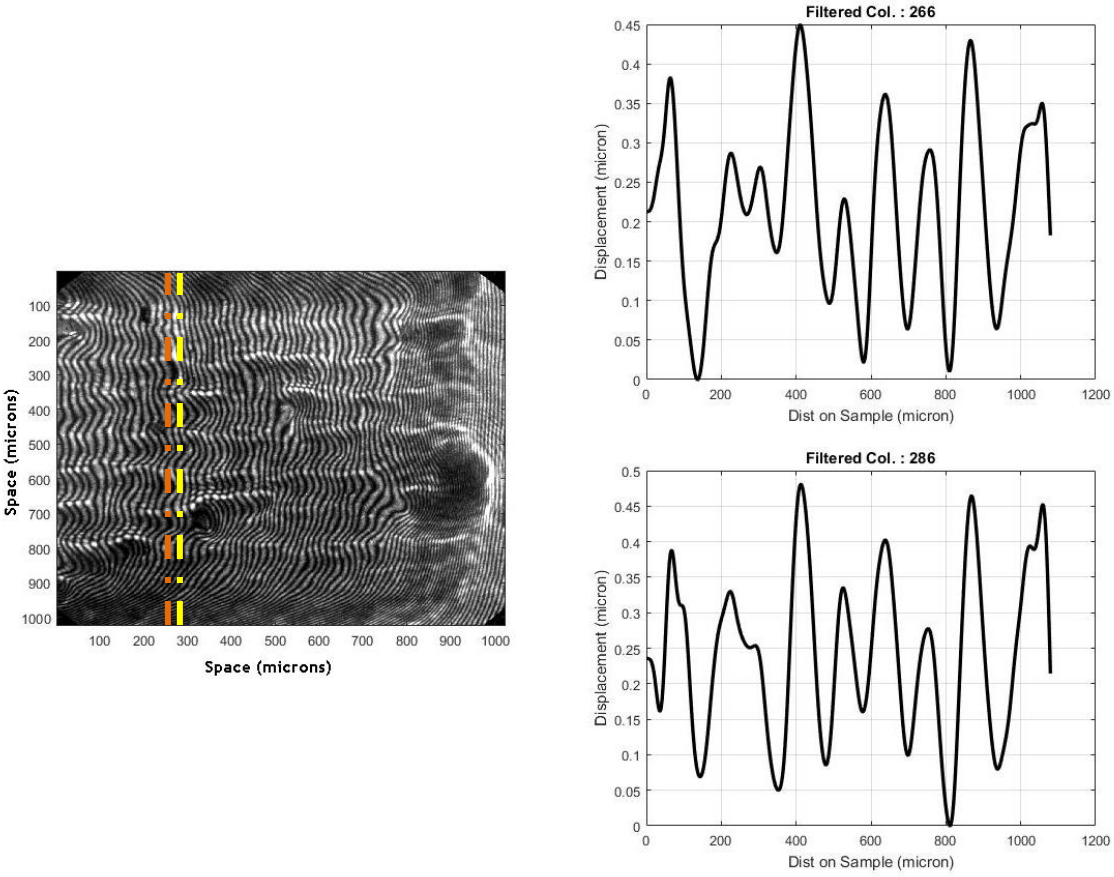

(a) (b)

Figure 5.14: a) TIDI data of s25278 at 17.4 ns after shock breakout; b) Displacement on the sample, obtained after post processing, along the lines indicated in 5.14 a.

The average displacement of 25278 at the free surface was around 0.19±0.05 at the first TIDI timing and 0.29±0.05 at the second TIDI timing.

In the TIDI output for both the samples, it can be noticed that the surface profile may not follow the same pattern throughout the sample. It can be noticed that the average grain size, from section 5.2, is close to the wavelength of the perturbations fabricated on the sample. These heterogeneities may be due to the presence of individual grains with an orientation or size different from the other around them. Hence, while post-

processing TIDI data, the amplitudes over several line profiles were taken and the average value was used to compare with the simulations. In addition to this, the average peak to valley distance was measured in the middle of the line profile plots, i.e., the data on either side or the data close to the edges was not taken into consideration. This is because release waves, which also tend to be perturbed, can have lateral effects and hence, certain length from the edges is neglected.

In the next chapter, simulations implemented using the rate independent elastic-perfectly plastic model and the rate-dependent PTW and Steinberg-Lund models will be discussed. The velocity history of the samples was used to calibrate the models and the displacement data was used as another experimental parameter with which the models can be validated.

CHAPTER 6

APPLICATION OF MATERIAL MODELS TO STUDY STRENGTH

Rate independent and rate dependent strength models were used to more closely study the dynamic strength of aluminium. The models were applied in simulations that tried to match experimental conditions as close as possible to the dynamic data of rippled samples. This will be further discussed in the rest of the chapter.

6.1 Elastic-Perfectly Plastic Model

In order to estimate the value of the dynamic yield strength of aluminium, Lagrangian simulations were also performed with the finite element code ABAQUS™ using explicit time integration. As mentioned before, simulations were done by using the elastic-perfectly plastic model coupled with the Mie-Grüneisen equation of state (MG-EOS). Prior to running the simulations in ABAQUS™, it was essential to estimate the boundary conditions to replicate the laser pulse condition. This was done using the 1D Lagrangian hydrocode LAGC1D, which used finite difference to solve the governing equations. A pressure boundary condition similar to the one shown in figure 5.7 resulted in a relatively square pulse. It was difficult to match the slope of the velocity curve during the rise and release, as can be seen in figure 6.1.

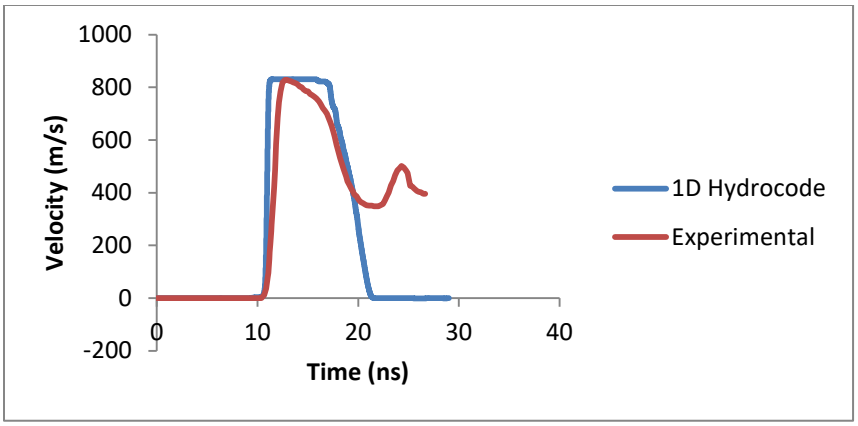

Figure 6.1: An example of the plot obtained by applying trapezoidal pressure pulse as a boundary condition with an elastic-perfectly plastic model.

Hence, the pressure profile was given smooth ramps while it changed from a low pressure to a peak pressure and when it dropped to zero after being held at the same value for a few nano-seconds. The pressure boundary condition for 25274 and 25278 that was used to match the velocity history from the simulation to the experimental is shown in figures 6.2 and 6.3. The comparison of simulation and experimental velocities after using this boundary condition is also included.

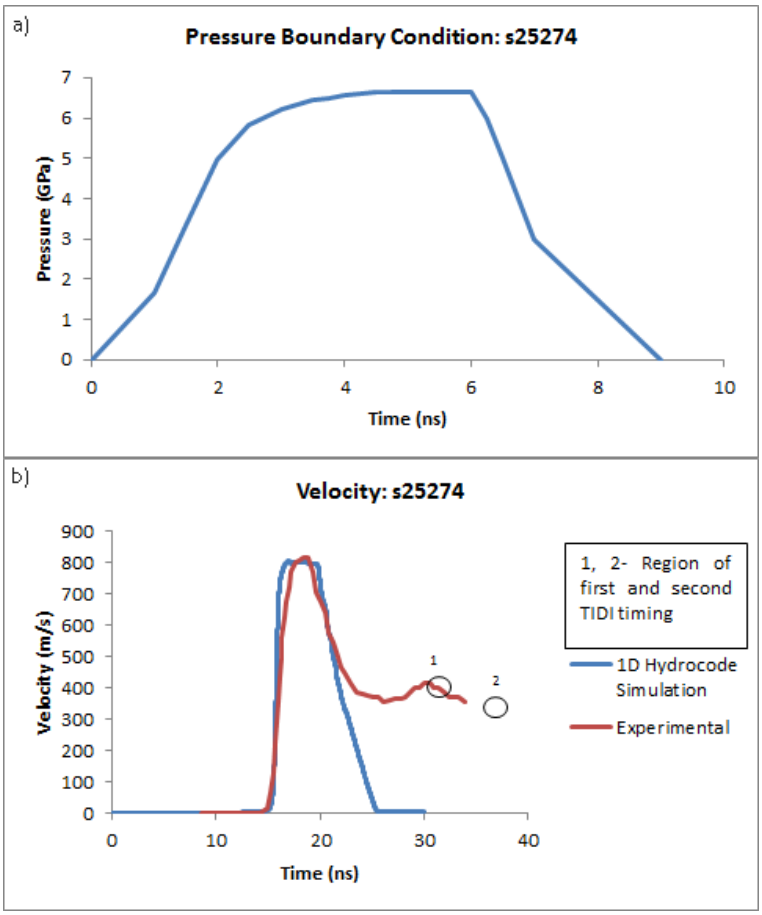

Figure 6.2: a) Pressure boundary condition b) Velocity history of s25274: 1D hydrocode and experimental.

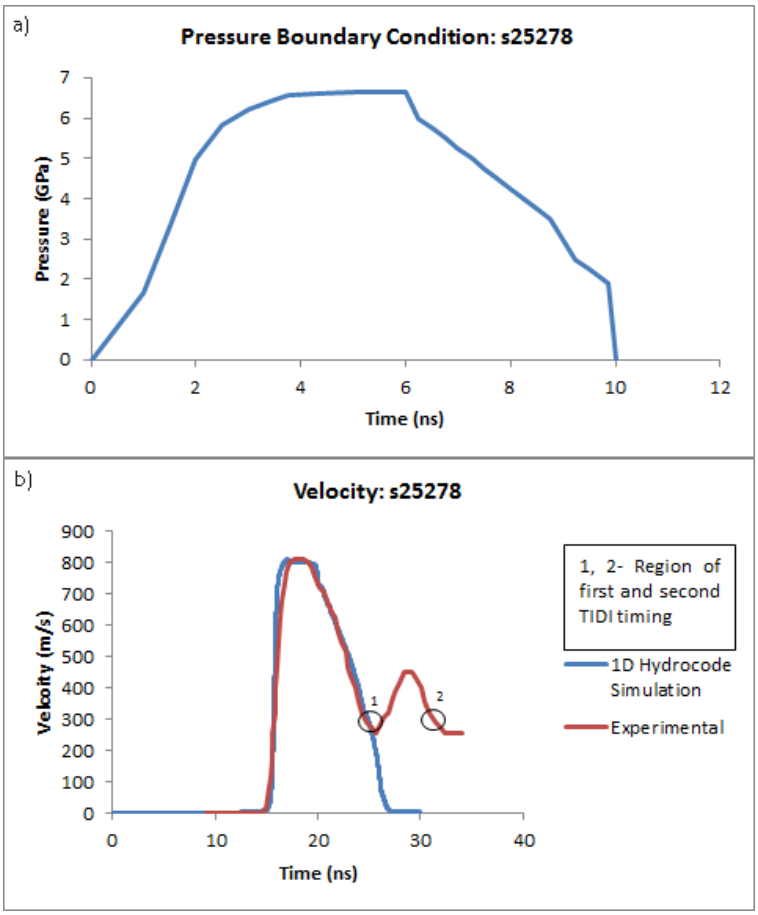

Figure 6.3: a) Pressure boundary condition b) Velocity history of s25278: 1D hydrocode and experimental.

The simulations show good agreement with the experimental velocities with very minor deviations. The boundary conditions shown in figures 6.2 a and 6.3 a were used to run the simulations in ABAQUS™. From the velocity history of 25278 and referring to table 5.4, it can be seen that the first TIDI timing is very close to the point of initiation of spall pullback and the second TIDI timing falls after the spall pullback. On the other hand, for 25274, both the TIDI timings fall after the pressure starts to rise again. In order to calibrate the closest value of the dynamic yield strength, the displacement data at the free surface for the first TIDI timing was obtained for different values of the yield

stress and compared with the experimental result. The deviation of the simulated displacement from the experimental value was obtained by subtracting it from the experimental displacement and was plotted as a function of yield stress. this is shown in figures 6.4 and 6.5.

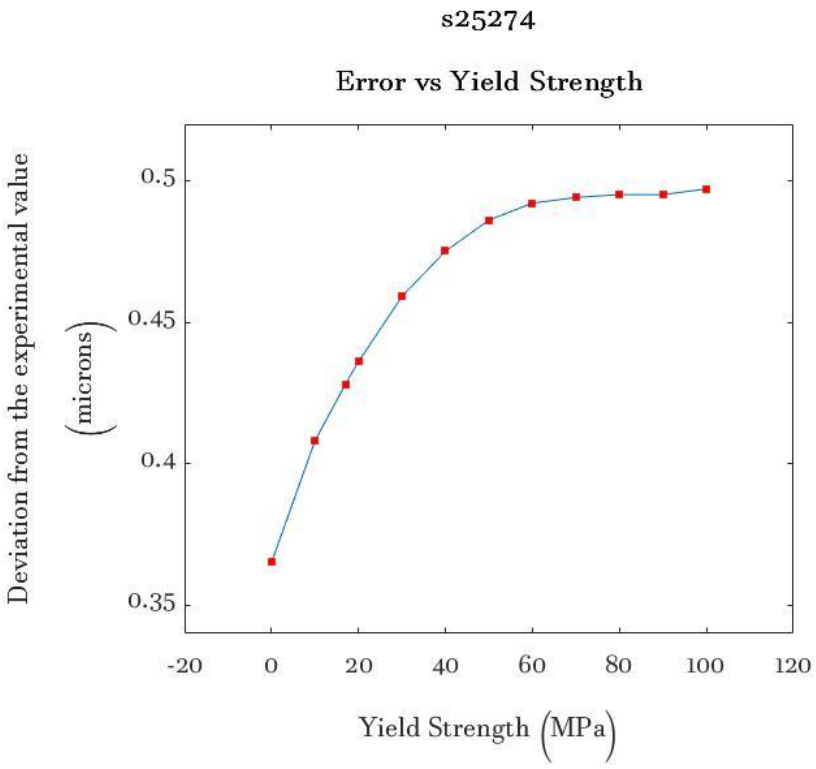

Figure 6.4: Error vs Yield Strength for s25274.

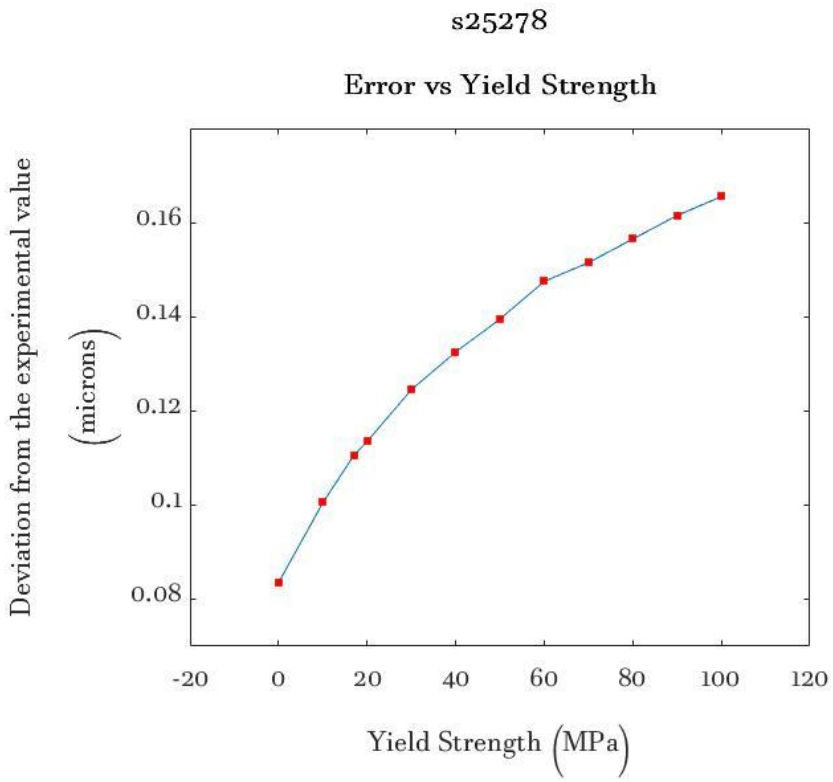

Figure 6.5: Error vs Yield Strength for s25278.

It can be seen that the displacement does not match with the experimental value and decreases with an increase in yield stress. In both the cases, the highest value of the displacement was obtained for an almost hydrodynamic simulation. For 25278, the value from the hydrodynamic simulation is 0.108, which is slightly closer to the lower limit of the experimental value. It can be seen in figure 6.5 that the deviation is the least for this almost no strength simulation. This may be due to the fact that the first TIDI timing for 25278 lies within the region for which the velocity history was matched.

On the other hand, in figure 6.4, for sample 25274, major deviations can be seen. This may be due to the fact that both the TIDI timings for 25274 lie in a region where there is a formation of tensile waves. The point where the pressure starts to rise again is known as spall pullback, and this causes spall damage. In the velocity history, there is no

velocity record at the second TIDI timing. This was because the path of the fringes could not be traced beyond this point. However, the diagnostic data was recorded within a time frame of almost 50 ns after shock break out.

Since, in 25278, the velocity history is good in the region of TIDI timings, now, let us see what happens if the spall pullback for 25278 is matched. In order to replicate the region of spall pullback, the pressure pulse was further changed to mimic the velocity history along with spall pullback. This was done for 25278 as shown in figure 6.6.

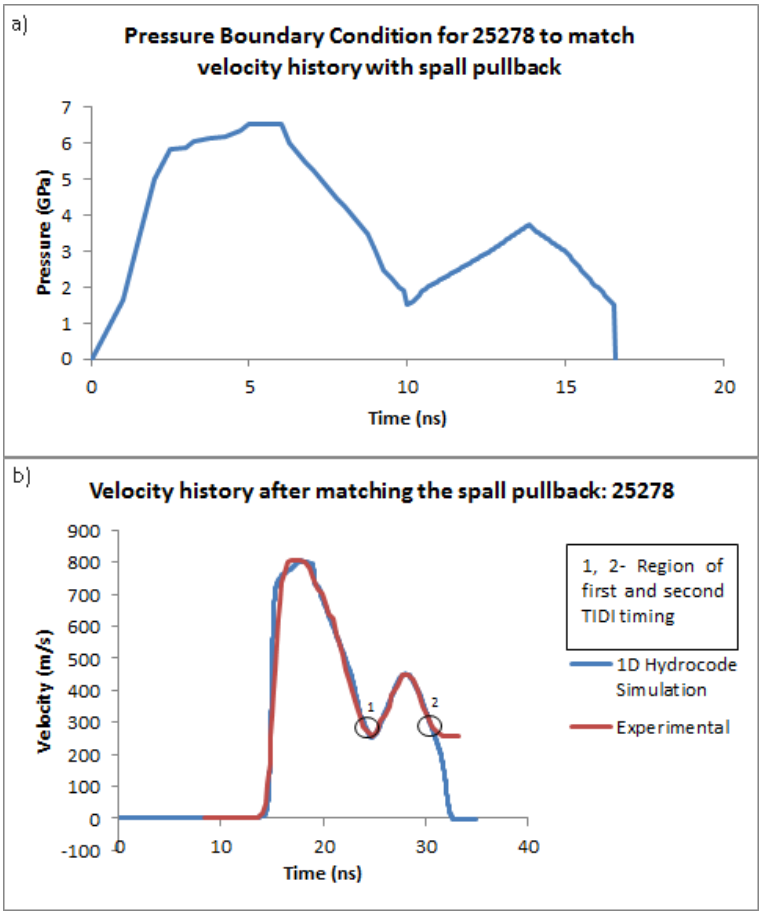

Figure 6.6: a) Pressure boundary condition to match the spall pullback b) Velocity history of s25278: 1D hydrocode and experimental.

The error in the displacement was then plotted for different values of yield stress, as shown in figure 6.7, to check if this pressure profile was able to match the displacement from the experiments. Since the spall pullback was also matched in the velocity history, the error plot was also obtained for the second TIDI timing and is shown in figure 6.8.

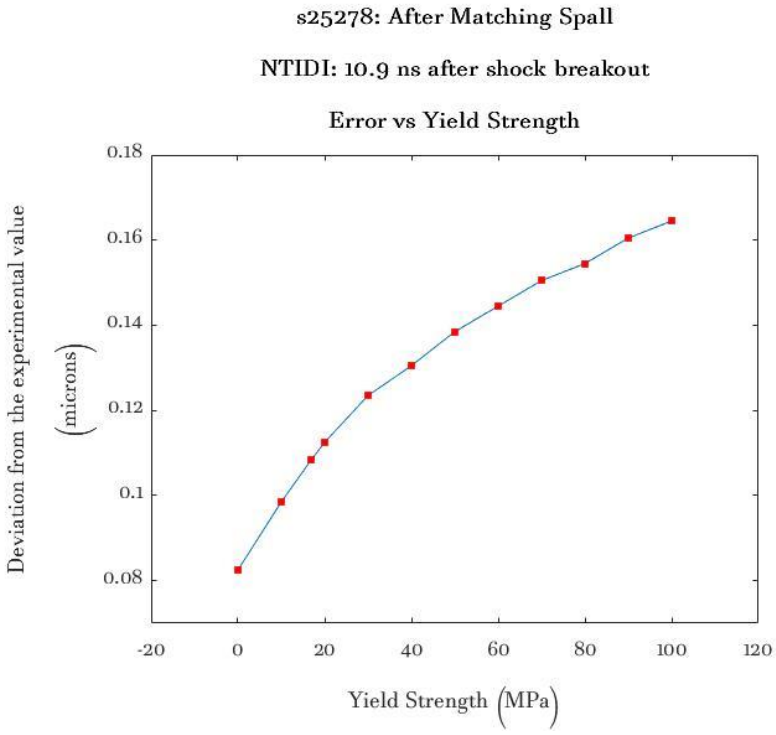

Figure 6.7: Error vs Yield Strength for 25278 after matching spall pullback at first

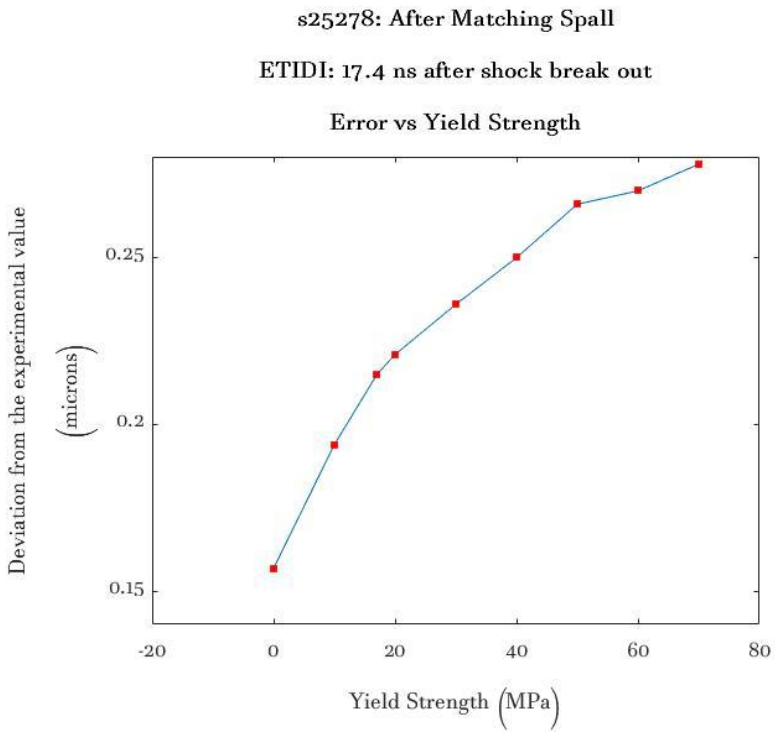

Figure 6.8: Error vs Yield Strength for 25278 after matching spall pullback at second TIDI timing.

As seen in figure 6.7 and 6.8, the results are similar to the one obtained without matching the spall pullback.

In all the cases, the displacement is closer to the experimental value only for a hydrodynamic simulation. Increasing the yield strength further decreased the amplitude of the perturbations at the free surface measured at the first TIDI timing, thereby increasing the difference between the simulation and experimental values. Although the elastic-perfectly plastic model could not predict the dynamic yield strength of the material even after closely matching the velocity profile, the typical effects of material strength on the growth of perturbation amplitude can be seen.

In an elastic-perfectly plastic model, there is no explicit strain rate dependence and the influence of the state of the material is not taken into consideration either. From the results in this section, it can be evidently seen that although the trapezoidal boundary condition was a very close match to replicate the experiment, in order to match the rise time of the experiments, it was necessary to modify the boundary condition in a way that is slightly different from the one used in experiments, i.e., the boundary condition was given smooth ramps both during the rise and release. In addition to this, the numerical simulations based on rate independent models do not consider real viscous-like behaviour of solids and instead use an artificial viscosity for the volumetric part of the response [50]. With artificial viscosity methods, the shock wave rise time depends on the artificial viscosity coefficient, which in turn affects the results from shock wave simulations [50]. These limitations of artificial viscosity were highlighted by Swegle et al. as they studied the shock viscosity and shock wave rise times in a variety of metals taking rate dependence and strain hardening into account as well as analysing the relationship between strain rate, Hugoniot stress and the effective viscosity in strong shock regimes [50], [110].

Figure 6.9 shows the velocity history was obtained from the 1D hydrocode by implementing an elastic-perfectly plastic model and applying a trapezoidal boundary condition.

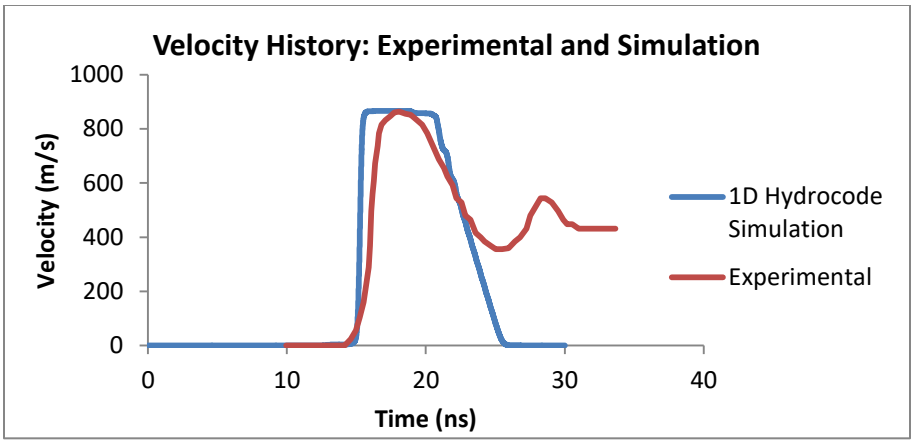

Figure 6.9: Velocity history showing elastic-plastic response for trapezoidal boundary condition.

As can be seen, the actual elastic-plastic response gives flat-topped pressure pulses. However, in the experimental velocity history, the top is not flat and is rather curved. This indicates the existence of rate dependence in the material behavior and means that the flow stress is rate-dependent [68].

The elastic-perfectly plastic model fails to provide an "average" value of dynamic yield strength of aluminium that leads to match of the displacement data collected. The rate dependence of the flow stress can be one of the reasons. However, the main reason for this is not clear at this stage. The data available is not enough to explore the other reasons that might have caused a mismatch in the experimental data that would validate this model. The failure of elastic plastic model to predict the dynamic yield strength has triggered the need to consider other material models that take additional parameters like strain rate, temperature, plastic strain, etc. into consideration and can provide better insight into studying the strength of aluminium under dynamic conditions. The implementation of rate-dependent models will be discussed further in the following sections.

6.2 Implementation of the Preston-Tonks-Wallace (PTW) Model

The basic equations governing the PTW model were presented in section 2.6. The role of each set of material parameters can be understood with the help of figure 6.10, in which the yield stress is plotted as a function of strain rate. S_0 and S_∞ are the values that the work hardening saturation stress takes at zero and melting temperatures, respectively, while, Y_0 and Y_∞ are the values of the yield stress at zero and melting temperatures, respectively. The PTW response plot indicates thermal activation and drag regimes and also the transition from one to the other. As seen in figure 6.10, for the same strain rate, increasing plastic strain increases strength via work hardening. The phonon drag region occurs at very high strain rates and it is insensitive to plastic strain. The slope of the thermal activation is controlled by κ, and the transition from thermal activation to the drag regime is set by the strain rate $\dot{\varepsilon}$, and the material constants Y_1, Y_2, which account for the abrupt change in strain rate sensitivity. The drag regime is mostly controlled by the strain rate $\dot{\varepsilon}$ and the constant β, which maintains the continuity of the stress.

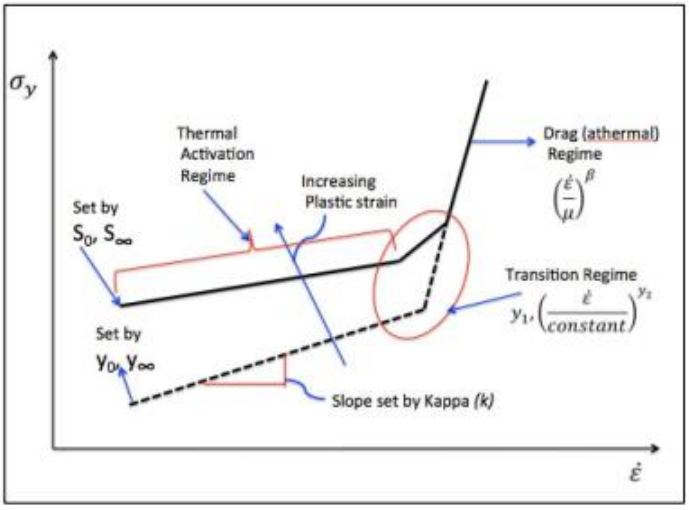

Figure 6.10: PTW response influenced by different material parameters [95].

The PTW response of aluminium was obtained using a point-integrator code, developed in matlab. The plot of yield stress vs strain rate was obtained for different plastic strains, and at a constant temperature. The PTW parameters for aluminium were obtained from Price et al. [67]. The experimental strain rate was calculated from equation 5.1. This experimental value was estimated to be of the order of $10^7\ s^{-1}$. Figure 6.11 shows the PTW response of aluminium for different plastic strains, and the region of experimental strain rate is also indicated. The reference PTW parameters from [67] are given in table 6.1.

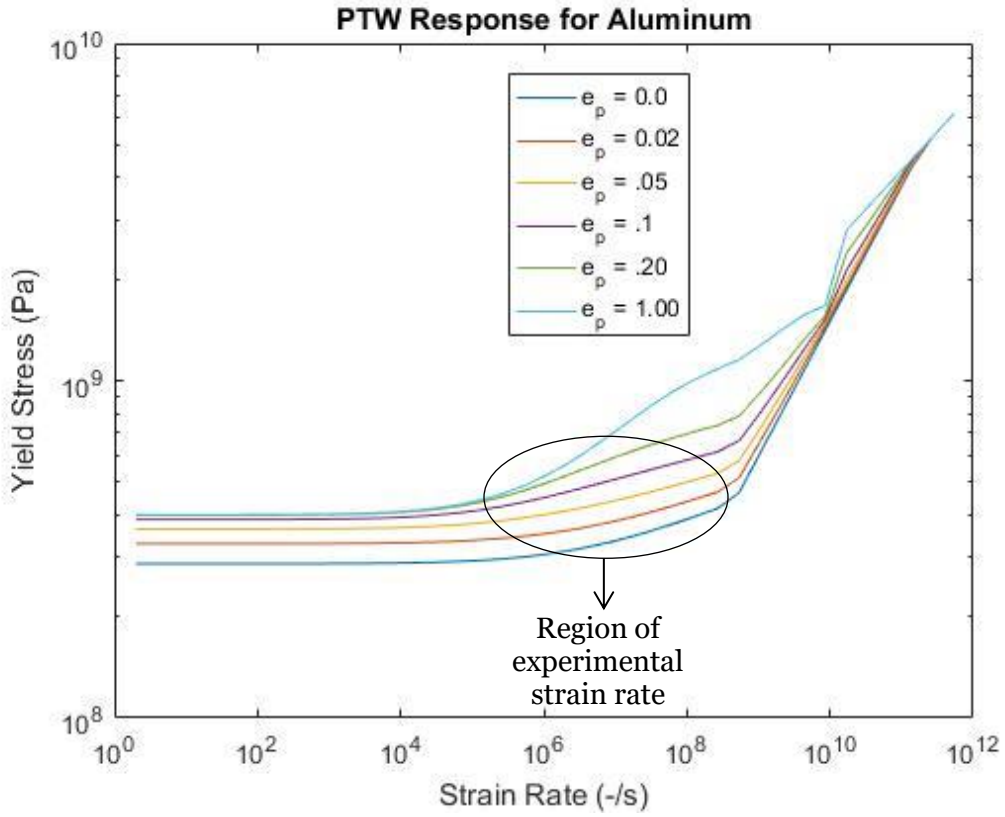

Figure 6.11: PTW response of aluminium at 300 K, showing region of experimental strain rate.

Table 6.1: Reference PTW Parameters [67]

Parameters	Description (with units)	Values
γ	Strain rate constant (-)	1.522e-4
θ	Strain hardening parameter (-)	0.0529
p	Strain hardening parameter (-)	3
S_0	Saturation stress factor (-)	0.032
S_∞	Saturation stress factor (-)	0.00791
κ	Constant of temperature dependence (-)	0.494
Y_0	Yield stress factor (-)	0.00942
Y_∞	Yield stress factor (-)	0.00566
Y_1	Medium strain rate constant (-)	0.0142
Y_2	Medium strain rate exponent (-)	0.40
β	Exponent in overdriven regime (-)	0.23
G_0	Reference shear modulus (GPa)	29.9
T_m	Melting Temperature (K)	932
M	Atomic mass (kg/atom)	4.480e-26

The reference PTW parameters were used for finite element simulations in ABAQUS™ to check if it was able to match the velocity history. As mentioned before, for sample 25274, both the TIDI timings lie after the spall pullback and for sample 25278, the first TIDI timing is close but before the spall pullback. Hence, the PTW model will be implemented for 25278 alone. In addition to this, the phenomenon of formation of damage due to tensile waves is not incorporated in this constitutive framework. Therefore, the agreement between simulation and experiment was sought only within the period of time before the spall pullback, as uncertainties increase after spall occurs.

A trapezoidal boundary condition was applied as shown in figure 6.12 a. The experimental velocity history was matched before the spall pullback, which is shown in figure 6.12 b.

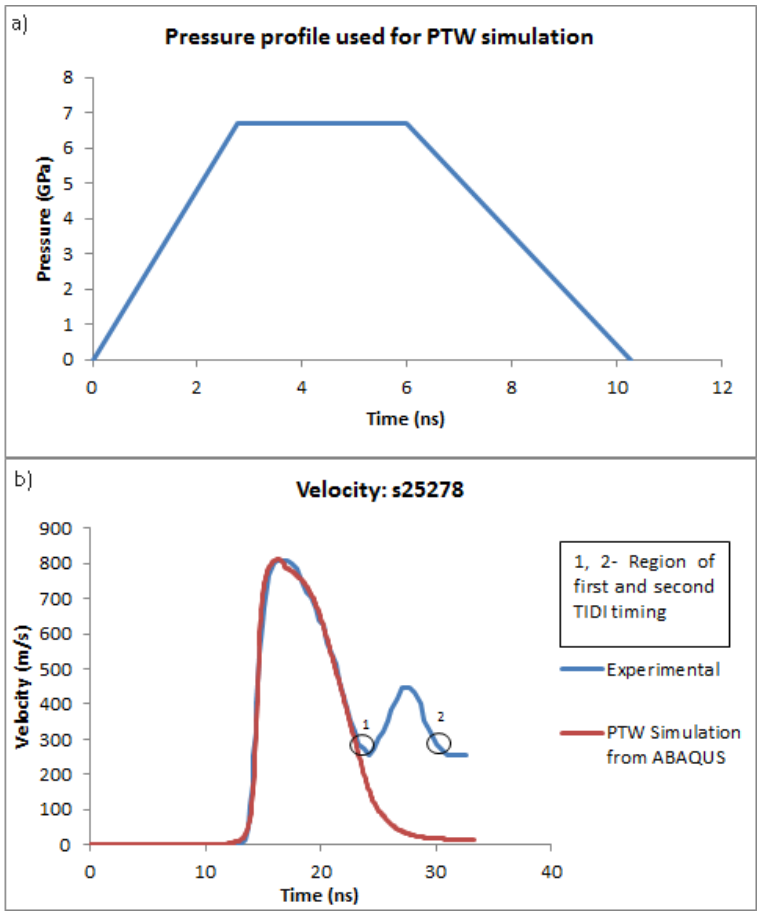

Figure 6.12: a) Pressure boundary condition to match the spall pullback; b) Velocity history of s25278 from PTW simulation and experiment.

The displacement of the free surface at the first TIDI timing, which is 10.9 ns after shock break out, was compared between experiment and simulation as shown in table 6.2.

Table 6.2: Comparison between experimental and simulated perturbation amplitude at the free surface for sample 25278.

Shot #	TIDI timing (ns)	Simulation time (ns)	Displacement (μm)	
			Experimental	Simulation
25278	10.9 ns after shock break out	24.3	0.19±0.05	0.161
	17.4 ns after shock break out	30.7	0.30±0.01	0.165

There is good agreement between simulation and experiment for the displacement at the first timing. The reference parameters from [67] work well for aluminium before the spall pullback. The prediction of displacement at the second TIDI timing differs by a margin of 44%, which is most likely due to the absence of spall pullback in the finite element model. This model was used as a reference to calibrate the rate dependent Steinberg-Lund model, without considering the region of spall and this will be discussed in the following section.

6.3 Calibration and Validation of the Steinberg-Lund Model

The governing equations of the Steinberg-Lund model were discussed in section 2.6 [68]. This model combines the effects of rate controlling mechanism in the thermal activation and dislocation drag regions. The expression for plastic strain given in equation 2.32, makes it rate dependent while the rate dependent part of the flow stress is lower than the Peierls stress, as given in equation 2.35.

The stress-strain behaviour in the various regions is dominated by various constants in the model. The values of C_1, U_k, and Y_p govern the thermally activated part and the

point of transition from thermal activation to drag region is solely controlled by the constant C_2. These constants have not been calibrated for aluminium to the best of our knowledge.

The plot of flow stress vs strain rate in figure 6.11 from the PTW model was used as a starting step in calibrating the constants in Steinberg-Lund model. The initial set of parameters was taken from several references and is given in table 6.3. This also includes values of constants to calculate C_1 and C_2 from equations 2.33 and 2.34.

Table 6.3: Initial Steinberg-Lund parameters for aluminium

Parameter	Description	Value	Reference
ρ	Dislocation density (m^{-2})	3.0e11	[111]
b	Burger's vector (m)	0.289e-9	[112]
ν	Debye frequency (rad/sec)	9.66e13	[113]
Y_p	Peierl's stress (Pa)	5.24e6	[114]
D	Drag coefficient (Pa-sec)	2e-5	[115]
a	Distance between Peierls valleys (m)	$\sim b$	[68]
L	Length of dislocation segment (m)	$\sim 10^4 b$	[68]
w	Width of a kink loop (m)	$\sim 24b$	[68]
U_k	Activation energy (eV) (Calculated using the formula from [116])	0.7	[116]
C_1	Constant in thermal activation region	21e6	Equation 2.33
C_2	Constant in the drag region	815	Equation 2.34

As already discussed, the Steinberg-Lund model is bound by the condition in equation 2.35, making it unphysical for $Y_t > Y_p$. Hence, beyond this point, Y_t was made equal to Y_p. From the PTW response in figure 6.11, it can be seen that the flow stress dependence on strain rate lies in the thermal activation region for the experimental strain rate value of $10^7\ s^{-1}$. Hence, for the most part of this calibration, the various constants, namely, Y_p, Y_a, U_k, C_1, and C_2 were varied to match the strain rate dependence

of the Steinberg-Lund model with the PTW model in the thermal activation region, especially in the region of experimental strain rate. Figure 6.13 shows the plot from Steinberg-Lund model that more closely matched the PTW model after varying these constants.

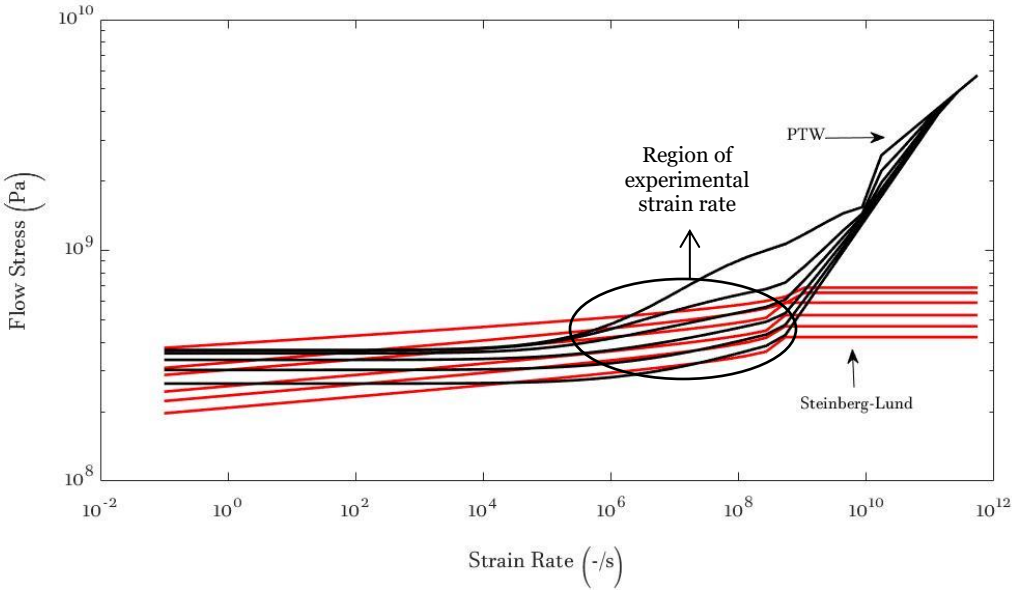

Figure 6.13: Comparison between PTW and Steinberg-Lund models after varying the constants.

After the response was matched with the PTW, simulations were run using the CTH hydrocode. As already discussed in chapter 4, a rippled flyer plate with the same amplitude and wavelength as the ripples on the sample was used to reproduce the boundary condition from the experiment. The surface that impacted the target was made of aluminium layer in order to make it a symmetric impact. A density gradient was applied on the flyer behind the impact layer in order to control the nature of the release waves from the flyer.

As a first step, the boundary condition from PTW model was used as a reference to calculate the different densities along the release. For this purpose, the equation of state parameters of aluminium, i.e., the speed of sound at zero pressure C_0 and the slope of the U_s-u_p line, s, were kept unchanged. Several points were taken on the release part of the velocity history, and the corresponding density was calculated from equation 5.2. In this equation, as an alternative, to get a range of densities, the speed of sound in aluminium, C, was also used instead of U_s, which is usually used for an elastic response [21]. The time after shock break out at which these points were located was used to obtain the corresponding pressure. Figure 6.14 shows the various points along the release that were used to calculate the density and the initial set of density values are shown in table 6.4.

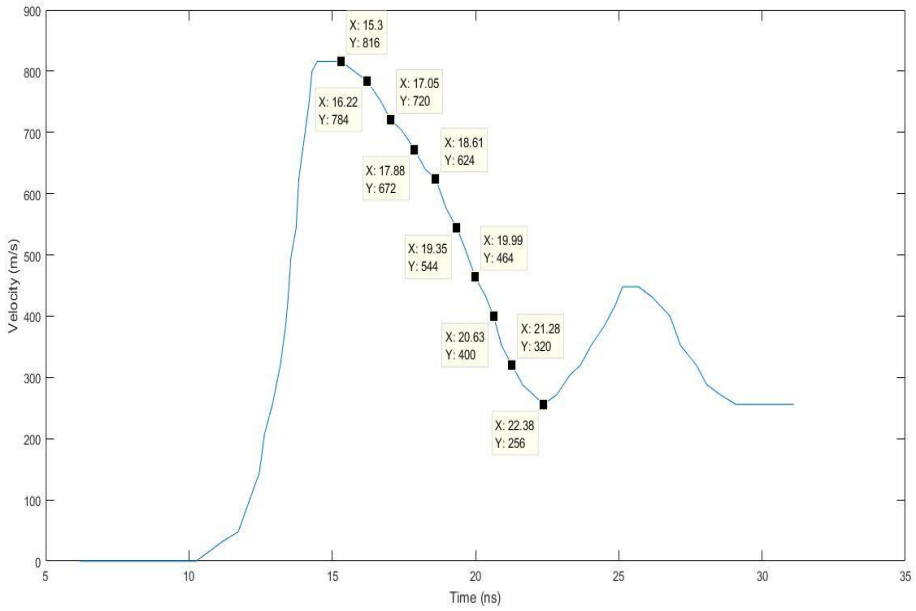

Figure 6.14: Velocity history showing points on the release for calculating densities.

Table 6.4: Initial density values used for CTH simulation

Using $\rho U_s U_p$	Using $\rho C U_p$
2600.3	2390.5
2127.5	1945.1
1662.1	1511
1170.9	1054.6
616.6	548.34

The simulations were initially run without material strength, i.e., pure hydrodynamic, in order to decide the optimum number of layers that would match the experimental velocity history. A flyer with 4 layers in addition to the aluminium layer predicted a close match to the velocity from the experiment. The densities decreased with every layer added above the aluminium layer. All the layers were of same thickness. The thickness of the aluminium layer was made slightly higher for the purpose of imparting the desired velocity at the time of impact and control the duration of the pulse. The geometry of the sample along with the flyer plate configuration is shown in figure 6.15. This configuration was used to run the simulations with the Steinberg-Lund model. With minor adjustments to the impact velocity, densities and spall strength, the velocity history at the free surface was matched with the experiment.

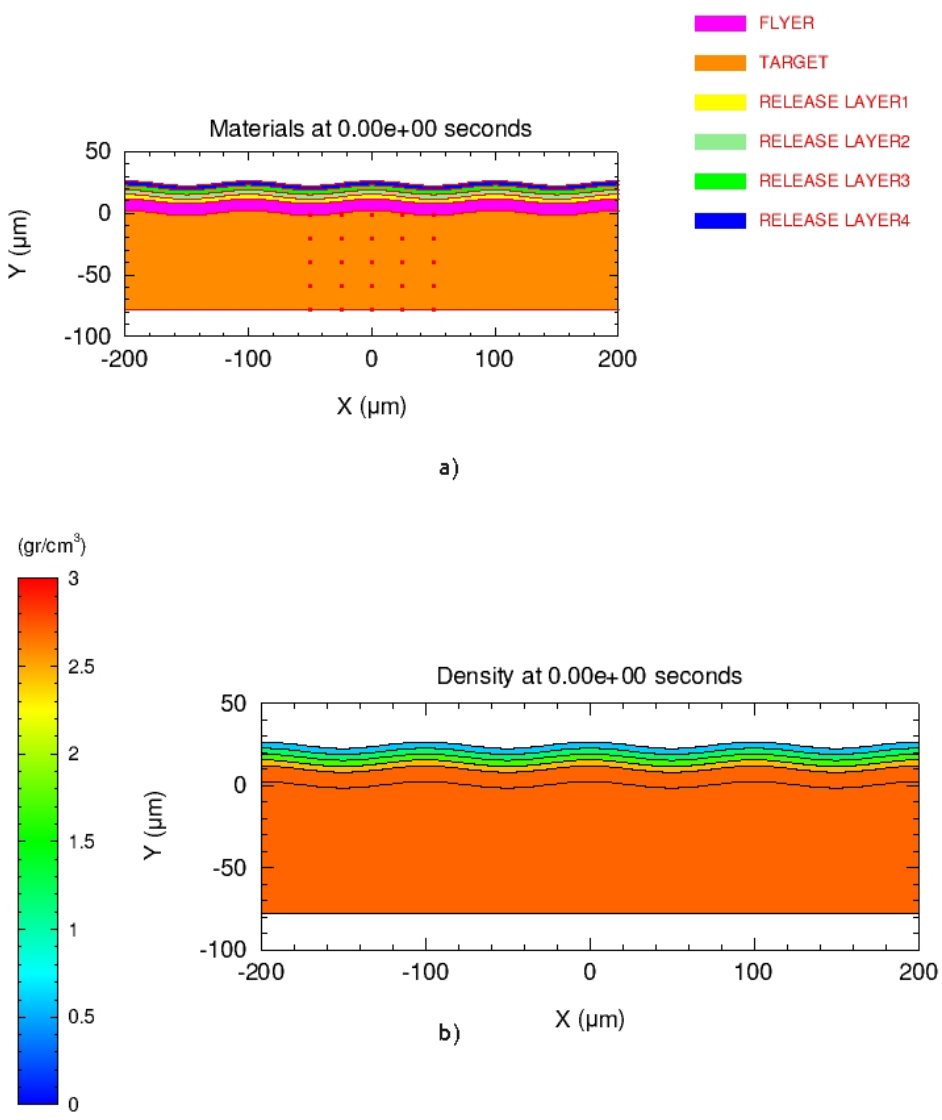

Figure 6.15: a) Geometry of the sample with a layered flyer plate; b) Density contour for the entire geometry.

The displacement of the free surface at the first TIDI timing was within the experimental error limits for a lower value of the athermal yield strength. Figure 6.16 shows the velocity history that matches the experiment. The comparison of displacement is shown in table 6.5.

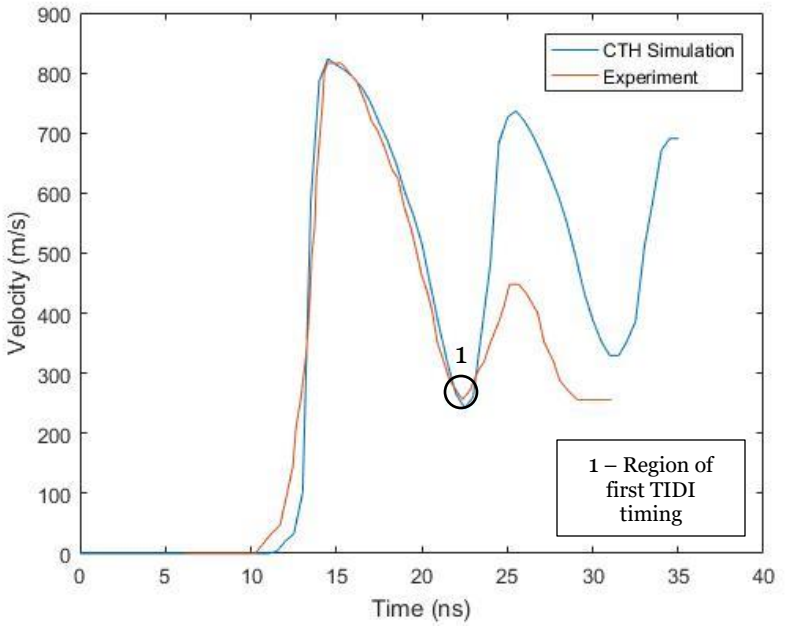

Figure 6.16: Comparison of velocity history of 25278 between CTH simulation and experiment.

Table 6.5: Comparison of perturbation amplitude at the free surface obtained from experiment and CTH simulation

Shot #	TIDI timing (ns)	Simulation time (ns)	Displacement (μm)	
			Experimental	Simulation
25278	10.9 ns after shock break out	23.05	0.19±0.05	0.21

Table 6.6 shows the final set of parameters that was used to match both the velocity history and displacement at first TIDI timing.

Table 6.6: Calibrated Steinberg-Lund parameters for aluminium

Parameter	Description	Value
Y_p	Peierl's stress (Pa)	1.6e8-2e8
Y_a	Athermal yield stress (Pa)	10e6
U_k	Activation energy (eV)	1.5
C_1	Constant in thermal activation region (sec)	1.5e8
C_2	Constant in the drag region (Pa-sec)	0.315

In the next section, the evolution of perturbation with time is studied, which will give more information about the strength predicted by each model.

6.4 Perturbation Growth Analysis

The evolution of perturbations at the free surface was plotted as a function of time. Since this was to observe the prediction of evolution from each model, an arbitrary value of yield strength was used for an elastic-perfectly plastic model. Figure 6.20 shows the plot of perturbation amplitude as a function of time for the three models.

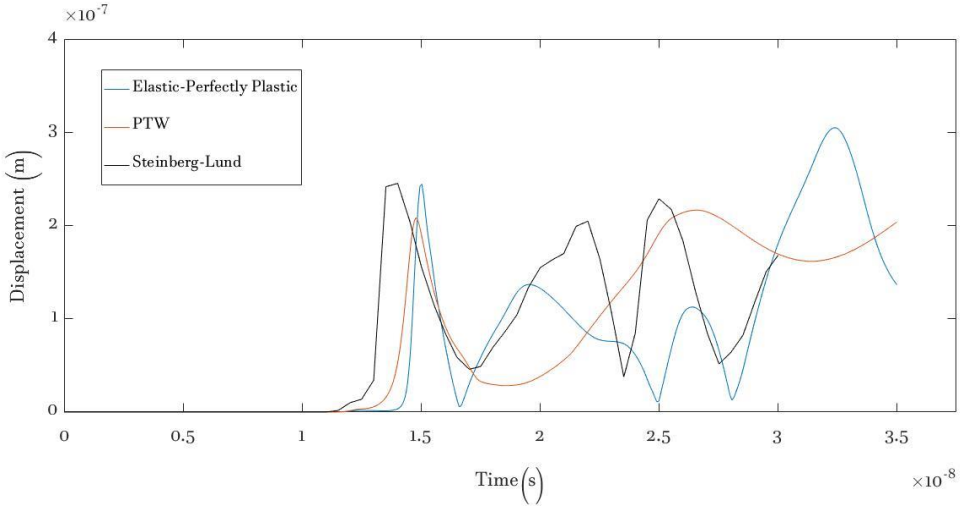

Figure 6.17: Evolution of perturbation amplitude with time from all the three models.

It can be observed that in all the three models, the initial growth at the time of shock break out looks similar, although the peak predicted at that point may change. The elastic-perfectly plastic and the Steinberg-Lund show that the amplitude of perturbation oscillates as it grows. The ripples imprinted on the free surface grow as a result of Richtmyer-Meshkov instability (RMI) and these oscillations maybe attributed to that. However, this behaviour is only mildly seen in PTW, i.e., the oscillations exist, but they are slower compared to the other two models. This may be due to high flow stress offered by the PTW model, which is damping the rapid growth as well as not allowing it to oscillate as much as the other models.

The phenomenon of inversion of perturbations on the free surface is one in which the positions of peak and valley are interchanged. An important point to consider here is that there may be uncertainties on the potential presence of an inversion. In addition to this, from figure 6.17, it can be seen that the dynamic evolution is largely different in all the three models. Although, the displacement predicted by the PTW and Steinberg-Lund models fall within the experimental limits, it is hard to estimate the correctness among these models due to the uncertainty of inversion and the difference in dynamic evolution between each model.

6.5 Discussion

From figure 6.17, it can be seen that at the first TIDI timing (~ near 2.5e-8 s), the PTW and Steinberg-Lund models predict amplitudes that are very close to each other. However, the elastic-perfectly plastic model predicts an overall lesser displacement at this point compared to the other models. If the material has considerably high strength, the simulations show that the amplitude of the rippled shock will reduce more slowly as

it travels through the thickness of the sample and the amplitude with which it hits the free surface will eventually be high. The growth of these amplitudes will be slower due to high strength. However, the growth at the free surface will be considerably high due to the larger amplitude of the rippled shock front at the time of break out, since it has been shown that the growth rate for RM as affected by strength is proportional to initial perturbation amplitude [15], [18]. For a lower strength, the rippled shock might lose its amplitude much sooner and the amplitude at the time of break out might not be as high. From results shown above, it can be clearly seen that the elastic-perfectly plastic model predicts a very low value of yield strength compared to the other two models, which agrees with this interpretation. It is likely that the dynamics of the evolution of perturbation amplitude are not captured accurately by the elastic-perfectly plastic model, as the strength will not change with the variations of strain rate that are likely to occur as the perturbation amplitude evolves in time, whereas a rate-dependent model would provide a closer predictions. Further work to examine the dynamics of the perturbation evolution is needed to shed light on this.

As mentioned in section 6.4, the possible presence of an inversion and the difference in model response to dynamic evolution triggers the need for further calibration of the constants in Steinberg-Lund model. The constants in the Steinberg-Lund model can be varied in different ways to match the experimental data. It is likely that the response of the model can be sensitive to each constant in table 6.6. The procedure followed in the previous sections in calibrating the Steinberg-Lund model has proved to work well for the aluminium samples in matching the velocity and displacement. However, it is essential to study the effects of each constant on the model response to check if the dynamic evolution can also be matched with the PTW model. The model can be further calibrated and validated in the following ways:

- Analysing the displacement data at both TIDI timings; if the TIDI timings fall after spall pullback, the velocity history after spall pullback has to be matched using an appropriate boundary condition.
- Testing this model on more aluminium samples shocked at different pressure conditions.

In addition to this, another sensitive aspect to be considered in this work is the timing of the TIDI data. It was in the region very close to the point of spall pullback, so small errors in timing can lead to several possibilities when trying to compare to simulations. It can be on the release curve, or on the point where the spall pullback starts. The time is located in a very sensitive position and hence, the probability for errors is high even if the time differs by a small amount. Sensitivity of the simulations to time needs to be carried out to ascertain the validity of the calibration.

CHAPTER 7

CONCLUSIONS

An experimental setup using a fed-thru Richtmyer-Meshkov instability was used to shock load aluminium and the diagnostic data obtained as well as modeling were used to study the dynamic behaviour. Several conclusions can be drawn from the work presented here.

Three models were separately studied and each model was calibrated by matching the velocity history with the experiment. This was followed by validation wherein the results were compared with experimental data not used for calibration.

The dynamic strength of aluminium was hard to predict using an elastic-perfectly plastic model, which is rate-independent. In an elastic-perfectly plastic model, the strength does not change after the material has reached the yield strength. It is likely that the dynamics of the evolution of perturbation amplitude are not captured accurately by the elastic-perfectly plastic model, as the strength will not change with the variations of strain rate that are likely to occur as the perturbation amplitude evolves in time, whereas a rate-dependent model would provide a closer predictions. However, the main reason for this type of model response is not clearly understood at this time.

It was evident that the PTW model, which is strongly rate dependent, worked well to match the displacement data collected for aluminium. Hence, there is a need for rate dependence to predominantly exist in order to closely predict the flow behaviour of aluminium.

The Steinberg-Lund (SL) model, which is a rate dependent model, has not yet been calibrated for aluminium, to the best of our knowledge. The PTW model was used as a starting step to do the calibration and it was found that it could be used to replicate the

behavior of the PTW model within the thermal activation regime. The calibrated model closely predicted the displacement at the free surface, which lies within the experimental error.

From the study of the variation of perturbation amplitude on the free surface as a function of time, it can be clearly seen that the response of PTW was more damped compared to the other models. Oscillations were seen in all the three models. However, the PTW model restricted oscillations to a greater extent compared to the other models. This indicates signs of a higher strength from this model. In addition to this, the dynamic evolution from each model was highly different from each other, which may be attributed to the difference in nature of the governing equations.

Hence, the calibration of the Steinberg-Lund model by using the PTW model as a reference has worked well for aluminum in matching the velocity and displacement data. However, due to the difference in dynamic evolution between these models, it is required to further validate this model as well as get more insight into the effect of each constant by using more experimental data. This can be done by testing this model on more aluminium samples shocked at different pressure conditions, as well as studying the sensitivity of model response to each constant.

CHAPTER 8

FUTURE WORK

[1] Studying the effects of spall pullback on the instabilities and try to extend the calibration and validation to the additional data available after the spall pullback.

[2] Study potential differences in dynamic evolution of perturbation amplitudes for different strength models and study the differences between rate independent and rate dependent models.

[3] Perform sensitivity analysis on predicted perturbation amplitudes with time, to quantify how robust the models are when compared with experimental data.

[4] Study the sensitivity of response of Steinberg-Lund model to various constants.

REFERENCES

[1] “Comprehensive Nuclear-Test-Ban Treaty.” [Online]. Available: https://en.wikipedia.org/wiki/Comprehensive_Nuclear-Test-Ban_Treaty. [Accessed: 03-Mar-2017].

[2] “GlobalSecurity.org.” .

[3] “Lawrence Livemore National Laboratory: Science and Technology Review.” [Online]. Available: https://str.llnl.gov.

[4] G. Dimonte, G. Terrones, F. J. Cherne, T. C. Germann, V. Dupont, K. Kadau, W. T. Buttler, D. M. Oro, C. Morris, and D. L. Preston, “Use of the Richtmyer-Meshkov instability to infer yield stress at high-energy densities,” *Phys. Rev. Lett.*, vol. 107, no. 26, pp. 1–4, 2011.

[5] “National Nuclear Security Administration.” [Online]. Available: https://nnsa.energy.gov/.

[6] R. Betti and O. A. Hurricane, “Inertial-confinement fusion with lasers,” *Nat. Phys.*, vol. 12, no. May, pp. 435–448, 2016.

[7] M. J. (University of N. D. McCready, “Introduction to Hydrodynamic Stability,” 1998. [Online]. Available: https://www3.nd.edu/~mjm/linstab.pdf.

[8] S. Atzeni and J. Meyer-ter-Vehn, *The Physics of Inertial Fusion: BeamPlasma Interaction, Hydrodynamics, Hot Dense Matter*, no. 125. Oxford University Press on Demand, 2004.

[9] “Rayleigh–Taylor instability.” [Online]. Available: https://en.wikipedia.org/wiki/Rayleigh–Taylor_instability. [Accessed: 03-Mar-2017].

[10] M. Brouillette, “The richtmyer-meshkov instability,” *Annu. Rev. Fluid Mech.*, vol. 34, no. 1, pp. 445–468, 2002.

[11] K. Nishihara, J. G. Wouchuk, C. Matsuoka, R. Ishizaki, and V. V Zhakhovsky, “Richtmyer--Meshkov instability: theory of linear and nonlinear evolution,” *Philos. Trans. R. Soc. London A Math. Phys. Eng. Sci.*, vol. 368, no. 1916, pp. 1769–1807, 2010.

[12] J. F. Barnes, P. J. Blewett, R. G. McQueen, K. A. Meyer, and D. Venable, “Taylor instability in solids,” *J. Appl. Phys.*, vol. 45, no. 2, pp. 727–732, 1974.

[13] A. R. Piriz, J. J. L. Cela, O. D. Cortázar, N. A. Tahir, and D. H. H. Hoffmann, “Rayleigh-Taylor instability in elastic solids,” *Phys. Rev. E - Stat. Nonlinear, Soft Matter Phys.*, vol. 72, no. 5, pp. 1–10, 2005.

[14] A. R. Piriz, J. J. L. Cela, and N. A. Tahir, “Rayleigh-Taylor instability in elastic-plastic solids,” *J. Appl. Phys.*, vol. 105, no. 11, 2009.

[15] A. R. Piriz, J. J. Lopez Cela, and N. A. Tahir, “Richtmyer-Meshkov instability as a tool for evaluating material strength under extreme conditions,” *Nucl. Instruments Methods Phys. Res. Sect. A Accel. Spectrometers, Detect. Assoc. Equip.*, vol. 606, no. 1–2, pp. 139–141, 2009.

[16] N. R. Barton, J. V. Bernier, R. Becker, A. Arsenlis, R. Cavallo, J. Marian, M. Rhee, H. S. Park, B. A. Remington, and R. T. Olson, “A multiscale strength model for extreme loading conditions,” *J. Appl. Phys.*, vol. 109, no. 7, 2011.

[17] P. Peralta, E. Loomis, Y. Chen, a. Brown, R. McDonald, K. Krishnan, and H. Lim, “Grain orientation effects on dynamic strength of FCC multicrystals at low shock pressures: a hydrodynamic instability study,” *Philos. Mag. Lett.*, vol. 95, no. 2, pp. 67–76, 2015.

[18] A. R. Piriz, J. J. Lopez Cela, N. A. Tahir, and D. H. H. Hoffmann, “Richtmyer-Meshkov instability in elastic-plastic media,” *Phys. Rev. E - Stat. Nonlinear, Soft Matter Phys.*, vol. 78, no. 5, pp. 1–10, 2008.

[19] S. Opie, S. Gautam, E. Fortin, J. Lynch, P. Peralta, and E. Loomis, “Behaviour of rippled shocks from ablatively-driven Richtmyer-Meshkov in metals accounting for strength,” *J. Phys. Conf. Ser.*, vol. 717, p. 12075, 2016.

[20] G. W. P. Iv, “Response of Materials to Various Shock Loading Conditions Generated by Plate Impact Experiments,” vol. 4, 2013.

[21] M. A. Meyers, *Dynamic behavior of materials*. John wiley & sons, 1994.

[22] S. N. DiGiacomo, “Characterization of plasticity and damage in shock loaded copper at various microstructural length scales,” Arizona State University, 2008.

[23] W. H. Holt, C. R. Crowe, and W. Mock Jr, “Dynamic Yield Stress and Elastic Wave Velocity Measurements for HF-1 Steel.,” 1976.

[24] H. Huang and J. R. Asay, “Reshock response of shock deformed aluminum,” *J. Appl. Phys.*, vol. 100, no. 4, p. 43514, 2006.

[25] W. W. Anderson, F. J. Cherne, M. A. Zocher, M. V Zhernokletov, and B. L. Glushak, *Material properties under intensive dynamic loading*. Springer Science & Business Media, 2007.

[26] L. K. Wayne, “Three-dimensional characterization of spall damage at microstructural weak links in shock-loaded copper polycrystals,” Arizona State University, 2009.

[27] R. L. Martineau, “A viscoplastic model of expanding cylindrical shells subjected to internal explosive detonations,” Colorado State University, 1998.

[28] G. I. Kanel, S. V Razorenov, and V. E. Fortov, *Shock-wave phenomena and the properties of condensed matter*. Springer Science & Business Media, 2013.

[29] C. Doolan, “A two-stage light gas gun for the study of high speed impact in propellants,” 2001.

[30] H. D. Espinosa and S. Nemat-Nasser, “Low-velocity impact testing,” *ASM Handb.*, vol. 8, pp. 539–559, 2000.

[31] W. N. Sharpe, *Springer handbook of experimental solid mechanics*. Springer Science & Business Media, 2008.

[32] C. S. Montross, T. Wei, L. Ye, G. Clark, and Y. W. Mai, “Laser shock processing and its effects on microstructure and properties of metal alloys: A review,” *Int. J. Fatigue*, vol. 24, no. 10, pp. 1021–1036, 2002.

[33] A. K. Tyagi and S. Banerjee, *Materials Under Extreme Conditions: Recent Trends and Future Prospects*. Elsevier Science, 2017.

[34] S. I. Ashitkov, M. B. Agranat, P. S. Komarov, V. E. Fortov, and others, “Behavior of aluminum near an ultimate theoretical strength in experiments with femtosecond laser pulses,” *JETP Lett.*, vol. 92, no. 8, pp. 516–520, 2010.

[35] M. H. Edwards, D. S. Whittaker, G. J. Tallents, P. Mistry, G. J. Pert, B. Rus, T. Mocek, M. Kozlov??, J. Polan, A. Praeg, M. Stupka, and P. Homer, “Laser-ablation rates measured using X-ray laser transmission,” *Phys. Rev. Lett.*, vol. 99, no. 19, pp. 5–8, 2007.

[36] D. C. Swift, A. Hauer, D. Paisley, and J. Niemczura, “Basic Material Properties Using Laser-Driven Shocks,” *Phys. Div. Res. Rev.*

[37] S. N. Luo, S. R. Greenfield, D. L. Paisley, R. P. Johnson, T. Shimada, D. D. Byler, E. N. Loomis, S. N. DiGiacomo, B. M. Patterson, K. J. McClellan, and others, “Long pulse laser driven shock wave loading for dynamic materials experiments,” in *High-Power Laser Ablation 2008*, 2008, p. 700514.

[38] C. Phipps, *Laser ablation and its applications*, vol. 129. Springer, 2007.

[39] W. M. Isbell, *Shock waves: measuring the dynamic response of materials*. Imperial College Press, 2005.

[40] R. Kraus, E. Loomis, S. Luo, A. Seifter, and D. Swift, “Experiment and Simulations of Ablatively Driven Shock Waves in Gadolinium Metal,” in *APS Shock Compression of Condensed Matter Meeting Abstracts*, 2007.

[41] C. A. Bolme and K. J. Ramos, “Line-imaging velocimetry for observing spatially heterogeneous mechanical and chemical responses in plastic bonded explosives during impact,” *Rev. Sci. Instrum.*, vol. 84, no. 8, 2013.

[42] P. M. Celliers, D. J. Erskine, C. M. Sorce, D. G. Braun, O. L. Landen, and G. W. Collins, “A high-resolution two-dimensional imaging velocimeter,” *Rev. Sci. Instrum.*, vol. 81, no. 3, 2010.

[43] D. H. Dolan, *Foundations of VISAR analysis*. Citeseer, 2006.

[44] W. F. Hemsing, “Line-imaging Laser Interferometers for Measuring Velocities.”

[45] S. N. Luo, D. C. Swift, T. E. Tierney IV, D. L. Paisley, G. A. Kyrala, R. P. Johnson, A. A. Hauer, O. Tschauner, and P. D. Asimow, “Laser-induced shock waves in condensed matter: some techniques and applications,” *High Press. Res.*, vol. 24, no. 4, pp. 409–422, 2004.

[46] L. M. Barker, “The development of the VISAR, and its use in shock compression science,” *Shock Compression Condens. Matter - 1999*, vol. 55, no. 11, pp. 11–17, 2000.

[47] L. Wayne, K. Krishnan, S. Digiacomo, N. Kovvali, P. Peralta, S. N. Luo, S. Greenfield, D. Byler, D. Paisley, K. J. McClellan, A. Koskelo, and R. Dickerson, “Statistics of weak grain boundaries for spall damage in polycrystalline copper,” *Scr. Mater.*, vol. 63, no. 11, pp. 1065–1068, 2010.

[48] S. R. Greenfield, S. N. Luo, D. L. Paisley, E. N. Loomis, D. C. Swift, and A. C. Koskelo, “Transient Imaging Displacement Interferometry applied to shock loading,” *AIP Conf. Proc.*, vol. 955, pp. 1093–1096, 2007.

[49] S. R. Greenfield, “Transient Interferometric Studies of Shocked Bicrystals,” *AIP Conf. Proc.*, vol. 706, no. 2004, pp. 1269–1272, 2004.

[50] J. W. Swegle and D. E. Grady, “Shock viscosity and the prediction of shock wave rise times,” *J. Appl. Phys.*, vol. 58, no. 2, pp. 692–701, 1985.

[51] J. Lépinoux, D. Mazière, V. Pontikis, and G. Saada, *Multiscale phenomena in plasticity: from experiments to phenomenology, modelling and materials engineering*, vol. 367. Springer Science & Business Media, 2012.

[52] G. Regazzoni, U. F. Kocks, and P. Follansbee, “Dislocation kinetics at high strain rates,” *Acta Metall.*, vol. 35, no. 12, pp. 2865–2875, 1987.

[53] A. Kumar, F. E. Hauser, and J. E. Dorn, “Viscous drag on dislocations in aluminum at high strain rates,” *Acta Metall.*, vol. 16, no. 9, pp. 1189–1197, 1968.

[54] S. J. Zhou, D. L. Preston, P. S. Lomdahl, and D. M. Beazley, “Large-scale molecular dynamics simulations of dislocation intersection in copper,” *Science (80-.).*, vol. 279, no. 5356, pp. 1525–1527, 1998.

[55] T. J. Vogler, T. Ao, and J. R. Asay, “High-pressure strength of aluminum under quasi-isentropic loading,” *Int. J. Plast.*, vol. 25, no. 4, pp. 671–694, 2009.

[56] “Manual for the Calculation of Elastic-Plastic Materials Models Parameters,” *Natl. Phys. Lab.*, p. 49, 2007.

[57] C. Jenkins and S. Khanna, “Mechanics-Materials-Design.” [Online]. Available: http://www1.us.elsevierhealth.com/books.elsevier/companionsites/JenkinsKhanna/mmd/yieldpoint/yieldpointa.html. [Accessed: 08-Mar-2017].

[58] G. R. Johnson and W. H. Cook, “A constitutive model and data for metals subjected to large strains, high strain rates and high temperatures,” *7th International Symposium on Ballistics*. pp. 541–547, 1983.

[59] Y. Zhang, J. C. Outeiro, and T. Mabrouki, “On the selection of Johnson-Cook constitutive model parameters for Ti-6Al-4V using three types of numerical models of orthogonal cutting,” *Procedia CIRP*, vol. 31, pp. 112–117, 2015.

[60] D. J. Steinberg, S. G. Cochran, and M. W. Guinan, “A constitutive model for metals applicable at high-strain rate,” *J. Appl. Phys.*, vol. 51, no. 3, pp. 1498–1504, 1980.

[61] F. J. Zerilli and R. W. Armstrong, “Dislocation-mechanics-based constitutive relations for material dynamics calculations,” *J. Appl. Phys.*, vol. 61, no. 5, pp. 1816–1825, 1987.

[62] C. Y. Gao and L. C. Zhang, “A constitutive model for dynamic plasticity of FCC metals,” *Mater. Sci. Eng. A*, vol. 527, no. 13–14, pp. 3138–3143, 2010.

[63] G. Z. Voyiadjis and F. H. Abed, “Microstructural based models for bcc and fcc metals with temperature and strain rate dependency,” *Mech. Mater.*, vol. 37, no. 2–3 SPEC. ISS., pp. 355–378, 2005.

[64] P. Follansbee and U. F. Kocks, “A constitutive description of the deformation of copper based on the use of the mechanical treshold as an internal state variable,” *Acta Metall.*, vol. 36, no. I, pp. 81–97, 1988.

[65] E. S. Puchi-Cabrera, C. Villalobos-Gutiérrez, and G. Castro-Fariñas, “On the Mechanical Threshold Stress of Aluminum: Effect of the Alloying Content,” *J. Eng. Mater. Technol.*, vol. 123, no. 2, p. 155, 2001.

[66] D. L. Preston, D. L. Tonks, and D. C. Wallace, “Model of plastic deformation for extreme loading conditions,” *J. Appl. Phys.*, vol. 93, no. 1, pp. 211–220, 2003.

[67] M. C. Price, A. T. Kearsley, and M. J. Burchell, “Validation of the Preston-Tonks-Wallace strength model at strain rates approaching ???1011 s-1 for Al-1100, tantalum and copper using hypervelocity impact crater morphologies,” *Int. J. Impact Eng.*, vol. 52, pp. 1–10, 2013.

[68] D. J. Steinberg and C. M. Lund, “A constitutive model for strain rates from 10-4 to 106 s-1,” *J. Appl. Phys.*, vol. 65, no. 4, pp. 1528–1533, 1989.

[69] F. Wang, J. Glimm, and B. J. Plohr, “A MODEL FOR RATE-DEPENDENT PLASTICITY FENG WANG, JAMES GLIMM and BRADLEY J. PLOHR,” vol. 43, no. 9, 1995.

[70] E. N. Loomis, S. R. Greenfield, R. P. Johnson, J. A. Cobble, S. N. Luo, D. S. Montgomery, and M. M. Marinak, “Investigations into the seeding of instabilities due to x-ray preheat in beryllium-based inertial confinement fusion targets,” *Phys. Plasmas*, vol. 17, no. 5, 2010.

[71] S. M. Bakhrakh, O. B. Drennov, and N. P. Kovalev, “Hydrodynamic instability in strong media,” 1997.

[72] D. H. Sharp, “An overview of Rayleigh-Taylor instability,” *Phys. D Nonlinear Phenom.*, vol. 12, no. 1–3, pp. 3–18, 1984.

[73] S. Li and H. Li, “Parallel AMR code for compressible MHD or HD equations,” *Los Alamos Natl. Lab. Retrieved*, pp. 5–9, 2006.

[74] C. J. He, H. B. Zhou, and Y. H. Hang, “A numerical study on Rayleigh-Taylor instability of aluminum plates driven by detonation,” *Sci. China Physics, Mech. Astron.*, vol. 53, no. 2, pp. 195–198, 2010.

[75] H. S. Park, B. A. Remington, R. C. Becker, J. V. Bernier, R. M. Cavallo, K. T. Lorenz, S. M. Pollaine, S. T. Prisbrey, R. E. Rudd, and N. R. Barton, “Strong stabilization of the Rayleigh-Taylor instability by material strength at megabar pressures,” *Phys. Plasmas*, vol. 17, no. 5, 2010.

[76] R. T. Olson, E. K. Cerreta, C. Morris, a M. Montoya, F. G. Mariam, a Saunders, R. S. King, E. N. Brown, G. T. Gray, and J. F. Bingert, “The effect of microstructure on Rayleigh-Taylor instability growth in solids,” *J. Phys. Conf. Ser.*, vol. 500, no. 11, p. 112048, 2014.

[77] Y. Aglitskiy, M. Karasik, A. L. Velikovich, V. Serlin, J. L. Weaver, T. J. Kessler, S. P. Nikitin, A. J. Schmitt, S. P. Obenschain, N. Metzler, and J. Oh, “Observed transition from Richtmyer-Meshkov jet formation through feedout oscillations to Rayleigh-Taylor instability in a laser target,” *Phys. Plasmas*, vol. 19, no. 10, 2012.

[78] A. C. Robinson and J. W. Swegle, “Acceleration instability in elastic-plastic solids. II. Analytical techniques,” *J. Appl. Phys.*, vol. 66, no. 7, pp. 2859–2872, 1989.

[79] J. R. Asay, L. P. Mix, and F. C. Perry, “Ejection of material from shocked surfaces,” *Appl. Phys. Lett.*, vol. 29, no. 5, pp. 284–287, 1976.

[80] W. T. Buttler, D. M. Oró, D. L. Preston, K. O. Mikaelian, F. J. Cherne, R. S. Hixson, F. G. Mariam, C. Morris, J. B. Stone, G. Terrones, and D. Tupa, “Unstable Richtmyer–Meshkov growth of solid and liquid metals in vacuum,” *J. Fluid Mech.*, vol. 703, no. 2012, pp. 60–84, 2012.

[81] X. Chen, J. R. Asay, S. K. Dwivedi, and D. P. Field, “Spall behavior of aluminum with varying microstructures,” *J. Appl. Phys.*, vol. 99, no. 2, 2006.

[82] S. J. Bless, “Spall criteria for several metals,” 1981.

[83] M. A. Meyers and C. Taylor Aimone, “Dynamic fracture (spalling) of metals,” *Prog. Mater. Sci.*, vol. 28, no. 1, pp. 1–96, 1983.

[84] K. Krishnan, “3D Modeling of Incipient Spall Damage in Shocked FCC Multicrystals,” Arizona State University, 2013.

[85] J. H. Oscarson and K. F. Graff, “Spall fracture and dynamic response of materials,” 1968.

[86] J. R. Asay and M. Shahinpoor, *High-pressure shock compression of solids*. Springer Science & Business Media, 2012.

[87] D. Curran, “Dynamic failure of solids,” *Phys. Rep.*, vol. 147, no. 5–6, pp. 253–388, 1987.

[88] G. I. Kanel, S. J. Bless, and A. M. Rajendran, “Behavior of brittle materials under dynamic loading,” 2000.

[89] S. Hashemian, S. Digiacomo, P. Peralta, H. D’Armas, S. N. Luo, E. Loomis, D. Paisley, D. Byler, R. Dickerson, and K. J. McCllelan, “Effects of microstructure on spall damage localization in shock loaded copper multicrystals,” in *TMS 2008 Annual Meeting Supplemental: Materials Processing and Properties*, 2008.

[90] P. Peralta, S. DiGiacomo, S. Hashemian, S.-N. Luo, D. Paisley, R. Dickerson, E. Loomis, D. Byler, K. J. Mcclellan, and H. D’Armas, “Characterization of Incipient Spall Damage in Shocked Copper Multicrystals,” *Int. J. Damage Mech.*, vol. 18, no. 4, pp. 393–413, 2008.

[91] T. Antoun, *Spall fracture*. Springer Science & Business Media, 2003.

[92] G. I. Kanel, S. V. Razorenov, A. Bogatch, A. V. Utkin, and D. E. Grady, “Simulation of spall fracture of aluminum and magnesium over a wide range of load duration and temperature,” *Int. J. Impact Eng.*, vol. 20, no. 6, pp. 467–478, 1997.

[93] G. I. Kanel, S. V. Razorenov, K. Baumung, and J. Singer, “Dynamic yield and tensile strength of aluminum single crystals at temperatures up to the melting point,” *J. Appl. Phys.*, vol. 90, no. 1, pp. 136–143, 2001.

[94] G. H. Miller and T. J. Ahrens, “Shock-wave viscosity measurement,” *Rev. Mod. Phys.*, vol. 63, no. 4, pp. 919–948, 1991.

[95] S. Gautam, “Effects of Dynamic Material Strength on Hydrodynamic Instability and Damage Evolution in Shock Loaded Copper,” Arizona State University, 2016.

[96] M. Takeda, H. Ina, and S. Kobayashi, “Fourier-transform method of fringe-pattern analysis for computer-based topography and interferometry,” *J. Opt. Soc. Am.*, vol. 72, no. 1, p. 156, 1982.

[97] J. I. Martinez and D. W. Schmidt, “diamond turning and linear sine wave profiling,” 2015.

[98] “Allied High Tech.” [Online]. Available: http://www.alliedhightech.com.

[99] A. E. Giannakopoulos, P. L. Larsson, and R. Vestergaard, “Analysis of Vickers indentation,” *Int. J. Solids Struct.*, vol. 31, no. 19, pp. 2679–2708, 1994.

[100] R. McDonald, “An evaluation of the mechanical properties and microstructure in

uranium dioxide doped with oxide additives," Arizona State University, 2014.

[101] A. J. Schwartz, M. Kumar, B. L. Adams, and D. P. Field, *Electron backscatter diffraction in materials science*, vol. 2. Springer, 2009.

[102] A. Brown, "Three dimensional characterization of microstructural effects on spall damage in shocked polycrystalline copper," Arizona State University, 2015.

[103] D. Stojakovic, "Electron backscatter diffraction in materials characterization," *Process. Appl. Ceram.*, vol. 6, no. 1, pp. 1–13, 2012.

[104] "Wessex Scientific and Technical Services." [Online]. Available: http://www.wxres.com.

[105] *Abaqus/CAE user's manual*. Simulia, D. S., 2007.

[106] *ABAQUS theory manual*. Simulia, D. S., 2009.

[107] "Sandia National Laboratories." [Online]. Available: http://www.sandia.gov.

[108] E. S. Hertel Jr, R. L. Bell, M. G. Elrick, A. V Farnsworth, G. I. Kerley, J. M. McGlaun, S. V Petney, S. A. Silling, P. A. Taylor, and L. Yarrington, "CTH: A software family for multi-dimensional shock physics analysis," in *Shock Waves@ Marseille I*, Springer, 1995, pp. 377–382.

[109] J. M. Walsh and R. H. Christian, "Equation of state of metals from shock wave measurements," *Phys. Rev.*, vol. 97, no. 6, p. 1544, 1955.

[110] D. E. Grady, "Strain-rate dependence of the effective viscosity under steady-wave shock compression," *Appl. Phys. Lett.*, vol. 38, no. 10, pp. 825–826, 1981.

[111] Y. Miyajima, T. Ueda, H. Adachi, T. Fujii, S. Onaka, and M. Kato, "Dislocation Density of FCC Metals Processed by ARB," *IOP Conf. Ser. Mater. Sci. Eng.*, vol. 63, no. 1, p. 12138, 2014.

[112] G. E. Totten and D. S. MacKenzie, *Handbook of aluminum: Vol. 1: physical metallurgy and processes*, vol. 1. CRC Press, 2003.

[113] "Phonon density of states of the Debye model." [Online]. Available: https://lampx.tugraz.at/~hadley/ss1/phonons/table/dosdebye.html.

[114] I. Shin and E. A. Carter, "Possible origin of the discrepancy in Peierls stresses of fcc metals: First-principles simulations of dislocation mobility in aluminum," *Phys. Rev. B - Condens. Matter Mater. Phys.*, vol. 88, no. 6, pp. 1–10, 2013.

[115] T. Vreeland, "Dislocation drag in close-packed metals," *Scr. Metall.*, vol. 18, no. 7, pp. 645–651, 1984.

[116] D. Rodney, "Activation enthalpy for kink-pair nucleation on dislocations: Comparison between static and dynamic atomic-scale simulations," *Phys. Rev. B - Condens. Matter Mater. Phys.*, vol. 76, no. 14, pp. 1–9, 2007.